Master's Thesis

Modeling of the Wheel-Soil Contact for Planetary Exploration Rovers

Alexander Männel

2nd May 2016

Supervisor: Prof. Dr.-Ing. habil. Boris Lohmann (TUM)
Prof. Dr.-Ing. Martin Otter (DLR)
Stefan Barthelmes, M.Sc. (DLR)
Maria Cruz Varona, M.Sc. (TUM)
Institutes: Institute of Automatic Control
Technische Universität München (TUM)
& Institute of System Dynamics and Control
Space Systems Dynamics
German Aerospace Center (DLR)

Erklärung

Hiermit erkläre ich, die vorliegende Arbeit selbstständig durchgeführt zu haben und keine weiteren Hilfsmittel und Quellen als die angegebenen genutzt zu haben. Mit ihrer unbefristeten Aufbewahrung in der Lehrstuhlbibliothek erkläre ich mich einverstanden.

München, den 17. Mai 2016 _____

Acknowledgment

I would first like to express my sincere gratitude to my supervisors of the German Aerospace Center (DLR) and the Technische Universität München (TUM). I want to thank Prof. Dr.-Ing. habil. Boris Lohmann of the Institute of Control (TUM) who made it possible for me to write this thesis at the DLR.

Furthermore, I want to thank my supervisors at the Institute of System Dynamics and Control - Space System Dynamics (DLR), Dr.-Ing. Johann Bals and Prof. Dr.-Ing. Martin Otter. They gave me the chance to work at the DLR and provided premises and equipment.

I would also like to express my deep gratitude to my master thesis advisor, Stefan Barthelmes. He always had a sympathetic ear for me when I had questions about my research or when I ran into trouble. I want to thank my thesis advisor Maria Cruz Varona, who was always available as reference person at the Institute of Control (TUM). Furthermore, I would like to thank all the members of the Space System Dynamics department for supporting me. Especially Fabian Buse and Roy Lichtenheldt for their input and help as well as Bernhard Rebele, Jakub Spytek and Christian Lanegger for the help with SWT experiments. In addition, I want to thank my office colleague Alexandre Dias Luciano Lima who helped me with several experiments and became a good friend during my time at the DLR.

Finally, I would like to express my gratitude to my family and my girlfriend for their encouragement and their financial support. Without their support, it would not have been possible to finish my studies at university.

Aufgabenstellung

Für die Auslegung wie auch für die Regelung von planetaren Rovern ist die Modellierung der Kontaktkräfte zwischen Rädern und weichem, verformbarem und unebenem Boden ein zentrales Element. Verschiedenste Ansätze wurden sowohl am DLR als auch außerhalb z.B. am MIT, bei der NASA oder der ESA entwickelt. Nach wie vor ist diese Modellierung jedoch Gegenstand der Forschung weltweit und alle vorhandenen Lösungen haben teils schwerwiegende Nachteile oder Probleme.

Für die Regelung und Beobachtung von Einzelrad und Gesamtfahrzeug sowie die Optimierung von Rover und Roverkomponenten wird am Institut DLR-SR ein schnelles Modell benötigt, dass dennoch viele Effekte hinreichend genau abbildet. Die Weiterentwicklung bestehender Ansätze und die Herleitung sowie Implementierung neuer Funktionen und Ansätze soll im Rahmen einer Masterarbeit verfolgt werden. Neben dem klassischen Rad-Boden-Kontakt sollen u.a. Einflüsse von Schlupf sowie dem mehrfachem Durchfahren des gleichen Bereichs abgebildet werden. Weiterhin können die genauen Bodenbeschaffenheiten, mit denen ein planetarer Rover umgehen muss weder als bekannt noch als konstant angenommen werden. Weitere mögliche Aufgabenpakete sind daher die Verwendung des entwickelten Modells für eine Sensitivitätsanalyse im Hinblick auf fehlerhafte Bodenparameter sowie für den Entwurf von Beobachteralgorithmen. In jedem Fall ist die Tauglichkeit der Ansätze und Implementierungen für Regelungs- und Beobachterentwürfe zu beachten.

Anhand bestehender Messdaten eines institutseigenen Prüfstands und/oder eigenen Messungen mit selbigem soll die Funktionsweise des entwickelten Modells abschließend bewertet und validiert werden.

Zusammenfassung

Um die kostenintensive Mission eines planetaren Explorationsrover zum Erfolg zu führen, müssen zunächst enorme Anstrengungen in Entwicklung und Design unternommen werden. Ein wichtiger Teilaspekt in der Entwicklung eines Explorationsrovers, ist die Betrachtung des Rad-Boden Kontaktes, welcher nötig ist um die Mobilität eines Rovers, besonders auf losem und weichen Boden zu gewährleisten. Dabei ermöglicht der Einsatz von Modellen und Tests in Simulation die Anzahl von teuren Prototypen zu reduzieren, was die Entwicklungskosten erheblich senkt.

In dieser Masterarbeit liegt der Fokus auf semi-empirischen Modellen der Terramechanik, deren Einsatzfähigkeit jedoch stark beschränkt ist, da diese Modelle einer starken Vereinfachung unterliegen. Deshalb werden mögliche Erweiterungen der bestehenden Modelle untersucht, um zu prüfen, ob diese Weiterentwicklungen die Einsatzfähigkeit semi-empirischer Modelle verbessern kann. Insbesondere die Eignung verschiedener Ansätze des sogenannten Borstenmodells, ein Konzept der Reibungsmodellierung, ist Gegenstand der Betrachtung und wurde in einer bestehenden Simulationsumgebung implementiert und in Simulation sowie am Prüfstand getestet.

Um diese Modellerweiterungen zu validieren und um das Rad-Boden Kontakt Verhalten zu untersuchen, wurde eine Testkampagne auf einem linear geführten Einzelradprüfstand am DLR in Oberpfaffenhofen durchgeführt.

Abstract

In order to lead the cost-intensive mission of a planetary exploration rover to a success, tremendous efforts must previously be undertaken in development and design. An important issue in the exploration rover development is the consideration of the wheel-soil contact, which is necessary to ensure the maneuverability of a rover, especially on loose and soft soil. As a consequence, the modeling of the contact reactions between wheel and soil has become a subject of research, because it can help to reduce costs in the development by using simulations instead of designing expensive prototypes.

In this master thesis the focus is on semi-empirical models of terramechanics, however the operational capability of these models is strongly limited due to their high degree of simplification. For this reason, extensions to existing models are investigated in order to verify if these extensions improve the operational capability of semi-empirical models. In particular, the suitability of different approaches of the so-called bristle model, which is a concept of friction modeling, are implemented in an existing simulation environment and then tested in simulation, as well as on a test bed.

In order to validate these model extensions, as well as to investigate the wheel-soil contact behavior in soft soil, a field campaign on the linear guided Single-Wheel Testbed at the DLR Oberpfaffenhofen are performed.

Contents

List of Figures

List of Tables

List of Abbreviations

BCM Bekker based Contact Model

BFCS BCM with bristles fixed on the contact surface

BFEW BCM with bristles fixed on the entire wheel surface

DLR German Aerospace Center (Deutsches Zentrum für Luft- und Raumfahrt e. V.)

DEM Discrete Element Method

ESA European Space Agency

FEM Finite Element Method

JPL Jet Propulsion Laboratory

MBS Multibody System

MIT Massachusetts Institute of Technology

NASA National Aeronautics and Space Administration

RMC Robotics and Mechatronics Center of the DLR

SCM Soil Contact Model

SWT Single-Wheel Testbed

TUM Technische Universität München

Nomenclature

Δt	Time increment
$\boldsymbol{f}$	Force vector
k_1, k_0	Polynomial coefficients for curve fit
$\mathbf{A}$	Matrix A
$\mathbf{b}$	Vector b
$\mathbf{e}$	Unit vector
t	Time

Wheel-soil contact modeling

α	Rotation angle of the wheel
α_{B}	Rotation angle of the wheel for bristle distribution in BFEW
β	Tilt angle of the wheel
b_{w}	Wheel width
c_{b}	Bristle damping coefficient
c	Cohesion
$c_1,\ c_2,\ c_3$	Coefficients of the normal stress distribution
$\Delta\theta$	Distance between bristles along the angle θ_i in BCM / BFCS
$\Delta\tilde{\theta}$	Distance between bristles along the angle $\tilde{\theta}_i$ in BFEW
$\Delta\xi$	Distance between bristles along the width ξ_j
$\eta,\ V_{\mathrm{CA}},\ V_{\mathrm{J}},\ D$	Independent BCM parameters
$\boldsymbol{f}_{\mathrm{D}}$	Damping force vector
$\boldsymbol{f}_{\mathrm{G}}$	Grouser force vector

N_ϕ	Flow value for computation of active and passive earth pressure.
f_n	Normal force
F_p	Force of passive earth pressure
$\boldsymbol{f}_\mathrm{total}$	Total reaction force vector
ϕ	Friction angle
$\boldsymbol{f}_\mathrm{SC}$	Surface force vector
h_G	Grouser height
h_b	Cutting depth
k_b	Bristle stiffness coefficient
$k_\mathrm{c},\ k_\phi,\ n$	BEKKER soil parameter
k_kin	Kinetic coefficient for the kinetic regime
W_Lane	Minimum SWT lane width of one test
$\mathbf{K}_\mathrm{Lim}$	BCM limitation factor
q	Load
$\boldsymbol{t}_\mathrm{D}$	Damping torque vector
$\boldsymbol{t}_\mathrm{G}$	Grouser torque vector
$\boldsymbol{t}_\mathrm{total}$	Total reaction torque vector
$\boldsymbol{t}_\mathrm{SC}$	Surface torque vector
μ_k	Friction coefficient of kinetic regime
μ_s	Friction coefficient of static regime
N_Bristles	Total number of bristles
N_SC	Total number of contact patches
ω	Angular velocity of the wheel
r_w	Wheel radius
$\boldsymbol{s}$	Bristle deflection vector
σ_p	Passive earth pressure
i	Slip
s_max	Maximum bristle deflection
$s_\mathrm{k\,max}$	Maximum bristle deflection in kinetic regime
$s_\mathrm{s\,max}$	Maximum bristle deflection in static regime

σ	Normal stress
τ	Shear stress
$\tau_{\max}$	Maximum shear stress
θ_{entry}	Entry angle of the wheel
θ_{exit}	Exit angle of the wheel
$\tilde{\theta}_{i_{\text{conv}}}$	Converted $\tilde{\theta}_i$ in order to compare it with entry and exit angle.
$\theta_i,\ \xi_j$	Bristle position in BFCS
$\tilde{\theta}_i,\ \xi_j$	Bristle position in BFEW
v_{DBP}	Drawbar pull velocity
v_{d}	Velocity deadband (threshold)
V_{J}	Reference velocity for shear stress calculation
v_{slip}	Slip velocity
$\boldsymbol{v}_{\text{t}}$	Tangential velocity vector of contact point
γ_{s}	Unit weight of soil
j	Shear displacement
m	Number of bristles (axial)
n	Number of bristles (radial)
${}^{\text{b}}\mathbf{T}_{\text{a}}$	Rotation matrix from a to b

Coordinate systems

${}^{\tilde{\text{C}}}[\cdot]$	System of bristle position in BFEW
${}^{\text{C}}[\cdot]$	System of a contact point
${}^{\text{FW}}[\cdot]$	Fixed wheel system
${}^{\text{G}}[\cdot]$	Grouser system
${}^{\text{P}}[\cdot]$	Local contact plane system
${}^{\text{W}}[\cdot]$	Wheel system

Errors computation

$\text{NRMSE} = {}^{\text{RMSE}}/_{\overline{y}}$	Normalized root-mean-square error
$\overline{y}$	Mean of observed results
$\text{RMSE} = \sqrt{\frac{\sum_{k=1}^{n}(y_k - \tilde{y}_k)^2}{n}}$	Root-mean-square error
$\tilde{y}$	Predicted results
n	Number of results
y	Observed results

1. Introduction

1.1. Motivation

For investigation of the solar system planetary exploration rovers have become a significant element. The increasing number and requirements of planetary exploration missions resulted in an intensified research of rovers. In order to ensure the success of an exploration, a reliable locomotion of these vehicles must be guaranteed. Previous exploration missions showed that difficult soil conditions could endanger the entire mission. A prime example is NASA's Mars rover Spirit which got stuck in loose sand in 2009 because of slip sinkage, as illustrated in Figure 1.1. Despite enormous efforts over several months, the engineers of NASA failed to free the sand-trapped rover. Through this incident, Spirit was no longer able to align its solar cells to the sun to collect enough energy for primary functions. Therefore, the engineers lost contact to Spirit one year later [5].
A further example is NASA's Mission MSL - Curiosity. In July 2014, the rover drove across an area called "Zabriskie Plateau" which is interspersed with hazardously sharp

Figure 1.1.: The Mars rover Spirit stuck in soft sand [33].

rocks. Damage to the aluminum wheels could not be prevented despite a detour of about 200 meters [34].

These examples show that the locomotion of the rover is a bottleneck problem. In order to avoid such occurrences in future rover missions it is necessary to have comprehensive understanding about the mechanical wheel-soil reactions, the so-called terramechanics. A substantial knowledge in this field enables a development of suitable rover design and capable controller strategies in a shorter time. Moreover, costs can be saved by depicting the terramechanics in simulations in order to decrease the number of prototypes which must be developed. For this reason, the modeling of contact forces between the rover's wheel and the soil, based on knowledge of the terramechanics has become a subject of ongoing efforts in research [3], [5].

1.2. Exploration Rovers on Planetary Missions

There are many reasons for using a rover for planetary exploration, as those vehicles are able to drive directly to a place of interest and can perform scientific observations, which are considerable advantages compared to other space probes as stationary landers or orbiters [6].

Figure 1.2 shows some examples of planetary exploration rovers. On the right, Mars rover Spirit (MER-A) is illustrated which was launched from earth in June 2003. The rover was developed by the Jet Propulsion Laboratory (JPL), a research and development center of the California Institute of Technology. As already mentioned, the Spirit mission ended in 2010, after the rover got stuck in soft sand. In the center, the ExoMars rover can be seen

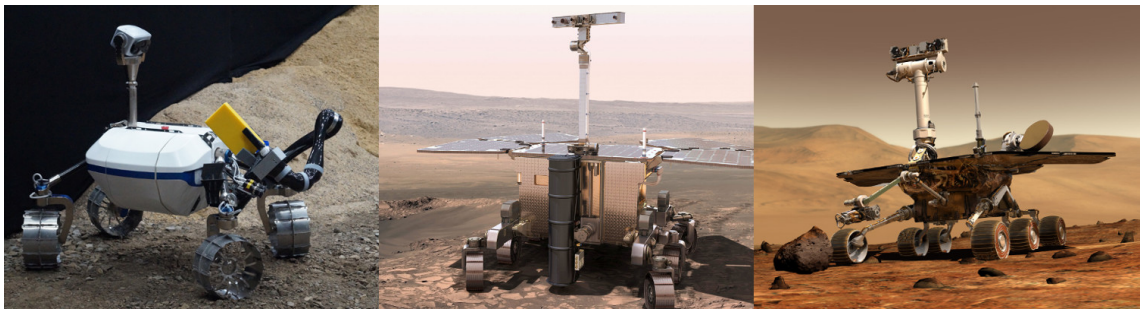

Figure 1.2.: Examples of different planetary exploration rovers. Left: LRU (DLR) [7], center: EXOMARS (ESA) [10], right: MER-A Spirit (JPL) [32].

which belongs to the mars mission of the European Space Agency (ESA). The start date for the rover mission is scheduled to be in 2018. As an example for a current research project the Lightweight Rover Unit (LRU) is shown on the left of Figure 1.2. The rover was developed by the Robotics and Mechatronics Center (RMC) of the German Aerospace Center (DLR) and is used for further research and the development of rover components for future rover missions [3], [9].

The wheel design is significant for the locomotion of an exploration rover. Current rovers have a wheel radius which ranges from 100 mm to 250 mm and the wheel width ranges from 100 mm to 400 mm. The wheel size usually depends on the size and weight of the rover [31], [36]. Moreover, they are designed as hollow cylinders to reduce the rover's total weight. Because of the extreme operating conditions of planetary rovers, the wheels are usually made of a metal strip which encircles the spokes. Moreover, the metal strip and the spokes can be flexible or rigid [37]. On the other hand, wheels with tires made of a rubber compound are unsuitable because of the extreme temperatures and the radiation in space [38].

Another important element of the rover's wheel design are the so-called grousers which are structures attached to the wheel surface transversally to the roll direction. The purpose of grousers is to improve the tractive performance of the rover, especially in loose soil [26].

1.3. Wheel-Soil Modeling

Wheel-soil contact models allow the development of model-based controller strategies for the rover's locomotion, respectively the coordination of the wheel and steering drives. Due to the large spatial distance between ground control and the exploration vehicle, there is a tremendous signal latency but because of increasing requirements, the rover also has to overcome larger distances, as well as drive on difficult terrain. This results in a need of path-finding and partially autonomous driving algorithms for the rover, where wheel-soil contact models can be helpful [21].

The wheel-soil contact modeling leads to the research field of the so-called terramechanics which deals specifically with the mechanical properties of soils and the behavior of the soil during application of force and its retroactive effect on penetrating objects. The

term terramechanics was first used by Prof. BEKKER in his book "Off-road locomotion: research and development in terramechanics" in 1960 [2]. This research field first arose with the entry of farm machinery in agriculture and the need of increasing the yield. As a consequence, the agricultural engines have become bigger and heavier in order to work on more soil in the same amount of time. Simultaneously, the soil pressure caused by heavy machinery was to be kept as low as possible to avoid any damage to the yield, which was the motivation to create mathematical descriptions to predict the wheel sinkage and the soil pressure of farm machinery. Later, this knowledge was also used for further development of military vehicles [23]. With the use of planetary rovers to explore other planets in the solar system, terramechanics also became a research field in the aerospace.

As Figure 1.3 illustrates, terramechanics plays an important role in several design and development steps of a planetary exploration rover, as the soil properties on planetary exploration missions can never be accurately determined prior to the start of the mission and can quickly change during exploration [5]. Through the theoretical knowledge of terramechanics the design of the wheel, as well as the wheel-load distribution and the locomotion kinematics of an off-road vehicle can be improved in order to increase their locomotion performance, even under changing soil conditions. In the age of increasingly powerful computers, Multibody System (MBS) simulations including the wheel-soil contact behavior can be performed, as well as development and the use of intelligent locomotion controls becoming possible [5].

There are different factors that have an influence on the wheel-soil reactions, such as soil properties and shear behavior on the one hand and constructive aspects like the wheel design and the load distribution on the other [5], [21]. For this reason, the wheel-soil contact modeling is a strongly non-linear problem, which makes the system more difficult to handle.

In order to properly describe wheel-soil reactions it is necessary to consider the friction between wheel and soil, which can depend on many different properties, among others, the tangential velocity, the kind of material, the topology and geometry of the surface, as well as the lubrication. For this reason, the modeling of friction is not trivial as it is hard to describe friction mathematically [35]. Especially the calculation of the friction force at zero velocity and the transition to low velocity are hard to describe and thus, friction

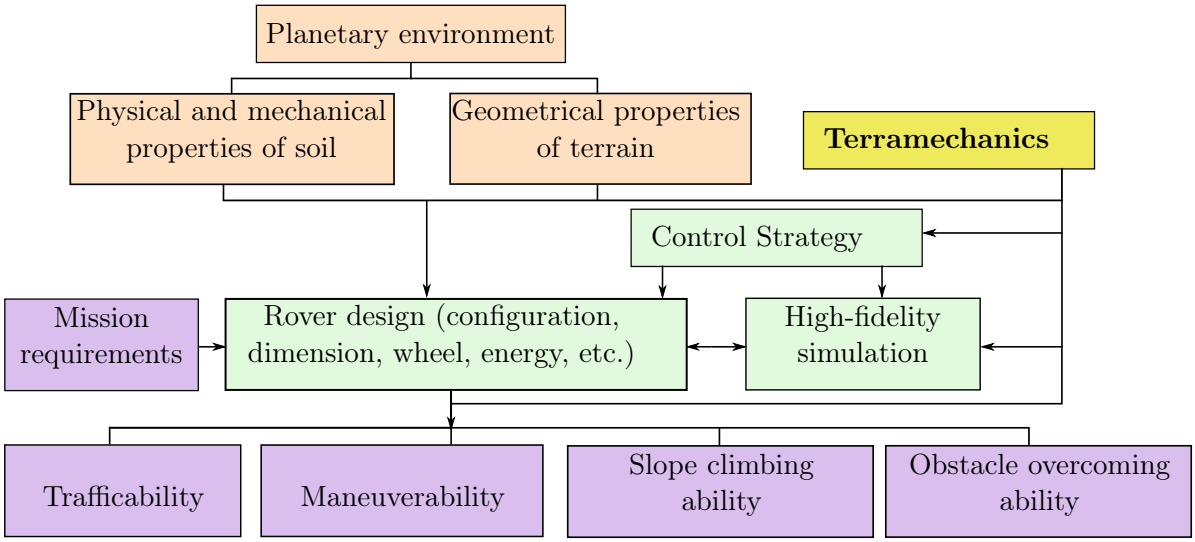

Figure 1.3.: Fields in which terramechanics is an important field, cf. [5].

models may be highly error-prone [40]. As a consequence, many different approaches have been developed in the last decades in order to predict friction accurately, as explicitly described in 2.2.

All these considerations are important in order to develop suitable wheel-soil contact models which help to observe and predict the locomotion of rovers on difficult terrain.

1.4. Objectives

This Master's Thesis investigates the modeling of wheel-soil contact and especially the shear stress modeling of wheel and soil. One requirement is the real-time capability of these models, because they should be usable for a rover's locomotion control. For this reason, only semi-empirical models will be part of this work as they combine experimental results on the one hand with physical relations on the other and thus lead to a reasonable compromise between accuracy and computational effort [5].

One of these models is the Bekker based Contact Model (BCM), which is based on the semi-empirical equations of Bekker [2], Wong [45], Janosi, as well as Hamamoto [45] and is supposed to be extended in this thesis by two approaches. Following this, these BCM extensions are investigated in a simulation tool.

Finally, in order to validate the theoretical model, experiments on a special test rig for

investigations on wheel-soil contact, the so-called Single-Wheel Testbed (SWT) have to be performed subsequently. The SWT is used at the Robotics and Mechatronics Center (RMC) of the DLR.

1.5. Structure of Thesis

Chapter 2 gives an overview on the state of the art concerning the topics which are important for the remainder of this thesis. This includes among others, the introduction to different current approaches that describe the wheel-soil interactions and the modeling of friction and subsequently the BCM model equations are introduced in Chapter 3. After this, the implementation of further developments of BCM, with an alternative description of the shear behavior between wheel and soil, are considered in Chapter 4 . In Chapter 5, the model extensions are analyzed in simulation and suitable values for the model parameters are discussed. Finally, the models are validated with experiments performed with the SWT at the DLR. An introduction of the SWT and different test scenarios is given in Chapter 6 and in Chapter 7 the results are presented and discussed. In Chapter 8, further developments are discussed as an outlook for future works.

2. State of the Art

Different approaches of wheel-soil contact modeling are currently considered in research. On the one hand, these are element or particle methods like the Finite Element Method (FEM) and the Discrete Element Method (DEM) which also have significance in other research fields [5]. In Discrete Element Method (DEM) simulation, the medium, respectively the soil, is depicted as a large number of discrete particles, which can move each in 6 degrees of freedom. Furthermore, there is no fixed geometric relation between the particles but the motion of each particle is only computed regarding the forces which arise from particle contacts and external forces [25]. An illustration of the DEM can be seen in Figure 2.1. The FEM approach considers the soil as a continuum, where the mesh has fixed neighbored nodes [25], [36]. In case of a wheel-soil contact, the mesh will be distorted by the contact reaction forces and torques.

These methods enable to compute an accurate prediction of the wheel-soil contact but on the other hand the computational effort to simulate these models is extensive and for real-time capable applications, as model-based controller, FEM and DEM are unsuitable. For this reason, semi-empirical methods of the wheel-soil contact are on the focus of this

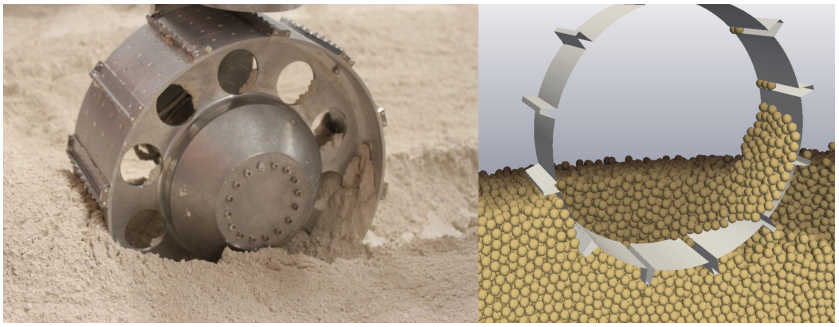

Figure 2.1.: Wheel-soil contact modeling of a single wheel in experiment(left) and with the discrete element method (right), [25].

work. These approaches are based on theoretical knowledge combined with experimental results and mostly based on the findings of BEKKER, which introduced firstly. After this, an overview of friction modeling is given and finally different wheel-soil contact models are introduced.

2.1. Modeling of Wheel Sinkage and Earth Pressure

BEKKER's analysis and investigations regarding the pressure-sinkage relationship of soil are still basis for many semi-empirical approaches. Due to the vehicle's weight, the wheel induces a load to the surface of the terrain which leads to a soil deformation. This increasing deformation causes a rising sinkage of the wheel. BEKKER considered the relationship between pressure and sinkage by performing penetration tests. The test arrangement consists of plates of different shapes and areas which are pressed vertically into a homogeneous soil surface and is called Bevameter (short for BEKKER Value Meter). The measurement values of the Bevameter experiment are the sinkage and the normal force. BEKKER developed a mathematical relationship from the measured data, the nonlinear pressure-sinkage equation [2], as

$$\sigma = \left(\frac{k_\mathrm{c}}{b} + k_\phi \right) z^n. \tag{2.1}$$

where σ is the normal stress at a given plate sinkage z, and k_c, k_ϕ, n are the so-called BEKKER soil parameters for an individual homogeneous soil and b is the diameter of the test plate. In order to predict the wheel sinkage, the wheel width is used for b instead of the diameter of a plate. However, it should be mentioned that BEKKER's theory was originally developed for plates. The BEKKER soil parameters k_c, k_ϕ and n are listed in Table 2.1 with the corresponding units. Note that a detailed description of the identification of the parameters can be found in [45]. Another derivative of the Bevameter test can be found in the work of Apfelbeck [1].

The grousers have an important influence on the locomotion of the wheel, as its motion performance depends on the number of grousers on the wheel surface, the grouser shape, as well as the thickness [26]. The calculation of the grouser effects are based on the

Table 2.1.: BEKKER soil parameter and units.

Parameter	Description	Unit
k_c	Cohesive modulus	$\mathrm{kN/m^{n+1}}$
k_ϕ	Friction modulus	$\mathrm{kN/m^{n+2}}$
n	Exponent of deformation	-

equations of the passive earth pressure theory which are briefly discussed in the following. Details can be found in [41] and [45]. In Figure 2.2, a wheel with grousers is illustrated, where the lowest grouser is fully embedded in the soil. In order to calculate the driving force of a grouser, the passive earth pressure σ_p is calculated as

$$\sigma_\mathrm{p} = \gamma_\mathrm{s} z N_\phi + q N_\phi + 2c\sqrt{N_\phi}, \quad \text{with} \quad N_\phi = \tan^2\left(\frac{\pi}{4} + \frac{\phi}{2}\right), \tag{2.2}$$

with the unit weight $\gamma_\mathrm{s} = \rho g$, the load q, cohesion c, the flow value N_ϕ and the depth z. In the next step, the passive earth pressure must be integrated over the cutting depth of the grouser h_b, which yields

$$F_\mathrm{p} = \int_0^{h_\mathrm{b}} \sigma_\mathrm{p}\, dz = \frac{1}{2}\gamma_\mathrm{s} h_\mathrm{b}^2 N_\phi + q h_\mathrm{b} N_\phi + 2c h_\mathrm{b}\sqrt{N_\phi}, \tag{2.3}$$

to calculate the driving force of one grouser.

Further effects are the lateral force, caused by the pressure of the soil to the wheel flanks,

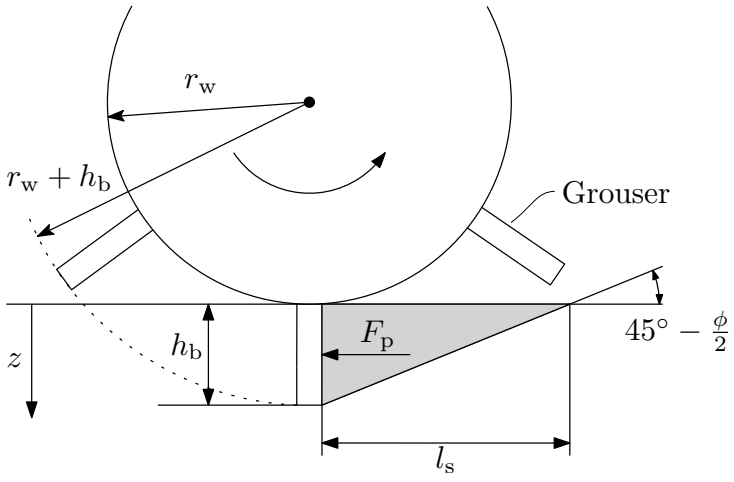

Figure 2.2.: Grouser-soil interaction of a wheel with soil, cf. [45].

and the bulldozing phenomena. Bulldozing means that the displaced soil gathers in front of the wheel and thus the wheel shoves that loosened soil in the direction of motion, which results in a further resistance to the wheel locomotion [17].
The so-called multi-pass effect describes the difference in soil condition and resulting contact forces between a front wheel, driving on untouched ground, and a rear wheel, following in the first wheel's track. Depending on the amount of slip of the front wheel, the soil is either compressed or loosened. This leads to higher or respectively lower sinkage and ultimately to said differences in contact forces and torques. Especially for soft, granular soil this effect should be taken into account [5], [13].

2.2. Modeling of Friction

In addition to the aforementioned normal stress on the soil caused by the wheel, there are also forces and torques which are tangential to the soil surface. For the prediction of tangential reactions, the modeling of friction is necessary.
The motivation of researchers to model the behavior of friction has been high for over 300 years, as friction occurs practically in any mechanical system. One of the first attempts to describe friction is the COULOMB friction model which describes the proportional relationship between the normal force and the friction force. Moreover, COULOMB worked out that friction is independent from the contact area. However, this approach only considers the behavior of friction when the involved bodies are in relative motion, the so-called sliding regime. Thus, the model is not able to depict the friction behavior in the sticking regime, respectively at zero velocity [19]. Though it is necessary to consider both the sticking and the sliding regime in order to predict the dynamic behavior of a MBS that includes contact between bodies. As a consequence, several approaches have been developed in order to obtain models with an improved validity.
STRIBECK proposed a more comprehensive model which combines static, kinetic and viscose friction and from this he developed the *Stribeck curve* [39]. The transition from static to kinetic friction is assumed in this model as a continuous process. In 1985, KARNOPP introduced a model which changes its state when the relative velocity of the contact bodies ranges around zero velocity [18]. In this case, the model treats the friction

as if the contact bodies already were at zero velocity and thus it assumes static friction. A further method is the DAHL model which was especially developed for the description of friction in ball bearings. DAHL showed that friction depends on the relative velocity between the respective contact bodies and the displacement of their material. In addition he found that the friction behavior strongly depends on whether the material is brittle or ductile [4]. Moreover, the DAHL model can be seen as the predecessor of the models which are introduced in detail in Section 2.2.2 and Section 2.2.3 [24], [29], [40].

2.2.1. Mohr-Coulomb Criterion and Extensions

The tangential forces and torques originated from wheel-soil contact results in a shear stress of the soil. At a certain point, when shear stress exceeds the maximum shear strength of the soil $\tau_{\max}$, a plastic flow of the soil sets in, the so-called shear-failure. This maximum shear strength of a soil is defined by the MOHR-COULOMB failure criterion as

$$\tau_{\max} = c + \sigma \tan \phi, \tag{2.4}$$

with the individual soil parameters cohesion c and the friction angle ϕ and σ as the normal stress.

However, for loose soils the shear strength also depends on the soil compaction, because a soil with higher compaction can absorb more tangential forces before it fails. For this reason, JANOSI and HANAMOTO proposed the following extension to the MOHR-COULOMB failure criterion [45], which is the shear stress-displacement relationship, as

$$\tau = \underbrace{c + \sigma \tan \phi}_{\tau_{\max}} \left(1 - e^{\frac{j}{K}}\right), \tag{2.5}$$

where j is the shear displacement, which is caused by the deformation of soil and K is the horizontal shear deformation modulus which depends on the soil compressibility. The shear stress-displacement relationship for loose soils can seen in Figure 2.3 which shows the relation between the shear displacement j and the shear stress τ. Furthermore, it can be seen that the shear stress converges to $\tau_{\max}$ and that K describes the initial gradient of the function [45].

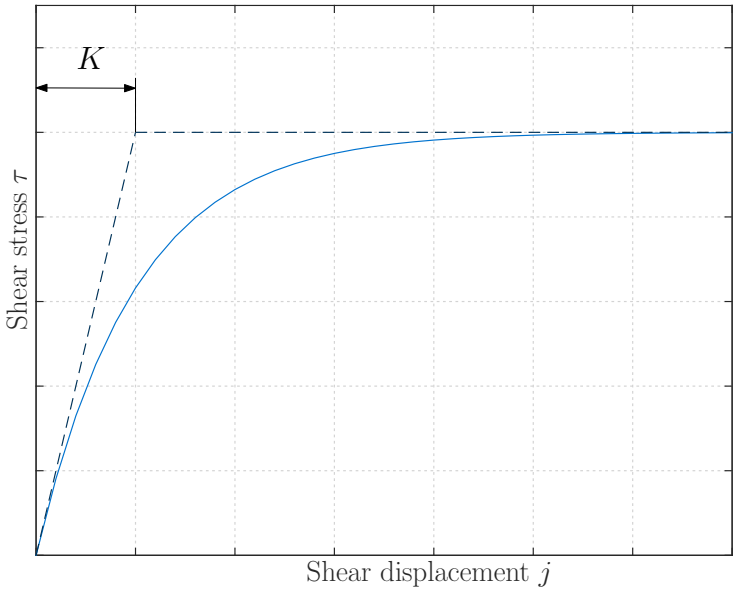

Figure 2.3.: Shear stress - Shear displacement curve, cf. [45].

2.2.2. Bristle Friction Model

The bristle friction model was proposed by Haessig and Friedland in [14] with the motivation to describe the friction between two surfaces as a large number of microscopical contact points [35]. This was derived from the idea that friction force is a result of elastic and plastic deformations of the surface [29]. The method is intended to represent the microscopical physical bonds of a contact surface as bristle bonds. However, it is not recommended to represent each microscopical physical bond of a real contact surface as one bristle bond because the number is most probably very high and it would lead to a high computational effort. Instead, a relatively small number of bristles n should be chosen for the entire contact surface. Haessig and Friedland found that a relatively small number (i.e., $n \leq 50$) is sufficient for an adequate depiction of the friction phenomena [14]. As a result a $1/n$-th part of all physical bonds of the contact surface is condensed in one bristle bond. Simply put, the behavior of friction can be imagined as a brush which slides over the surface as shown in Figure 2.4.

In this case, the upper surface slides over the stationary lower surface and the bristle of the stationary surface are pliable and the bristle of the sliding body are rigid. When a pliable and a rigid bristle are at the same position, both are bonded. The relative motion

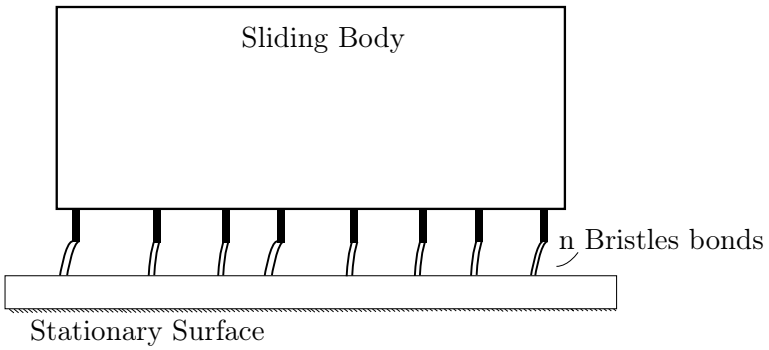

Figure 2.4.: Illustration of the bristle friction, with n bristles, cf. [14].

between the upper and lower surface leads to a strain of the pliable bristle of each bristle bond. The deflection is now $x_i - b_i$, where x_i is the position of the deflected bristle bond and b_i the original location of the unloaded bristle bond. For a better understanding, Figure 2.5 shows the relations within one bristle bond. Furthermore, it is assumed that each pliable bristle has a stiffness k_b. Hence, the pliable bristle acts like a spring, where one has to apply a force to deflect the spring. The sum of n bristle loads and thus the sum of all bristle forces represents the resulting friction force between the two surfaces which yields

$$f_\mathrm{friction}\left(t\right) = \sum_{i=1}^{n} k_\mathrm{b}\left(x_i\left(t\right) - b_i\right). \tag{2.6}$$

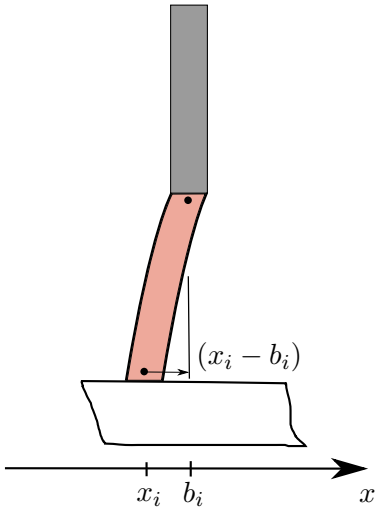

Figure 2.5.: Deflection of a single bristle bond, cf. [14].

If the bristle deflection $x_i - b_i$ exceeds a defined level $s_{\max}$, it is assumed that the bristle bond snaps and contributes no longer an amount to the friction force. At the same time a new unloaded pliable bristle rises at other random location compared to the previous one. Through this stochastic feature the transition point between static and kinetic friction can slightly change and this captures the random nature of friction [16]. For more details about the random behavior of friction, please refer to [16]. Since there is no damping the model will be oscillatory in motion and a damping term should be integrated as shown in 2.2.3. Another disadvantage is that the computation of the bristle friction model can be inefficient because the snapping of the bristle bonds can lead to discontinuities which are hard to handle for the integration algorithm of a simulation because the time step must be set very short. Furthermore, the model is only defined in a single dimensional space, and thus it is only usable for 1D application and it cannot be used for a 3D simulation, with the friction force being time-varying and a vector in 3D space [28], [35].

2.2.3. Extended Bristle Friction Model

From the motivation to use the bristle friction model for MBS simulations Ma [28], Liang [24] and Fillmore [12] proposed an extended bristle friction model for 3D space. They introduce a standalone model which can be integrated in a 3D multibody dynamics simulation. The following considerations are completely based on Liang's work [24]. In this approach, the bristles are assumed as springs with effective average deflections, which are in the tangential plane of their corresponding contact points, because friction force always occurs in common tangential planes of two contact points. Furthermore, a bristle does not break when the bristle deflection reaches the maximum level $s_{\max}$. Instead of breaking, the bristle remains at this maximum level which makes the model significantly faster to compute. As a result of the unbreakable bristle spring, the randomness of the friction is lost. For this reason, the transition from the static and the dynamic regime is always at the same point. The loss of this stochastic feature leads to less accuracy on the one hand, but a faster computation of the model on the other.

Figure 2.6 illustrates the relative motion between body 1 and body 2 at the time t and $t + \Delta t$. Note that for a better understanding only one contact point is assumed. The contact point with the assumed bristle is represented by P which is time-varying, as well

as the corresponding tangential plane. The time-varying 3D friction force vector in the contact point is now defined as

$$\boldsymbol{f}\,(t) = -k_{\mathrm{b}}\ \boldsymbol{s}\,(t)\,, \tag{2.7}$$

where k_{b} is the scalar bristle stiffness and $\boldsymbol{s}$ the 3-dimensional bristle deflection vector, respectively the displacement vector. The bristle deflection vector $\boldsymbol{s}$ is defined, as follows

$$\boldsymbol{s}(t) = \begin{cases} \boldsymbol{s}\,(t_0) + \int\limits_{t_0}^{t} \boldsymbol{v}_{\mathrm{t}}\,(t)\,\mathrm{d}t, & \text{if } ||\boldsymbol{s}|| < s_{\max}\,(t) \\ s_{\max}\,(t)\,\frac{\boldsymbol{v}_{\mathrm{t}}(t)}{||\boldsymbol{v}_{\mathrm{t}}(t)||}, & \text{if } ||\boldsymbol{s}|| \geq s_{\max}\,(t)\,, \end{cases} \tag{2.8}$$

where $\boldsymbol{v}_{\mathrm{t}}$ is the tangential velocity vector of the contact point P, t is the current time, t_0 the start time of the contact and thus, $\boldsymbol{s}(t_0)$ the initial bristle deflection vector. Equation (2.8) shows that the bristle deflection is the time integration of the tangential velocity $\boldsymbol{v}_{\mathrm{t}}$. As already mentioned, the bristle bond is unable to snap in this model approach. For this reason, when the bristle deflection reaches the scalar maximum level of deflection $s_{\max}$, the bristle remains at the time-varying maximum deflection.

In order to take static and kinetic friction into account, the computation of $s_{\max}$ depends

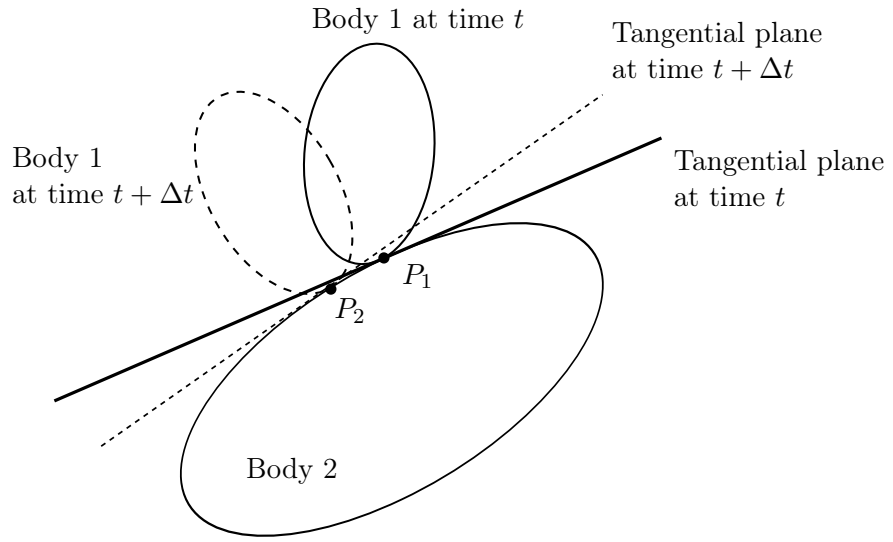

Figure 2.6.: The extended bristle model, cf. [24].

on whether the contact point P is in sliding or in sticking mode and yields

$$s_{\max}(t) = \begin{cases} s_{\mathrm{k\,max}}(t) = \frac{\mu_{\mathrm{k}} f_{\mathrm{n}}(t)}{k_{\mathrm{b}}}, & \text{if } ||\boldsymbol{v}_{\mathrm{t}}(t)|| > v_{\mathrm{d}} \\ s_{\mathrm{s\,max}}(t) = \frac{\mu_{\mathrm{s}} f_{\mathrm{n}}(t)}{k_{\mathrm{b}}}, & \text{if } ||\boldsymbol{v}_{\mathrm{t}}(t)|| \leq v_{\mathrm{d}}. \end{cases} \tag{2.9}$$

f_{n} is the normal force which is acting at the contact point P, μ_{s} is the scalar static friction coefficient in sticking mode and μ_{k} is the scalar kinetic friction coefficient when the system is in sliding mode. The scalar velocity deadband v_{d}, also called threshold, is the boundary between the two friction types. This threshold is necessary to capture the sticking mode, which is around zero velocity, because exact zero velocity would be barley reached in numerical simulations. If $||\boldsymbol{v}_{\mathrm{t}}||$ is less than v_{d} the contact point is within the sticking mode and $s_{\max} = s_{\mathrm{s\,max}}$. However, if $||\boldsymbol{v}_{\mathrm{t}}||$ is greater than v_{d} the contact point is within sliding mode and $s_{\max} = s_{\mathrm{k\,max}}$.

The definitions of the bristle deflection $\boldsymbol{s}$ and the maximum bristle deflection $s_{\max}$ become clearer in Figure 2.7. In this figure, the tangential planes of time t and $t+\Delta t$ of Figure 2.6 are illustrated in top view. The point in the middle represents the contact point P of two surfaces, where the normal and friction force are applied. The outer circles illustrate the maximum bristle deflection $s_{\mathrm{s\,max}}$ in case of static regime, whereas the inner circle shows

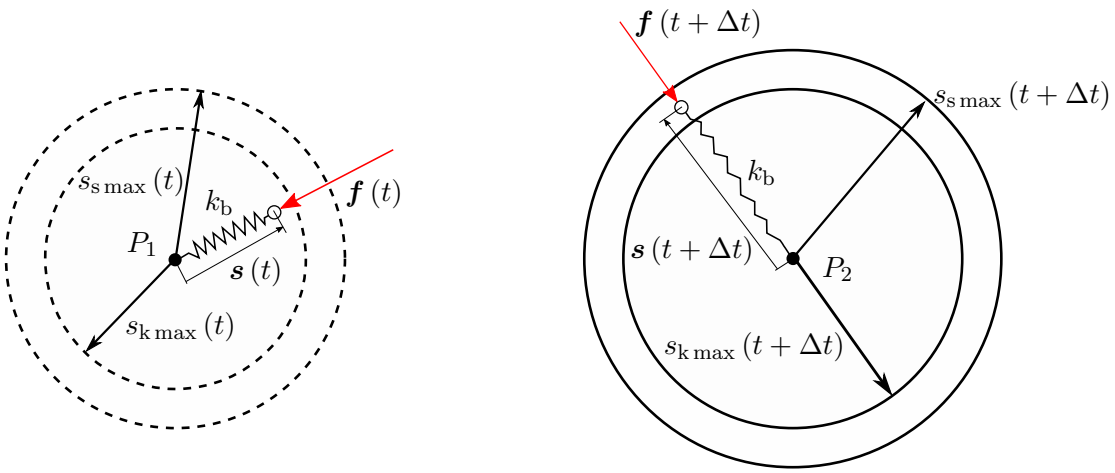

Tangential plane at time t Tangential plane at time $(t+\Delta t)$

Figure 2.7.: Tangential planes of the extended bristle model at time t (left) and $t+\Delta t$ (right), cf. [24].

the maximum bristle deflection $s_{\mathrm{k\,max}}$ when the system is in the kinetic regime. Moreover, μ_{s} is always greater than μ_{k}, because the friction force is greater in sticking mode than in sliding mode. For this reason, $s_{\mathrm{s\,max}}$ is always the outer circle and the bristle deflection can be higher in sticking mode. As the bristle acts like a linear spring, a higher maximum deflection s_{max} leads to a higher spring force and thus, the friction force is higher in the sticking regime. In Figure 2.7, it can be seen that the bristle deflection is completely within the inner circle at time point t (left figure) and thus, the system is the sliding mode. On the contrary, the system is in sticking mode at time point $t + \Delta t$ (right figure), because the tangential velocity $||\boldsymbol{v}_{\mathrm{t}}||$ fell below the velocity deadband v_{d} within the time step Δt.

As already mentioned, a disadvantage of the bristle model is the oscillatory behavior. In order to prevent an oscillation, a damping term can be added to Equation (2.7), as

$$\boldsymbol{f}\,(t) = -k_{\mathrm{b}}\boldsymbol{s}\,(t) - c_{\mathrm{b}}\dot{\boldsymbol{s}}\,(t)\,, \tag{2.10}$$

where the parameter c_{b} is the damping coefficient of the bristle.

The five introduced bristle parameters are listed in Table 2.2 for a better overview. For

Table 2.2.: The five bristle parameters.

Parameter	Symbol	Unit
Bristle stiffness	k_{b}	$^{\mathrm{N}}/_{\mathrm{m}}$
Bristle damping	c_{b}	$^{\mathrm{Ns}}/_{\mathrm{m}}$
Static coefficient of friction	μ_{s}	$-$
Kinetic coefficient of friction	μ_{k}	$-$
Velocity deadband (Threshold)	v_{d}	$^{\mathrm{m}}/_{\mathrm{s}}$

adequate friction force results the parameters must be identified precisely. Moreover, the bristle friction model needs two dynamic input values for each contact point to calculate the total friction force which are shown in Table 2.3.

Table 2.3.: Inputs of the bristle friction model.

Inputs	Symbol	Unit
Normal force of the contact point	f_n	N
Tangential velocity of the contact point	$\boldsymbol{v}_\mathrm{t}$	$^\mathrm{m}/_\mathrm{s}$

2.3. Modeling of Wheel-Soil Contact

The dynamic modeling and simulation of wheel-soil contact based on the relationships, which are mentioned in the previous sections, is the motivation of many researchers and several developments of different research institutions are state of the art.

Trease et al. [43] from JPL introduces a dynamic wheel-soil contact model and a simulation tool called *ARTEMIS* (Adams-based Rover Terramechanics and Mobility Interaction Simulator) which is based on the MBS simulation tool MSC Adams. This model uses the relationships of Bekker, Wong and Janosi. For the contact force computation between wheel and soil only a single contact point is assumed and the a rolling resistance caused by the wheel penetration is not considered.

Yoshida et al. [46] proposed a model which tangential forces are calculated by multiplying the normal force by a load-traction factor. This factor depends on the slip ratio of the wheel. However, in this work the load-traction factor was not analytical derived, but identified by velocity measurements. Based on the velocity data, the slip was obtained and the traction force was calculated by the motor characteristics between the driving torque and the angular velocity [46]. From this data the load-traction factor can be obtained.

Another semi-empirical wheel-soil contact model, with flexible wheels is proposed by Scharringhausen et al. (DLR) in [11] and in [37]. In order to calculate the sinkage of the flexible wheel, the wheel is assumed to be rigid, firstly. In a second step, the ground pressure is calculated to achieve the deflection of the flexible wheel. This deflected wheel has a new shape, which is assumed as an ellipse in the section where the wheel is penetrated in soil [37]. In this approach, the wheel-soil contact surface is divided into three parts. The equations for normal pressure, wheel sinkage as well as the soil shear displacement have been modified for this three sections to take the elliptic shape of the flexible

wheel into account.

2.3.1. Bekker Based Contact Model (BCM)

The Bekker based Contact Model (BCM) is a semi-empirical model developed by the DLR. BCM calculates the reaction forces and torques between soil and wheel from the current position and the velocity of the wheel. The velocity and position is given by a MBS, which is connected to the wheel [3]. From this data the contact reactions are computed based on the semi-empirical equations of Bekker, Wong and Janosi [45]. Furthermore, BCM is a one-step procedure, which means that the algorithm only uses the information of the current time step [3]. The advantage of a one-step procedure is the low computational effort, which is important for real time applications. For simulation of BCM the Multi-Physics Modeling and Simulation Tool *Dymola* is used. The existing BCM is the starting point which will be further developed within this Master Thesis. For this reason, the functional principle and the equations of BCM are introduced in Chapter 3.

2.3.2. Soil Contact Model (SCM)

Another semi-empirical model for wheel-soil contact simulation is the so-called Soil Contact Model (SCM). The SCM was developed by the DLR and a detailed description can be found in [20] and [22].
SCM is connected to a MBS which sets velocity and position of the wheel and it is also based on the equations of Bekker, Wong and Janosi [45], with the corresponding wheel, soil and Bekker parameters.
In addition to the soil parameters, SCM contains a description of the soil surface as a Digital Elevation Model. This means that the soil surface is represented by a mesh, where each grid node contains information about the height of the surface. As a result, it is possible to model soil deformations and surface topology. Furthermore, the wheel's surface is represented as a point cloud. The Digital Elevation Model of the soil and the point cloud of the wheel is also used for contact detection between wheel and soil. From this contact detection, a discretized footprint of the wheel in the soil is computed.

Based on this footprint the BEKKER equations are used to calculate the contact forces and torques, which are given back to the MBS. The advantage of SCM is, that it considers plastic deformations of soil and thus, bulldozing, multi-pass, as well as lateral guidance can be modeled. However, this also means a higher computational effort compared to the BCM algorithm.

3. Bekker Based Contact Model

In this chapter the equations and functional principle of the BEKKER based Contact Model (BCM) are briefly introduced. Note, that this introduction is based on the work of Fabian Buse [3].

BCM needs as input values position and velocity of the wheel, provided by the MBS which is connected to the wheel. From this input the algorithm computes the resulting 3D contact reaction force vector $\boldsymbol{f}_{\text{total}}$ and torque vector $\boldsymbol{t}_{\text{total}}$. These forces and torques are the output of the BCM, which are given back to the connected MBS.

In addition to the input values, the BCM needs a set of parameters. As wheel parameters, the BCM algorithm requires the wheel width b_{w} and the wheel radius r_{w}. In order to calculate the grouser reactions, the height and width and the number of grousers are needed as well. The soil is described by the density ρ, the friction angle ϕ, the cohesion c and the BEKKER soil parameters k_{c}, k_{ϕ} and n. Moreover the BCM algorithm requires a set of independent parameters, which are briefly described in Table 3.1.

For simulation of BCM the Multi-Physics Modeling and Simulation Tool *Dymola* which is based on the programming language *Modelica* is used [8]. *Modelica* is an object-orientated,

Table 3.1.: Independent BCM parameters.

Parameter	Description
η	The relation of the wheel-soil entry angle and the minimal exit angle, as $\theta_{\text{exit}} = -\eta\ \theta_{\text{entry}}$
V_{CA}	Reference velocity for the adjustment of the velocity dependent exit angle θ_{exit}
V_{J}	Reference velocity for the determination of shear stress from the slip velocity
D	Damping coefficient for $\boldsymbol{f}_{\text{D}}$ and $\boldsymbol{t}_{\text{D}}$ computation

equation based language and was developed especially for modeling of complex physical systems [42].

For the contact detection between wheel and soil, the *DLR Visualization Library* is used, as it provides a contact detection tool. *DLR Visualization Library* utilizes the *Modelica* interface to the programming language C and it can be used with *Dymola* [15].

3.1. Coordinate Systems

As shown in Figure 3.1, the BCM algorithm uses five coordinate systems for computing the wheel-soil behavior. The $^{\mathrm{W}}[\cdot]$ system is used to describe position and orientation of the wheel in the world system. Moreover, $^{\mathrm{FW}}[\cdot]$ is the fixed wheel system which is used as an auxiliary system parallel to the soil. The origins of the $^{\mathrm{W}}[\cdot]$ and the $^{\mathrm{FW}}[\cdot]$ system are in the wheel center and the $^{\mathrm{W}}[\cdot]$ turns about the y_{f} axis. The current rotation is described by angle α, which is the angle between the x_{f} and x_{w} axis. For calculations at a contact point, the $^{\mathrm{C}}[\cdot]$ system is used. In order to calculate the reaction forces and torques of one grouser the $^{\mathrm{G}}[\cdot]$ system is used. Finally, there is the local contact plane $^{\mathrm{P}}[\cdot]$ system which is given by the contact detection. The wheel tilt angle is β, as the angle between z_{f} and z_{p} axis.

The $^{\mathrm{W}}[\cdot]$ system is given by the MBS, whereas the contact detection provides the local contact plane $^{\mathrm{P}}[\cdot]$. From these coordinate systems the position and velocity of the wheel can be directly obtained. Based on these inputs, further angles can be calculated as the

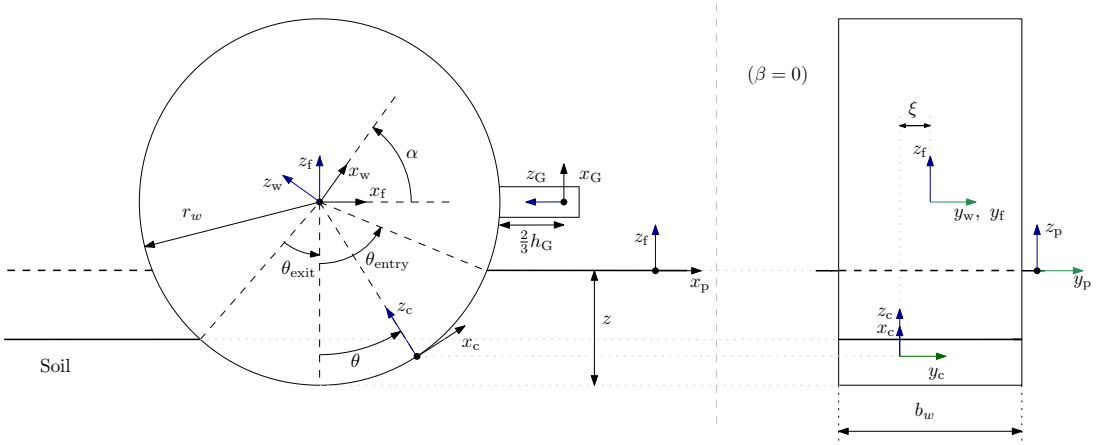

Figure 3.1.: The coordinate systems of the BCM algorithm for $\beta = 0$ and without grousers cf. [3].

exit angle θ_{exit} and the entry angle θ_{entry} of the wheel-soil contact, which can be seen in Figure 3.1.

For the description of the current local contact point ${}^{\text{C}}[\cdot]$ system, two control variables, θ and ξ are introduced. The circumferential angle θ turns about the y_{f} axis and ranges between exit angle to the entry angle $\theta \in [\theta_{\text{exit}}, \theta_{\text{entry}}]$. ξ runs along the y_{f} axis over the wheel width in the interval of $\xi \in \left[\frac{-b_{\text{w}}}{2}, \frac{b_{\text{w}}}{2}\right]$. The origin of the ${}^{\text{C}}[\cdot]$ system is at the point $(0, \xi, -r_{\text{w}})^T$ and the rotation about the y_c axis from the current local contact point ${}^{\text{C}}[\cdot]$ system to the fixed wheel ${}^{\text{FW}}[\cdot]$ system is defined as

$$ {}^{\text{FW}}\mathbf{T}_{\text{C}}(\theta) = \begin{pmatrix} \cos\theta & 0 & -\sin\theta \\ 0 & 1 & 0 \\ \sin\theta & 0 & \cos\theta \end{pmatrix}. \tag{3.1} $$

Note, that this rotation is in negative mathematical direction of rotation. Finally, the BCM angles are summarized in Table 3.2.

3.2. Reaction Forces and Torques

The main principle of the BCM algorithm is a spatial integration of the local normal and shear stress over the contact surface and the computation of all grouser reactions. The normal and shear stress depend on the wheel velocity, the wheel sinkage, the contact plane and the given soil and wheel parameters. This leads to the equations for the total three-dimensional force vector ${}^{\text{W}}\boldsymbol{f}_{\text{total}}$ and the torque vector ${}^{\text{W}}\boldsymbol{t}_{\text{total}}$ of the wheel-soil contact,

Table 3.2.: BCM angles.

Symbol	Description
θ_{exit}	Exit angle of wheel-soil contact
θ_{entry}	Entry angle of wheel-soil contact
α	Rotation angle of the wheel between the x_{f} and x_{w} axis
β	Wheel tilt angle between z_{f} and z_{p} axis
θ	Control variable in range $\theta \in [\theta_{\text{exit}}, \theta_{\text{entry}}]$
ξ	Control variable along the wheel width $\xi \in \left[\frac{-b_w}{2}, \frac{b_w}{2}\right]$

as follows

$$ {}^{\mathrm{W}}\boldsymbol{f}_{\mathrm{total}} = {}^{\mathrm{W}}\mathbf{T}_{\mathrm{FW}}\Big(\mathbf{K}_{\mathrm{Lim}}\big({}^{\mathrm{FW}}\boldsymbol{f}_{\mathrm{SC}} + {}^{\mathrm{FW}}\boldsymbol{f}_{\mathrm{G}} + {}^{\mathrm{FW}}\boldsymbol{f}_{\mathrm{D}}\big)\Big), \tag{3.2} $$

$$ {}^{\mathrm{W}}\boldsymbol{t}_{\mathrm{total}} = {}^{\mathrm{W}}\mathbf{T}_{\mathrm{FW}}\Big({}^{\mathrm{FW}}\boldsymbol{t}_{\mathrm{SC}} + {}^{\mathrm{FW}}\boldsymbol{t}_{\mathrm{G}} + {}^{\mathrm{FW}}\boldsymbol{t}_{\mathrm{D}}\Big), \tag{3.3} $$

where ${}^{\mathrm{W}}\mathbf{T}_{\mathrm{FW}}$ is the rotation matrix from the fixed wheel to the world system. ${}^{\mathrm{FW}}\boldsymbol{f}_{\mathrm{SC}}$ and ${}^{\mathrm{FW}}\boldsymbol{t}_{\mathrm{SC}}$ are force and torque vector of the contact surface, ${}^{\mathrm{FW}}\boldsymbol{f}_{\mathrm{G}}$ and ${}^{\mathrm{FW}}\boldsymbol{t}_{\mathrm{G}}$ the force and torque vector of the grousers and ${}^{\mathrm{FW}}\boldsymbol{f}_{\mathrm{D}}$, ${}^{\mathrm{FW}}\boldsymbol{t}_{\mathrm{D}}$ are the damping. $\mathbf{K}_{\mathrm{Lim}}$ is a factor which limits the vertical component of the contact reaction force. In case of an abrupt change of the wheel load, the contact reaction force need to be limited, to prevent unphysical behavior. In the following only the contact surface reactions ${}^{\mathrm{FW}}\boldsymbol{f}_{\mathrm{SC}}$ and ${}^{\mathrm{FW}}\boldsymbol{t}_{\mathrm{SC}}$ are considered. For the implementation of grouser, damping equations and $\mathbf{K}_{\mathrm{Lim}}$, the reader is referred to [3].

3.3. Contact Surface

The computation of the contact surface reaction forces and torques are realized by an integration of the stresses over the contact surface.
At the beginning, the contact detection supplies the local contact plane ${}^{\mathrm{P}}[\cdot]$ and from this, the wheel sinkage $z(\xi)$ can be obtained, which depends on the wheel tilt angle ξ. In the next step, the entry angle θ_{entry} of the wheel-soil contact is defined, as

$$ \theta_{\mathrm{entry}} = \operatorname{sgn}\left({}^{\mathrm{FW}}v_{\mathrm{f},x}\right) \begin{cases} \arccos\left(1 - \frac{z(\xi)}{r_{\mathrm{w}}}\right), & \forall z(\xi) < r_{\mathrm{w}} \\ \frac{\pi}{2}, & \forall z(\xi) \geq r_{\mathrm{w}} \end{cases} \text{ with } \operatorname{sgn}(0) = 1. \tag{3.4} $$

Note that, ${}^{\mathrm{FW}}v_{\mathrm{f},x}$ is the longitudinal translational velocity of the wheel, thus θ_{entry} always points in the direction of the longitudinal wheel motion. After that, the velocity dependent exit angle θ_{exit} can be obtained as

$$ \theta_{\mathrm{exit}} = -\theta_{\mathrm{entry}}\left(\eta + (1-\eta)\, e^{-\frac{\left|{}^{\mathrm{FW}}v_{\mathrm{f},x}\right|}{V_{\mathrm{CA}}}}\right). \tag{3.5} $$

When the translational velocity ${}^{\mathrm{FW}}v_{\mathrm{f},x} = 0$, the exit angle is $\theta_{\mathrm{exit}} = -\theta_{\mathrm{entry}}$. On the other hand, when ${}^{\mathrm{FW}}v_{\mathrm{f},x}$ is high, the exit angle converges to $\theta_{\mathrm{exit}} = -\eta\theta_{\mathrm{entry}}$. The BCM parameter η sets the minimal θ_{exit} and with the parameter V_{CA}, the rapidity of the convergence can be adjusted.

For the local normal stress computation, the assumption is a quadratic normal stress distribution over the wheel-soil contact surface, as

$$ {}^{\mathrm{C}}\sigma\left(\theta,\xi\right) = \theta^2 c_1 + \theta c_2 + c_3 \tag{3.6} $$

where $c_1,\ c_2,\ c_3$ are the coefficients of the quadratic function. They can be obtained by solving a system of equations which includes the original pressure-sinkage Equation (2.1) from Bekker [45]. In order to compute the shear stress at each contact point, the three-dimensional slip velocity vector at the contact point must be calculated first which is defined as

$$ {}^{\mathrm{C}}\boldsymbol{v} = {}^{\mathrm{C}}\mathbf{T}_{\mathrm{FW}}\left({}^{\mathrm{FW}}\boldsymbol{v}_{\mathrm{f}} + {}^{\mathrm{FW}}\boldsymbol{\omega} \times {}^{\mathrm{FW}}\boldsymbol{r}_{\mathrm{fc}}\right), \tag{3.7} $$

with ${}^{\mathrm{C}}\mathbf{T}_{\mathrm{FW}}$ as the rotation matrix from the fixed wheel system to the current contact point which can be obtained from Equation (3.1). ${}^{\mathrm{FW}}\boldsymbol{v}_{\mathrm{f}}$ is the tangential velocity vector of the wheel, while ${}^{\mathrm{FW}}\boldsymbol{\omega}$ is the rotational velocity of the wheel in the fixed wheel system. The vector from the origin of the fixed wheel system to each contact point ${}^{\mathrm{FW}}\boldsymbol{r}_{\mathrm{fc}}$ is defined as

$$ {}^{\mathrm{FW}}\boldsymbol{r}_{\mathrm{fc}} = {}^{\mathrm{FW}}\mathbf{T}_{\mathrm{C}}\left(\theta\right)\begin{pmatrix} 0 \\ \xi \\ -r_{\mathrm{w}} \end{pmatrix}. \tag{3.8} $$

After that, the local shear stress calculation at each contact point yields

$$ {}^{\mathrm{C}}\tau_x\left(\theta,\xi\right) = -\operatorname{sgn}\left({}^{\mathrm{C}}v_x\right)\tau_{\max}\left(1 - e^{\frac{\left|{}^{\mathrm{C}}v_x\right|}{V_{\mathrm{J}}}}\right), \tag{3.9} $$

$$ {}^{\mathrm{C}}\tau_y\left(\theta,\xi\right) = -\operatorname{sgn}\left({}^{\mathrm{C}}v_y\right)\tau_{\max}\left(1 - e^{\frac{\left|{}^{\mathrm{C}}v_y\right|}{V_{\mathrm{J}}}}\right), \tag{3.10} $$

where ${}^{\mathrm{C}}\tau_x$ is the local shear stress in longitudinal direction, whereas ${}^{\mathrm{C}}\tau_y$ is the shear stress in axial direction. ${}^{\mathrm{C}}\boldsymbol{v} = \left({}^{\mathrm{C}}v_x, {}^{\mathrm{C}}v_y\right)^T$ is the tangential slip velocity from Equation 3.7.

The shear stress computation is a modification of the empirical equation of JANOSI and HANAMOTO (2.5) which has been discussed previously. Instead of the shear displacement j, the slip velocity is used in order to predict the shear stress. Additionally, the BCM parameter V_J is used instead of the horizontal shear modulus. The maximal shear stress ${}^{\mathrm{C}}\tau_{\max}(\theta,\xi)$ at each contact point is based on the MOHR-COULOMB failure criterion cf. Equation (2.4), as

$$ {}^{\mathrm{C}}\tau_{\max}(\theta,\xi) = \Big[c + \tan\phi \; {}^{\mathrm{C}}\sigma(\theta,\xi)\Big]. \tag{3.11} $$

This assumption leads to a pure velocity-dependent relationship between the normal and shear stress because the shear stress is no longer dependent on the shear displacement j. As a consequence, the static friction is cannot be depicted from the BCM algorithm. However, the advantage is a computation of the contact reaction forces and torques only with the information of the current time step and without any data of previous time steps which makes the calculation of the model significantly faster.
With the normal ${}^{\mathrm{C}}\sigma$ and shear stress ${}^{\mathrm{C}}\boldsymbol{\tau}$ at the current contact point, the infinitesimal load ${}^{\mathrm{C}}\boldsymbol{q}_{\mathrm{SC}}(\theta,\xi)$ can be obtained, as

$$ {}^{\mathrm{C}}\boldsymbol{q}_{\mathrm{SC}}(\theta,\xi) = \begin{pmatrix} {}^{\mathrm{C}}\tau_x(\theta,\xi) \\ {}^{\mathrm{C}}\tau_y(\theta,\xi) \\ {}^{\mathrm{C}}\sigma(\theta,\xi) \end{pmatrix}. \tag{3.12} $$

Finally, the force over the contact surface ${}^{\mathrm{FW}}\boldsymbol{f}_{\mathrm{SC}}$ can be integrated with the infinitesimal load ${}^{\mathrm{C}}\boldsymbol{q}_{\mathrm{SC}}(\theta,\xi)$ and the infinitesimal surface patch $\mathrm{d}\theta\mathrm{d}\xi$ as

$$ {}^{\mathrm{FW}}\boldsymbol{f}_{\mathrm{SC}} = r_{\mathrm{w}} \int_{\frac{-b_{\mathrm{w}}}{2}}^{\frac{b_{\mathrm{w}}}{2}} \int_{\theta_{\mathrm{exit}}}^{\theta_{\mathrm{entry}}} {}^{\mathrm{FW}}\mathbf{T}_{\mathrm{C}} \; {}^{\mathrm{C}}\boldsymbol{q}_{\mathrm{SC}}(\theta,\xi)\,\mathrm{d}\theta\mathrm{d}\xi. \tag{3.13} $$

The contact surface torque vector ${}^{\mathrm{FW}}\boldsymbol{t}_{\mathrm{SC}}$ is defined as the cross product of the distance from the center of the wheel to the contact point ${}^{\mathrm{FW}}\boldsymbol{r}_{\mathrm{fc}}$ and the infinitesimal load

${}^{\mathrm{C}}\boldsymbol{q}_{\mathrm{SC}}(\theta,\xi)$ which yields

$$ {}^{\mathrm{FW}}\boldsymbol{t}_{\mathrm{SC}} = r_{\mathrm{w}} \int_{\frac{-b_{\mathrm{w}}}{2}}^{\frac{b_{\mathrm{w}}}{2}} \int_{\theta_{\mathrm{exit}}}^{\theta_{\mathrm{entry}}} {}^{\mathrm{FW}}\boldsymbol{r}_{\mathrm{fc}}(\theta,\xi) \times \left[{}^{\mathrm{FW}}\mathbf{T}_{\mathrm{C}} \; {}^{\mathrm{C}}\boldsymbol{q}_{\mathrm{SC}}(\theta,\xi) \right] \mathrm{d}\theta \mathrm{d}\xi. \tag{3.14} $$

3.4. Discretization of Contact Surface

In order to realize the integration of the stresses over the contact surface for simulation, the contact surface is discretized to contact patches. These contact patches are described in the ${}^{\mathrm{C}}[\cdot]$ system and the position of each contact patch is described as a pair of the discrete position θ_i and ξ_j on the contact surface. The position values of each contact patch can be defined as

$$ \theta_i = \left(\theta_{\mathrm{exit}} + \frac{\Delta\theta}{2} \right) + (i-1) \;\; \Delta\theta \qquad\qquad i \in \{1,...,n\} \tag{3.15} $$

and

$$ \xi_j = \left(-\frac{b_{\mathrm{w}}}{2} + \frac{\Delta\xi}{2} \right) + (j-1) \;\; \Delta\xi \qquad\qquad j \in \{1,...,m\}. \tag{3.16} $$

The contact surface is discretized in $N_{\mathrm{SC}} = n \cdot m$ contact patches, where n is the number of contact patches along the discrete angle θ_i in the interval of $[\theta_{\mathrm{exit}}, \theta_{\mathrm{entry}}]$. m are the contact patches along the discrete width ξ_j in the interval of $\left[\frac{-b_w}{2}, \frac{b_w}{2}\right]$. $\Delta\theta$ is the contact patch length along the discrete angle θ_i, as well as $\Delta\xi$ represents the contact patch width along ξ_j and thus, this yields

$$ \Delta\theta = \frac{\theta_{\mathrm{exit}} + \theta_{\mathrm{entry}}}{n} \tag{3.17} $$

and

$$ \Delta\xi = \frac{b_{\mathrm{w}}}{m}. \tag{3.18} $$

As a result of that, n and m are the resolution of the contact surface. The higher the value N_{SC}, the higher the density of contact patches on the surface and the smaller the length $\Delta\theta$ and width $\Delta\xi$ of the contact patch.

Each contact patch is now evaluated by using the analytical equations of 3.3 at its indi-

vidual position with angles θ_i and ξ_j. For the normal stress ${}^{\mathrm{C}}\sigma_z(\theta_i)$ Equation (3.6), for the local slip velocity ${}^{\mathrm{C}}\boldsymbol{v}\left(\theta_i, \xi_j\right)$ Equation (3.7) and for the shear stress of the current contact patch Equations (3.9), (3.10) and (3.11) are used. The normal and shear stress are used to obtain the discrete load of each contact patch, as

$$
{}^{\mathrm{C}}\boldsymbol{q}_{\mathrm{SC}}\left(\theta_i, \xi_j\right) = \begin{pmatrix} {}^{\mathrm{C}}\tau_x\left(\theta_i, \xi_j\right) \\ {}^{\mathrm{C}}\tau_y\left(\theta_i, \xi_j\right) \\ {}^{\mathrm{C}}\sigma\left(\theta_i, \xi_j\right) \end{pmatrix}. \tag{3.19}
$$

Finally, the contact surface reactions forces and the torques, can be calculated by approximating the equations (3.13) and (3.14) through the summation of the contact patch loads as

$$
\begin{aligned}
{}^{\mathrm{FW}}\boldsymbol{f}_{\mathrm{SC}} &= r_{\mathrm{w}} \int_{\frac{-b_{\mathrm{w}}}{2}}^{\frac{b_{\mathrm{w}}}{2}} \int_{\theta_{\mathrm{exit}}}^{\theta_{\mathrm{entry}}} {}^{\mathrm{FW}}\mathbf{T}_{\mathrm{C}}\ {}^{\mathrm{C}}\boldsymbol{q}_{\mathrm{SC}}\left(\theta, \xi\right) d\theta d\xi \\
&\approx r_{\mathrm{w}} \sum_{j=1}^{m} \sum_{i=1}^{n} {}^{\mathrm{FW}}\mathbf{T}_{\mathrm{C}}\left(\theta_i\right)\ {}^{\mathrm{C}}\boldsymbol{q}_{\mathrm{SC}}\left(\theta_i, \xi_j\right) \Delta\theta\Delta\xi,
\end{aligned} \tag{3.20}
$$

and

$$
\begin{aligned}
{}^{\mathrm{FW}}\boldsymbol{t}_{\mathrm{SC}} &= r_{\mathrm{w}} \int_{\frac{-b_{\mathrm{w}}}{2}}^{\frac{b_{\mathrm{w}}}{2}} \int_{\theta_{\mathrm{exit}}}^{\theta_{\mathrm{entry}}} {}^{\mathrm{FW}}\boldsymbol{r}_{\mathrm{fc}}\left(\theta, \xi\right) \times \left[{}^{\mathrm{FW}}\mathbf{T}_{\mathrm{C}}\ {}^{\mathrm{C}}\boldsymbol{q}_{\mathrm{SC}}\left(\theta, \xi\right)\right] d\theta d\xi \\
&\approx r_{\mathrm{w}} \sum_{j=1}^{m} \sum_{i=1}^{n} {}^{\mathrm{FW}}\boldsymbol{r}_{\mathrm{fc}}\left(\theta_i, \xi_j\right) \times \left[{}^{\mathrm{FW}}\mathbf{T}_{\mathrm{C}}\left(\theta_i\right)\ {}^{\mathrm{C}}\boldsymbol{q}_{\mathrm{SC}}\left(\theta_i, \xi_j\right)\right] \Delta\theta\Delta\xi.
\end{aligned} \tag{3.21}
$$

The rotation matrix ${}^{\mathrm{C}}\mathbf{T}_{\mathrm{FW}}\left(\theta_i\right)$ and the vector ${}^{\mathrm{FW}}\boldsymbol{r}_{\mathrm{fc}}\left(\xi_j\right)$ are derived from Equation (3.1) and Equation (3.8) which must be evaluated at each contact patch $\left(\theta_i, \xi_j\right)$ which yields

$$
{}^{\mathrm{FW}}\mathbf{T}_{\mathrm{C}}\left(\theta_i\right) = \begin{pmatrix} \cos\theta_i & 0 & -\sin\theta_i \\ 0 & 1 & 0 \\ \sin\theta_i & 0 & \cos\theta_i \end{pmatrix}. \tag{3.22}
$$

and

$$ {}^{\mathrm{FW}}\boldsymbol{r}_{\mathrm{fc}}\left(\theta_i, \xi_j\right) = {}^{\mathrm{FW}}\mathbf{T}_{\mathrm{C}}\left(\theta_i\right) \begin{pmatrix} 0 \\ \xi_j \\ -r_{\mathrm{w}} \end{pmatrix}. \tag{3.23} $$

4. Bristle Friction Modeling in BCM

The shear stress model of the existing BCM mainly considers the behavior of loose soil, as loose, granular sand [45]. However, if the soil is compressed the existing BCM does not model the behavior adequately. In case of a wheel-soil contact the soil is compacted by the wheel load and the capability of the soil to absorb shear stress increases. At a certain point however, the compressed soil failures and from this, the soil's capability to absorb shear stress decreases again. From this behavior, the idea arose to implement the bristle friction model approach as the shear stress model to the existing BCM, because the strain of a bristle follows a similar principle. A bristle, in the static regime, absorbs an increasing value of deflection and when the threshold is reached the bristle changes into the kinetic regime, from this moment the bristle absorb less deflection.
In order to adapt, the extended bristle friction model, which is introduced in 2.2.3, into the existing BCM several modifications need to be done in the algorithm firstly. These modifications are introduced in the beginning of this chapter in 4.1. Furthermore, a suitable distribution and fixation of the bristles have to be found in order to model the wheel-soil contact adequately. Within this thesis two implementations with different fixation and distribution of bristles have been elaborated, which are introduced in 4.3 and 4.4.

4.1. General Modifications on Modeling

As already mentioned, several modification of the existing BCM algorithm and the extended bristle friction model need to be done firstly. For the new bristle implementations, Equation (3.2) of total reaction forces and the Equation (3.3) of total reaction torques

are new defined, as

$$ {}^{\mathrm{W}}\boldsymbol{f}_{\mathrm{total}} = {}^{\mathrm{W}}\mathbf{T}_{\mathrm{FW}}\Big(\mathbf{K}_{\mathrm{Lim}}\big({}^{\mathrm{FW}}\boldsymbol{f}_{\mathrm{SC}}\big)\Big), \tag{4.1} $$

$$ {}^{\mathrm{W}}\boldsymbol{t}_{\mathrm{total}} = {}^{\mathrm{W}}\mathbf{T}_{\mathrm{FW}}\Big({}^{\mathrm{FW}}\boldsymbol{t}_{\mathrm{SC}}\Big). \tag{4.2} $$

The new Equations show, that the term of grousers and the damping is omitted. The grouser significantly influence the tractive performance of the wheel. In the new bristle approaches however, the complete tractive performance will only be depend on the bristles. As a result, the influence of the grouser must be already included in the bristles and thus, the parameterization of the bristles will be depend on grouser properties, as shape, size and height. The original damping term of BCM is omitted, because the damping term of the bristle friction model, as in Equation (2.10), is used. As shown in 5.3, this damping term achieves the better results.

The remaining terms $\boldsymbol{f}_{\mathrm{SC}}$ and $\boldsymbol{t}_{\mathrm{SC}}$ are modified in order to integrate the bristle friction model. The first equations for the calculation of the entry and exit angle of the wheel contact surface (Equation (3.4) and Equation (3.5)), the normal stress (Equation (3.6)) and the slip velocity vector (Equation (3.7)) can be adopted from the original BCM.

For the shear stress computation, a bristle is set to each contact patch of the discretized wheel-soil contact surface. Each bristle in the new BCM needs as inputs the tangential velocity $\boldsymbol{v}_{\mathrm{t}}$ and the normal stress σ. The latter is used instead of the normal force, because the normal stress can be directly obtained from the original algorithm. For the tangential velocity ${}^{\mathrm{C}}\boldsymbol{v}_{\mathrm{t}}$ the first two entries of the slip velocity vector ${}^{\mathrm{C}}\boldsymbol{v}$ evaluated at the corresponding bristle position can be used, as

$$ {}^{\mathrm{C}}\boldsymbol{v}_{\mathrm{t}}\left(\theta_i, \xi_j\right) = \begin{pmatrix} {}^{\mathrm{C}}v_{\mathrm{x}}\left(\theta_i, \xi_j\right) \\ {}^{\mathrm{C}}v_{\mathrm{y}}\left(\theta_i, \xi_j\right) \end{pmatrix}, \tag{4.3} $$

where ${}^{\mathrm{C}}v_{\mathrm{x}}$ is the longitudinal slip velocity and ${}^{\mathrm{C}}v_{\mathrm{y}}$ the axial slip velocity. After this, the maximum bristle deflection of the bristle can be determined, as

$$ {}^{\mathrm{C}}s_{\max}\left(\theta_i, \xi_j\right) = \begin{cases} {}^{\mathrm{C}}s_{\mathrm{k}\max}\left(\theta_i, \xi_j\right) = \frac{\mu_{\mathrm{k}}{}^{\mathrm{C}}\sigma(\theta_i, \xi_j)}{k_{\mathrm{b}}}, & \text{if } \left|\left|{}^{\mathrm{C}}\boldsymbol{v}_{\mathrm{t}}\left(\theta_i, \xi_j\right)\right|\right| > v_{\mathrm{d}} \\ {}^{\mathrm{C}}s_{\mathrm{s}\max}\left(\theta_i, \xi_j\right) = \frac{\mu_{\mathrm{s}}{}^{\mathrm{C}}\sigma(\theta_i, \xi_j)}{k_{\mathrm{b}}}, & \text{if } \left|\left|{}^{\mathrm{C}}\boldsymbol{v}_{\mathrm{t}}\left(\theta_i, \xi_j\right)\right|\right| \leq v_{\mathrm{d}}. \end{cases} \tag{4.4} $$

Note that this equation refers to Equation (2.9) with the difference in using normal stress instead of normal force. As already mentioned in 2.2.3 , v_d is the velocity deadband which is the boundary between the static and the kinetic friction regime. Through the case analysis in Equation 4.4, it can be determined whether the considered bristle is within the static or kinetic regime.

Due to the modification of using normal stress the parameter units of bristle stiffness k_b and the bristle damping c_b are changed and the parameters must be redefined. Suitable values for the bristle stiffness and damping are extensively discussed in the papers [12] and [28]. However, these discussions consider the original coefficients, which are not related to an unit area as they are in the BCM implementations. For this reason, suitable values for damping and stiffness are briefly investigated in 5.1.

The static friction coefficient μ_s can be assumed as the maximum possible friction case, and therefore the knowledge of the maximum tangential stress from the MOHR-COULOMB failure criterion, respectively Equation (2.4), is used for the determination of μ_s and yields

$$\mu_\mathrm{s} = \frac{\tau}{\sigma} = \frac{{}^\mathrm{C}\tau_\mathrm{max}\left(\theta_i, \xi_j\right)}{{}^\mathrm{C}\sigma\left(\theta_i, \xi_j\right)} = \frac{c + {}^\mathrm{C}\sigma\left(\theta_i, \xi_j\right)\tan\phi}{{}^\mathrm{C}\sigma\left(\theta_i, \xi_j\right)}. \tag{4.5}$$

Due to the friction limitation, it can be assumed that always $\mu_\mathrm{k} < \mu_\mathrm{s}$. However, μ_s is not constant because it depends on σ which is location- and time-variable and thus, μ_k must be depended on σ as well. In order to ensure that μ_k does not exceed μ_s, a new parameter k_kin as a reducing factor of the static friction coefficient is introduced in the following way

$$\mu_\mathrm{k} = k_\mathrm{kin}\ \mu_\mathrm{s} = k_\mathrm{kin}\ \frac{{}^\mathrm{C}\tau_\mathrm{max}\left(\theta_i, \xi_j\right)}{{}^\mathrm{C}\sigma\left(\theta_i, \xi_j\right)}. \tag{4.6}$$

As a consequence, the equation of the maximum bristle deflection (2.9) is now modified as follows

$${}^\mathrm{C}s_\mathrm{max}\left(\theta_i, \xi_j\right) = \begin{cases} {}^\mathrm{C}s_\mathrm{k\,max}\left(\theta_i, \xi_j\right) = \frac{k_\mathrm{kin}\ {}^\mathrm{C}\tau_\mathrm{max}(\theta_i, \xi_j)}{k_\mathrm{b}}, & \text{if } \left|\left|{}^\mathrm{C}\boldsymbol{v}_\mathrm{t}\left(\theta_i, \xi_j\right)\right|\right| > v_\mathrm{d} \\ {}^\mathrm{C}s_\mathrm{s\,max}\left(\theta_i, \xi_j\right) = \frac{{}^\mathrm{C}\tau_\mathrm{max}(\theta_i, \xi_j)}{k_\mathrm{b}}, & \text{if } \left|\left|{}^\mathrm{C}\boldsymbol{v}_\mathrm{t}\left(\theta_i, \xi_j\right)\right|\right| \leq v_\mathrm{d}. \end{cases} \tag{4.7}$$

This modification is used for both bristle friction model implementations with the benefit that only k_kin must be determined. k_kin depends on the soil, as well as on the wheel,

because the k_{kin} stands for the residual tractive performance of the wheel-soil contact. As a result, the value of k_{kin} is also influenced by the wheel grousers. Therefore, the parameter k_{kin} must be individually identified by experiment for each wheel type.

After the maximum bristle deflection is determined, the time integration of ${}^{\text{C}}\boldsymbol{v}_{\text{t}}$ follows in order to obtain the bristle deflection, for this Equation (2.9) is used, as

$$
{}^{\text{C}}\boldsymbol{s} = \begin{pmatrix} {}^{\text{C}}s_x\left(\theta_i, \xi_j\right) \\ {}^{\text{C}}s_y\left(\theta_i, \xi_j\right) \end{pmatrix} = \begin{cases} {}^{\text{C}}\boldsymbol{s}_0\left(\theta_i, \xi_j\right) + \int_{t_0}^{t} {}^{\text{C}}\boldsymbol{v}_{\text{t}}\left(\theta_i, \xi_j\right) dt, & \text{if } \left|\left|{}^{\text{C}}\boldsymbol{s}\left(\theta_i, \xi_j\right)\right|\right| < {}^{\text{C}}s_{\max}\left(\theta_i, \xi_j\right) \\ {}^{\text{C}}s_{\max} \frac{{}^{\text{C}}\boldsymbol{v}_{\text{t}}(\theta_i, \xi_j)}{||{}^{\text{C}}\boldsymbol{v}_{\text{t}}(\theta_i, \xi_j)||}, & \text{if } \left|\left|{}^{\text{C}}\boldsymbol{s}\left(\theta_i, \xi_j\right)\right|\right| \geq {}^{\text{C}}s_{\max}\left(\theta_i, \xi_j\right). \end{cases} \tag{4.8}
$$

Where ${}^{\text{C}}\boldsymbol{s}$ is the resulting bristle deflection vector and ${}^{\text{C}}\boldsymbol{s}_0$ the start deflection of each bristle. In case of the BCM simulation it is assumed that ${}^{\text{C}}\boldsymbol{s}_0 = \boldsymbol{0}$.

After the calculation of the bristle deflection, the shear stress vector of each bristle ${}^{\text{C}}\boldsymbol{\tau}$ can be determined as

$$
{}^{\text{C}}\boldsymbol{\tau}\left(\theta_i, \xi_j\right) = \begin{pmatrix} {}^{\text{C}}\tau_x\left(\theta_i, \xi_j\right) \\ {}^{\text{C}}\tau_y\left(\theta_i, \xi_j\right) \end{pmatrix} = -k_{\text{b}} \begin{pmatrix} {}^{\text{C}}s_x\left(\theta_i, \xi_j\right) \\ {}^{\text{C}}s_y\left(\theta_i, \xi_j\right) \end{pmatrix} - c_{\text{b}} \begin{pmatrix} {}^{\text{C}}v_{\text{t},x}\left(\theta_i, \xi_j\right) \\ {}^{\text{C}}v_{\text{t},y}\left(\theta_i, \xi_j\right) \end{pmatrix}. \tag{4.9}
$$

Note that for the damping term, the tangential velocity $\boldsymbol{v}_{\text{t}}(t)$ is used instead of using $\dot{\boldsymbol{s}}(t)$ as in Equation (2.10). The advantage is that $\boldsymbol{v}_{\text{t}}(t)$ is already computed in contrast to $\dot{\boldsymbol{s}}(t)$ which must be numerical derived. However, Equation (4.8) shows that $\boldsymbol{v}_{\text{t}}$ can only be used as the derivative when Equation (4.8) is in the first case. This loss of accuracy is accepted due to the significantly lower computational effort by using $\boldsymbol{v}_{\text{t}}$.

After this, the normal and shear stress are used to obtain the discrete load of each bristle, as

$$
{}^{\text{C}}\boldsymbol{q}_{\text{SC}}\left(\theta_i, \xi_j\right) = \begin{pmatrix} {}^{\text{C}}\tau_x\left(\theta_i, \xi_j\right) \\ {}^{\text{C}}\tau_y\left(\theta_i, \xi_j\right) \\ {}^{\text{C}}\sigma\left(\theta_i, \xi_j\right) \end{pmatrix}. \tag{4.10}
$$

The discrete loads of all bristles are summarized in order to obtain the surface contact reactions $\boldsymbol{f}_{\text{SC}}$ and $\boldsymbol{t}_{\text{SC}}$ of the discrete wheel-soil contact surface.

The parameters for the contact surface discretization n and m, which are already used in the original BCM implementation are now similar to the number of bristles N_{Bristles}. These parameters are crucial for the computation effort, as well as for the accuracy of

the results of the model. Thus, on the one side, the bristle number must be high enough to obtain sufficient results and on the other side, the number must be low enough for a reasonable computation effort - also with regard to real-time capabilities. For this reason, the model is simulated with different bristle numbers in 5.2, in order to find an adequate compromise between computation time and accuracy. For a better overview, all modified or new bristle friction parameters of the new BCM extensions are summarized in Table 4.1.

Table 4.1.: Bristle Parameter of BCM extensions.

Parameter	Symbol	Unit
Bristle stiffness per unit area	k_b	$\mathrm{N/m^3}$
Bristle damping per unit area	c_b	$\mathrm{Ns/m^3}$
Kinetic coefficient	k_kin	–
Velocity Deadband (Threshold)	v_d	$\mathrm{m/s}$
Resolution along the angle θ_i or $\tilde{\theta}_i$	n	–
Resolution along the width ξ_j	m	–

4.2. General Modifications on Implementation

Due to the time integration of Equation (4.8) it is necessary to have information about the previous time steps. However, the current BCM implementation is executed by the connected MBS simulation solver at each time step independently, without using any data from a previous time step.

Through the implementation of the bristle friction model it is necessary to implement a time integration block outside the BCM algorithm as it can be seen in Figure 4.1. The benefits of a simplified computation by using only the information of the current time step which is mentioned in Section 3.3 no longer apply. On the other hand, the shear stress is now temporally dependent which conforms more closely with reality. Nevertheless, this inevitably results in an increased computational effort.

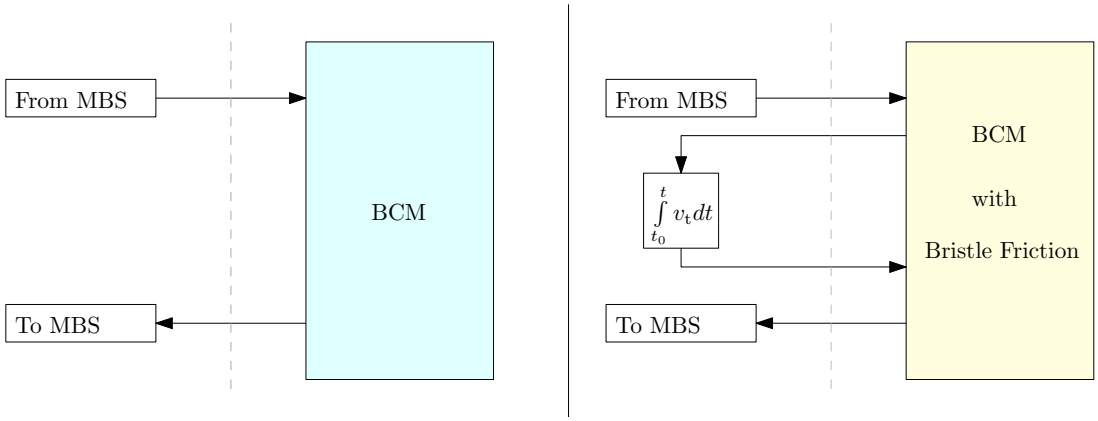

Figure 4.1.: Additional time integration by using the bristle friction model. Left: original BCM, right: BCM with bristle friction model.

4.3. Bristles Fixed on the Contact Surface (BFCS)

In this approach, the bristles are fixed to the contact surface as Figure 4.2 illustrates. In order to achieve a better understanding of the method, the principle can be thought of as a brush. In this case, the contact surface represents the brush and the wheel slides over it. When the wheel starts to move it pulls the bristles of this brush and thereby, they are strained. Note that the brush example has its limitations, because the assumed bristles do not have any spatial dimension.

The bristles are placed uniformly in the discretized contact surface, as Figure 4.3 shows. Each bristle is positioned in the center of one contact patch and thus, the number of contact patches N_{SC} is equal to the number of bristles N_{Bristles}. The advantage of this

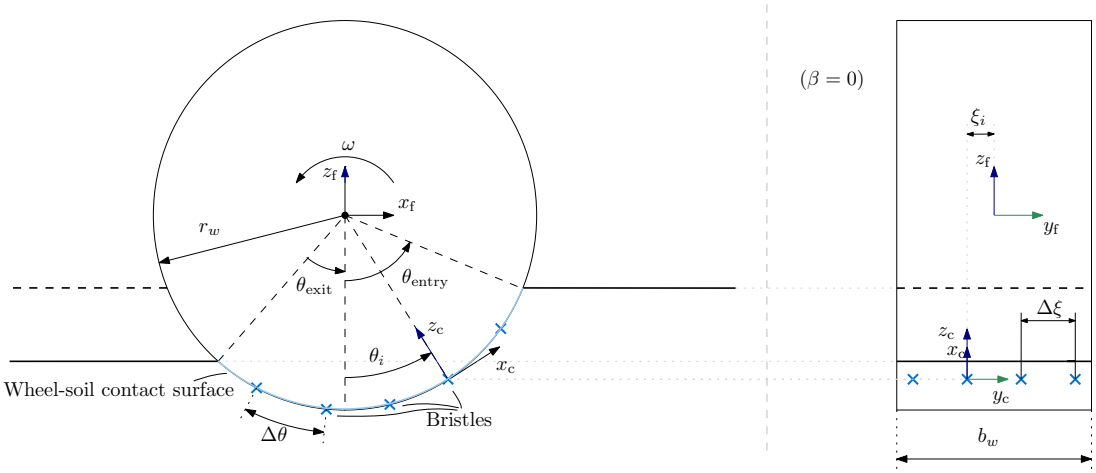

Figure 4.2.: Bristles fixed to the contact surface.

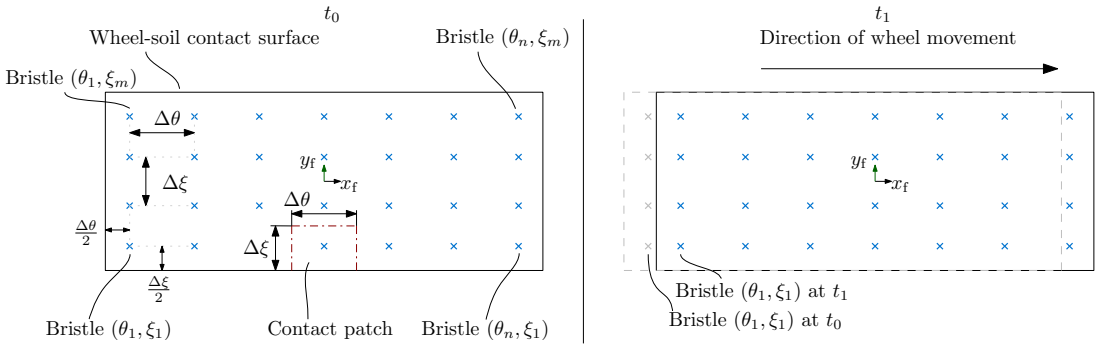

Figure 4.3.: Bristles fixed to the contact surface in top view.

bristle positioning is, that the local contact point ${}^{\mathrm{C}}[\cdot]$ coordinate system of the original BCM can be completely adopted.

On the other hand, this algorithm is disadvantageous when the size of the contact surface is changing during the simulation. A variation of contact surface size changes, among others, the exit angle θ_{exit} and the entry angle θ_{entry} and thus, the step sizes $\Delta\theta$ and $\Delta\xi$ are changed as well. This leads to a changing size of the contact patches, the resolution of the discretization and the bristle distance, as can be seen in Figure 4.4. At time point t_0 the sinkage of the wheel is higher than at time point t_1. As a result, the length of the wheel-soil contact surface decreases from t_0 to t_1 and the bristles are at different positions within the wheel surface form t_0 to t_1. This means, that different tangential velocities $\boldsymbol{v}_{\mathrm{t}}$ are used in t_0 and t_1 for the bristle deflection computation, which increase the oscillation of the contact body as results show in 5.1.

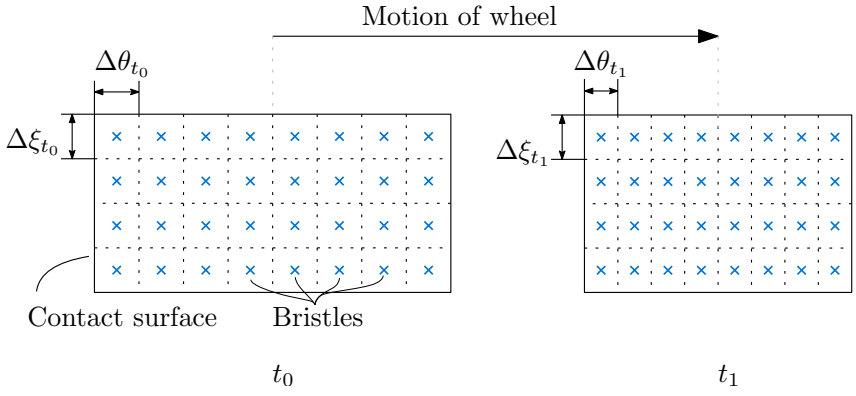

Figure 4.4.: Changing size of the wheel-soil contact surface from t_0 to t_1 (in top view).

4.4. Bristles Fixed on the Wheel Surface (BFEW)

In order to prevent the changing bristle position, an alternative approach was developed. This second bristle friction implementation assumes that each bristle is placed on a fixed location on the wheel surface. The bristles are homogeneously distributed over the entire wheel surface and not only within the wheel-soil contact surface.

However, it is necessary to define a new coordinate system for the bristles, the ${}^{\tilde{\mathrm{C}}}[\cdot]$ coordinate system. Starting point of the bristle distribution is α_{B}, which is obtained from the rotation angle between the ${}^{\mathrm{W}}[\cdot]$ system and the fixed wheel system ${}^{\mathrm{FW}}[\cdot]$ around the common y-axis y_{f}, y_{w}. Due to α_{B}, it is ensured that each bristle remains on its position on the wheel surface. As already mentioned in 3, the position and velocity of the wheel is determined by the connected MBS and thus, the wheel rotation can directly be obtained. Thus angle α_{B} inherits the wheel rotation and it is defined that the base is the negative unit vector ${}^{\tilde{\mathrm{C}}}\mathbf{e}_z$ with the interval

$$\alpha_{\mathrm{B}} \in [0, 2\pi]\,. \tag{4.11}$$

Now the new bristle ${}^{\tilde{\mathrm{C}}}[\cdot]$ system is defined with the rotation matrix ${}^{\tilde{\mathrm{C}}}\mathbf{T}_{\mathrm{FW}}\left(\tilde{\theta}_i\right)$ as

$${}^{\tilde{\mathrm{C}}}\mathbf{T}_{\mathrm{FW}}\left(\tilde{\theta}_i\right) = \begin{pmatrix} \cos\left(\alpha_{\mathrm{B}} + \tilde{\theta}_i\right) & 0 & -\sin\left(\alpha_{\mathrm{B}} + \tilde{\theta}_i\right) \\ 0 & 1 & 0 \\ \sin\left(\alpha_{\mathrm{B}} + \tilde{\theta}_i\right) & 0 & \cos\left(\alpha_{\mathrm{B}} + \tilde{\theta}_i\right) \end{pmatrix}, \tag{4.12}$$

and vector ${}^{\mathrm{FW}}\boldsymbol{r}_{\mathrm{f}\tilde{\mathrm{c}}}\left(\tilde{\theta}_i, \xi_j\right)$ as

$${}^{\mathrm{FW}}\boldsymbol{r}_{\mathrm{f}\tilde{\mathrm{c}}}\left(\tilde{\theta}_i, \xi_j\right) = {}^{\tilde{\mathrm{C}}}\mathbf{T}_{\mathrm{FW}}\left(\tilde{\theta}_i\right) \begin{pmatrix} 0 \\ \xi_j \\ -r_{\mathrm{w}} \end{pmatrix}. \tag{4.13}$$

$\tilde{\theta}_i$ is the new definition of the bristle position around the ${}^{\mathrm{FW}}y$-axis as

$$\tilde{\theta}_i = \left(\alpha_{\mathrm{B}} + \frac{\Delta\tilde{\theta}}{2}\right) + (i+1)\ \Delta\tilde{\theta} \qquad\qquad i \in \{1, ..., n\} \tag{4.14}$$

and the position along the width ξ_j is inherited from the original BCM implementation

$$\xi_j = \left(-\frac{b_\mathrm{w}}{2} + \frac{\Delta\xi}{2}\right) + (j+1)\ \Delta\xi \qquad\qquad j \in \{1, ..., m\}. \tag{4.15}$$

The contact patch size, respectively the distances between each bristle yields

$$\Delta\tilde{\theta} = \frac{2\pi}{n}, \tag{4.16}$$

$$\Delta\xi = \frac{b_\mathrm{w}}{m}. \tag{4.17}$$

$\Delta\tilde{\theta}$ is independent from the entry angle θ_entry and the exit angle θ_exit and thus the size of each contact patch is constant during simulation. The bristles are homogeneously distributed on the entire wheel surface instead of a distribution only within the wheel-soil contact surface. The number of bristles is $N_\mathrm{Bristles} = n \cdot m$, where n is the number of bristles around the wheel circumference and m the number along the wheel width. For better understanding, the bristle positioning is illustrated in Figure 4.5. In addition, it can be seen that each bristle has a fixed relative position to α_B and thus, the bristle can be either in contact with the soil or outside the contact surface.
Figure 4.6 shows the Bristle $\left(\tilde{\theta}_3, \xi_3\right)$ at different times during the rotation of the wheel. Every time when the bristle enters the contact surface, it will be strained and only within that time (t_2 in Figure 4.6), the bristle contributes a portion to the total shear stress. When the bristle leaves the surface it will be discharged again. In this case (t_1 and t_3 in Figure 4.6), the bristle contributes no portion to the resulting reaction. Furthermore,

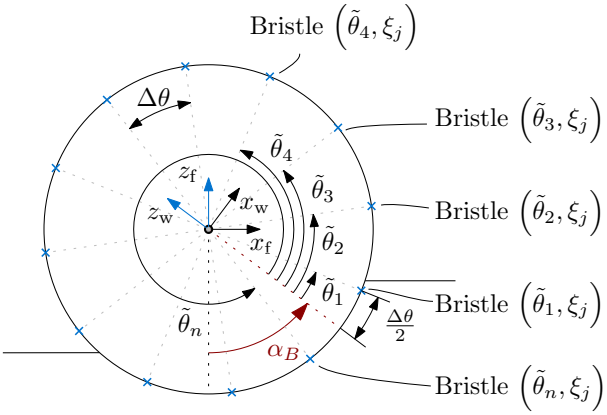

Figure 4.5.: Homogeneous wheel fixed bristle positioning.

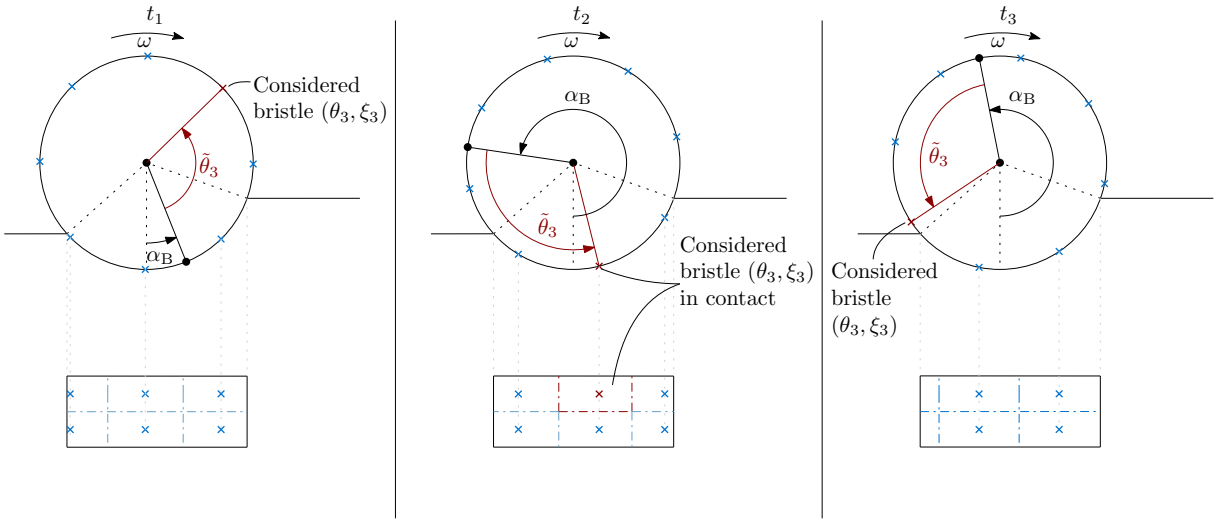

Figure 4.6.: Bristles fixed on the wheel surface (Top: side view, bottom: top view).
Left: time t_1; the considered bristle is outside the contact surface.
Center: time t_2; the considered bristle has entered the contact surface.
Right: time t_3; the considered bristle has left the contact surface.

Figure 4.6 (lower) shows that the numbers of bristles which are within the contact surface can be changing during the simulation. At time t_1 and t_2 six bristles are within the contact surface, whereas at time t_3, only four bristles are currently in contact with the soil. This leads to an additional error in the simulation. For this reason, the contact patch resolution, respectively the number of bristles, must be high enough to keep this error negligibly small.

The input values of this bristle friction model implementation are the same as the previous algorithm. However, the local slip velocity is now computed with the new coordinate system ${}^{\tilde{\mathrm{C}}}[\cdot]$ for the bristles as

$$ {}^{\tilde{\mathrm{C}}}\boldsymbol{v} = {}^{\tilde{\mathrm{C}}}\mathbf{T}_{\mathrm{FW}}\left(\tilde{\theta}_i\right)\left[{}^{\mathrm{FW}}\boldsymbol{v} + {}^{\mathrm{FW}}\boldsymbol{\omega} \times {}^{\mathrm{FW}}\boldsymbol{r}_{\mathrm{f}\tilde{\mathrm{c}}}\left(\tilde{\theta}_i, \xi_j\right)\right]. \tag{4.18} $$

The normal stress is only taken into account if the bristle is within the wheel-soil contact surface. For this reason, the considered bristle is firstly checked if it is currently inside the surface. In other words, the angle $\tilde{\theta}_i$ must be within the interval $[\theta_{\mathrm{exit}}, \theta_{\mathrm{entry}}]$. However, both angles are not running in the same range and therefore, $\tilde{\theta}_i$ is converted to compare it directly with the exit and entry angle. The possible range of angle $\tilde{\theta}_i$ is in the interval of $[\alpha_{\mathrm{B}}, \alpha_{\mathrm{B}} + 2\pi]$ and the wheel rotation angle α_{B} is within $[0, 2\pi[$. From this follows that

$\tilde{\theta}_i$ can be in the interval of $[0, 4\pi[$ and the conversion to $\tilde{\theta}_{i_{\text{conv}}}$ needs to be

$$\tilde{\theta}_{i_{\text{conv}}} = \begin{cases} \tilde{\theta}_i & \text{if } \tilde{\theta}_i \in [0, \pi[\,, \\ \tilde{\theta}_i - 2\pi & \text{if } \tilde{\theta}_i \in [\pi, 3\pi[\,, \\ \tilde{\theta}_i - 4\pi & \text{if } \tilde{\theta}_i \in [3\pi, 4\pi[\,. \end{cases} \tag{4.19}$$

The converted angle $\tilde{\theta}_i$ is used for the normal stress computation with Equation (3.6) and the additional case analysis, if the bristle is within or outside the wheel-soil contact surface and thus, it yields

$${}^{\tilde{\text{C}}}\sigma(\theta_i) = \begin{cases} \tilde{\theta}_{i_{\text{conv}}}^2 c_1 + \tilde{\theta}_{i_{\text{conv}}} c_2 + c_3 & \forall \tilde{\theta}_{i_{\text{conv}}} \in [\theta_{\text{exit}}, \theta_{\text{entry}}]\,, \\ 0 & \forall \tilde{\theta}_{i_{\text{conv}}} \notin [\theta_{\text{exit}}, \theta_{\text{entry}}]\,. \end{cases} \tag{4.20}$$

After the computation of the tangential velocity and the normal stress at each bristle, the maximum bristle deflection can be obtained by using the same equation as (4.7) with $\tilde{\theta}_i$ instead of using θ_i.

For the calculation of the bristle deflection Equation (4.8) is used with $\tilde{\theta}_i$ and an additional condition which checks, if the bristle is inside the surface, as

$${}^{\tilde{\text{C}}}\boldsymbol{s} = \begin{pmatrix} {}^{\tilde{\text{C}}}s_x\left(\tilde{\theta}_i, \xi_j\right) \\ {}^{\tilde{\text{C}}}s_y\left(\tilde{\theta}_i, \xi_j\right) \end{pmatrix} = \begin{cases} {}^{\tilde{\text{C}}}\boldsymbol{s}_0\left(\tilde{\theta}_i, \xi_j\right) + \int_{t_0}^{t} {}^{\tilde{\text{C}}}\boldsymbol{v}_{\text{t}}\left(\tilde{\theta}_i, \xi_j\right) dt, & \text{if } \left|\left|{}^{\tilde{\text{C}}}\boldsymbol{s}\left(\tilde{\theta}_i, \xi_j\right)\right|\right| < {}^{\tilde{\text{C}}}s_{\max}\left(\tilde{\theta}_i, \xi_j\right) \\ {}^{\tilde{\text{C}}}s_{\max} \frac{{}^{\tilde{\text{C}}}\boldsymbol{v}_{\text{t}}\left(\tilde{\theta}_i, \xi_j\right)}{\left|\left|{}^{\tilde{\text{C}}}\boldsymbol{v}_{\text{t}}\left(\tilde{\theta}_i, \xi_j\right)\right|\right|}, & \text{if } \left|\left|{}^{\tilde{\text{C}}}\boldsymbol{s}\left(\tilde{\theta}_i, \xi_j\right)\right|\right| \geq {}^{\tilde{\text{C}}}s_{\max}\left(\tilde{\theta}_i, \xi_j\right) \\ 0 & \text{if } \tilde{\theta}_i \notin [\theta_{\text{exit}}, \theta_{\text{entry}}]\,. \end{cases} \tag{4.21}$$

Note that $\boldsymbol{s}_0$ at t_0 is assumed as zero again. Moreover, the additional condition also ensures that the bristle discharges when it leaves the wheel-soil contact surface. Finally, the computation of the shear stress vector ${}^{\tilde{\text{C}}}\boldsymbol{\tau}$, as well as the discrete load of each bristle ${}^{\tilde{\text{C}}}\boldsymbol{q}_{\text{SC}}\left(\tilde{\theta}_i, \xi_j\right)$ is obtained by using Equation (4.9) and Equation (4.10) with the new control variables $\tilde{\theta}_i$ and ξ_j. The contact surface reaction vectors ${}^{\text{FW}}\boldsymbol{f}_{\text{SC}}$ and ${}^{\text{FW}}\boldsymbol{t}_{\text{SC}}$ are obtained by using Equation (3.20) and Equation (3.21) with the new rotation matrix ${}^{\tilde{\text{C}}}\mathbf{T}_{\text{FW}}\left(\tilde{\theta}_i\right)$ and vector ${}^{\text{FW}}\boldsymbol{r}_{\text{f}\tilde{\text{c}}}\left(\tilde{\theta}_i, \xi_j\right)$. In case of BFEW, the integration of the surface reactions forces and torques is over the entire wheel surface, instead of wheel-soil contact surface. In order

to ensure that there is no contribution of bristles outside the wheel-soil contact, ${}^{\tilde{C}}\boldsymbol{\tau}$ is automatically zero if the bristle is outside the contact surface.

4.5. Model Discussion

This chapter has shown, which modifications need to be done in order to integrate the extended bristle friction model into the existing BCM. An important issue is to find a reasonable fixation and distribution of the bristles for the wheel-soil contact. As a result, two different approaches have been introduced. The BFCS approach with bristles, which are fixed on the contact surface and the BFEW approach with bristles, fixed on the wheel surface.

The bristles of both BCM extensions can be assumed as linear springs from a physical point of view. In other words, the obtained tangential stress model of the wheel-soil contact is now realized by a number of springs. These springs can only be loaded in the tangential plane of the corresponding contact patch. Each spring contributes a small portion to the shear stress or the friction force, respectively, of the wheel-soil contact surface. The spring's load, is limited and this limitation depends on whether the contact is in static or kinetic regime.

5. Model Analysis

In the following chapter, the introduced BCM extensions are analyzed with *Dymola*, in order to investigate suitable values for bristle parameters. For this reason, several tests with a single wheel are simulated. The single wheel visualization in *Dymola* can be seen in 5.1.

In Table 5.2, the values for the independent BCM parameters, as well as the velocity deadband v_d and the kinetic coefficient k_kin are listed and used for all simulation tests. The values of the independent BCM parameters are chosen from previous simulation tests. v_d should be chosen low enough, as the simulation accuracy increases when this parameter is smaller. However, it is possible that the simulation solver misses a switching condition and the algorithm incorrectly remains in the previous regime when v_d is too small [24]. For this reason, the velocity deadband is set $v_\mathrm{d} = 0.01\,\mathrm{m/s}$, because this value distinctly lies under the common occurring wheel velocities.

For these simulation tests, the kinetic coefficient is initially set to $k_\mathrm{kin} = 0.55$, but later it

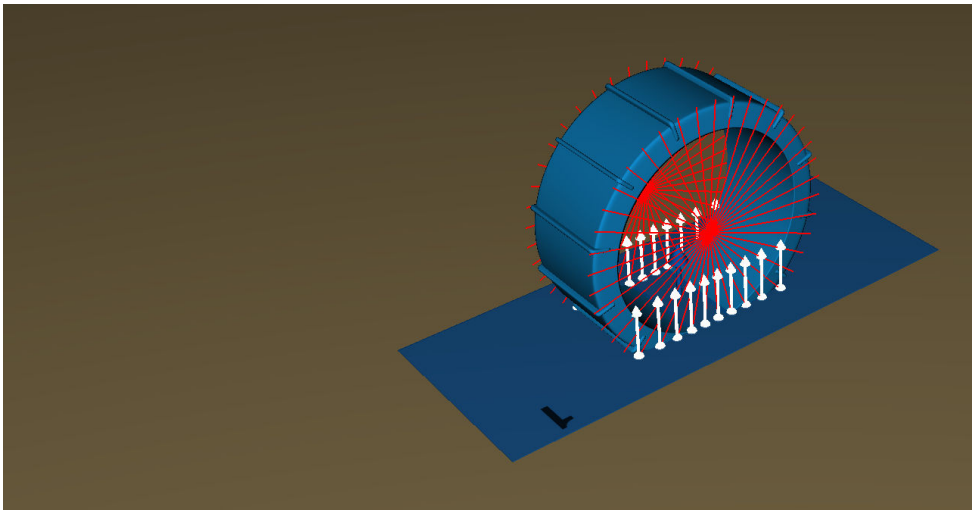

Figure 5.1.: Single wheel simulation in *Dymola*.

needs to be identified in experiments. The wheel radius in this simulation is $r_w = 0.125\,\mathrm{m}$ and the wheel width is $b_w = 0.1\,\mathrm{m}$. Furthermore, RMCS-1 - a quartz sand - is used as soil. In Table 5.1, the BEKKER soil parameters k_c, k_ϕ, n, as well as the cohesion c and the friction angle ϕ for different types of soil can be found.

Table 5.1.: List of soil parameters.
Cohesion c, Friction angle ϕ and BEKKER parameters k_c, k_ϕ, n, from [1] [3].

Soil	c [kPa]	ϕ [°]	k_c $[\mathrm{kN/m^{n+1}}]$	k_ϕ $[\mathrm{kN/m^{n+2}}]$	n [−]
Quartz (RMCS-1)	71.9	30.5	$-1.07 \cdot 10^4$	$1.13 \cdot 10^6$	0.97
MSS-D (RMCS-2)	66.5	36.7	$-2.86 \cdot 10^2$	$2.47 \cdot 10^8$	2.49
Lava (RMCS-3)	101.8	31.0	$-5.62 \cdot 10^3$	$1.85 \cdot 10^7$	1.74
Lime / Feed lime (RMCS-13)[1]	-	38.0	$7.08 \cdot 10^3$	$2.99 \cdot 10^4$	0.829

Moreover, the settings of *Dymola's Rkfix4* solver are also listed in Table 5.2, which are always the same, unless indicated otherwise. Finally, it should be noted that all simulation tests are performed on a standard office PC.

Table 5.2.: BCM parameters and solver settings for simulation.

BCM Parameters and solver settings	Value	Unit
η	0.7	−
V_{CA}	0.01	$\frac{m}{s}$
V_J (Original BCM)	0.01	$\frac{m}{s}$
v_d	0.01	$\frac{m}{s}$
k_{kin}	0.55	−
Fixed Integrator Step	0.001	s
Tolerance	0.0001	−

[1] The cohesion of RMCS-13 was not measurable and for this reason, the cohesion value was set to 1 in the BCM simulation.

5.1. Bristle Coefficients

In the beginning, suitable values for the bristle damping c_b and stiffness k_b need to be found. In [24], it is suggested to increase the stiffness k_b in a stick-slip test, while considering relative velocity between the contact bodies. At a certain point, the differences of the relative velocity at increasing bristle stiffness are hardly changing and further increasing stiffness only influences the computational effort [24].
The stick-slip test, which is mentioned in [24] is not suitable for testing the wheel-soil contact model and a different test scenario has been chosen. The wheel runs a straight trajectory on a soil plane with constant angular velocity which is set to $2\,^{\mathrm{rad}}/_{\mathrm{s}}$ after one second. The radial number of bristles is set to $n = 100$ and the axial number of bristles is $m = 1$ and thus, the total number of bristles is $N_{\mathrm{Bristles}} = 100$. In order to save computational effort, the visual contact detection is deactivated and the x-y plane is used as soil-plane. Furthermore, the bristle damping coefficient is set to $c_\mathrm{b} = 0$ in order to investigate the bristle stiffness separately. The results of different bristle stiffnesses can be seen in Figure 5.2. In the upper plot, the BFCS implementation is illustrated and in the lower Plot, the BFEW implementation. Both implementations show an unrealistic behavior for an insufficient bristle stiffness. While the BFCS reaches the desired velocity with a strong oscillation, the BFEW implementation remains at a lower velocity. Furthermore, in the BFCS, it can be seen that a higher stiffness leads to lower oscillation. However, the oscillation remains at a certain level, despite an increasing bristle stiffness, whereas the period of the oscillation changes with different stiffness and thus, the oscillations are dependent on the bristle stiffness. This remaining oscillation is a result of the mentioned effect, which was discussed in Section 4.3. On the other side, the oscillation in the BFEW implementation disappears almost completely with increasing stiffness. As suitable values, $300000\,^{\mathrm{N}}/_{\mathrm{m}^3}$ to $500000\,^{\mathrm{N}}/_{\mathrm{m}^3}$ seem to provide adequate results.
Figure 5.3 shows the behavior of both implementations with different bristle damping coefficients. The damping leads to a significant reduction of the oscillation in both implementations. However, it is important to remember to choose the damping coefficient low enough, as it does not model a physical behavior, but it is only used as a numerical damping. Suitable values for the damping coefficient c_b are $40000\,^{\mathrm{Ns}}/_{\mathrm{m}^3}$ to $60000\,^{\mathrm{Ns}}/_{\mathrm{m}^3}$,

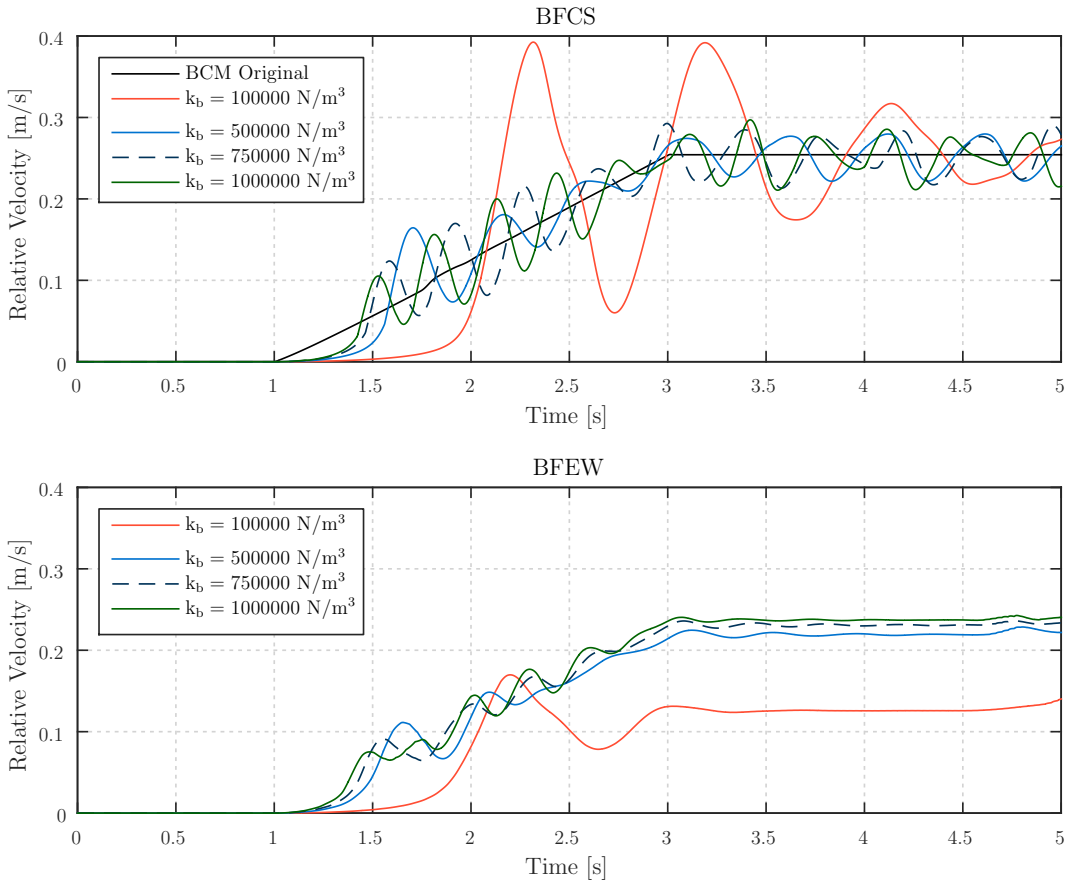

Figure 5.2.: Different bristle stiffness coefficients k_b. Top: BFCS, bottom: BFEW.

because the values in this range suppress the oscillation adequately for both BCM extensions as can be seen in Figure 5.3.

As can be seen in both figures, the oscillation is significantly stronger in the BFCS implementation. This is due to the possible change of the distance from one bristle to the next one during the simulation, which induces the unintentional oscillation as mentioned in Section 4.3. However, the effect can be suppressed with a high damping coefficient, as the upper plot of Figure 5.3 shows.

5.2. Number of Bristles

Another important parameter is the number of bristles N_Bristles, which is the crucial value for the computational effort, as well as the accuracy. On one side, N_Bristles must be high enough so that the error of discretization is as low as possible and on the other side, N_Bristles should be as low as possible in order to keep the computational effort low. The

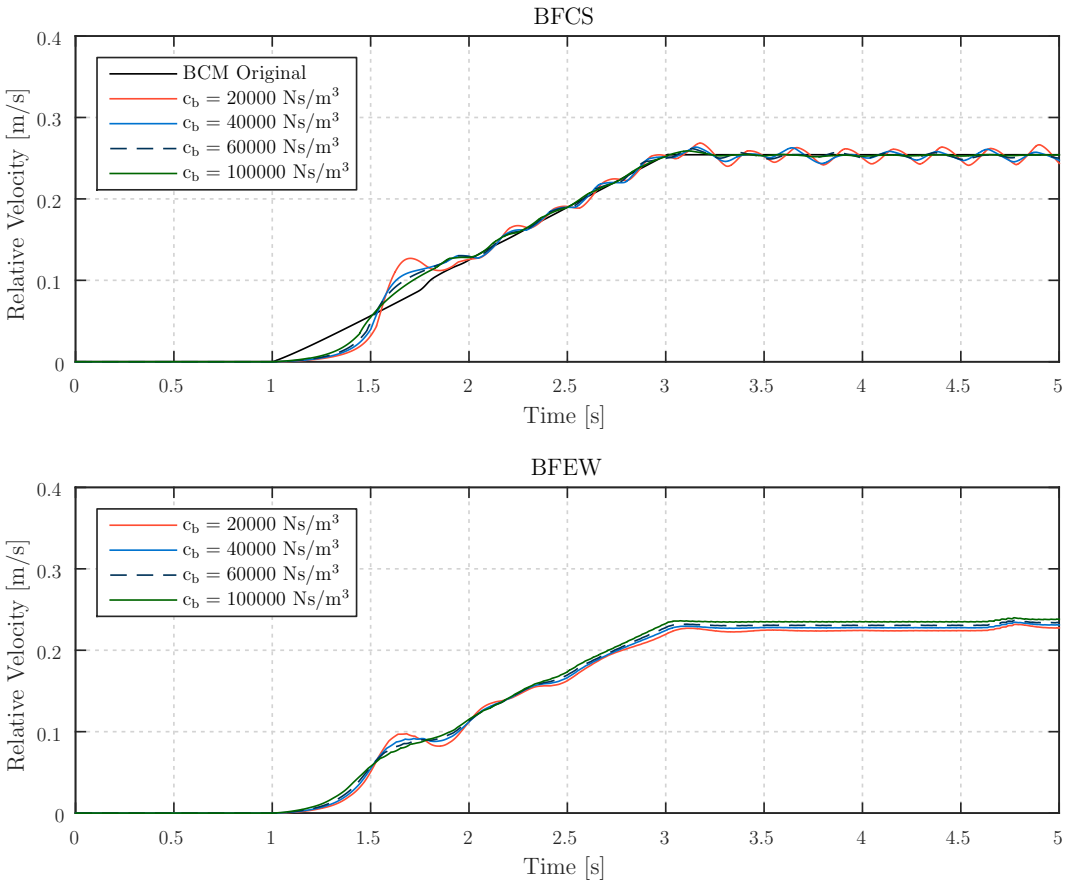

Figure 5.3.: Different bristle damping coefficients c_b. Top: BFCS, bottom: BFEW.

latter is especially important for usage in a real-time environment.

For this reason, the next test is performed in order to investigate the effect of different numbers of bristles. Thus, the same test is run with a different number of bristles and the bristle stiffness and damping parameters are constant and set to $k_\mathrm{b} = 500000\,\mathrm{N/m^3}$ and $c_\mathrm{b} = 40000\,\mathrm{Ns/m^3}$. However, only the radial number of bristles n is changed, while the number of bristles along the wheel width is always $m = 1$, because the latter has no influence on this test scenario. The angular velocity of the wheel is locked to zero during the simulation and thus, each bristle remains at its initial position which simplifies the observation of the bristles. Hence, the wheel is only constantly drawn in longitudinal direction with two different velocities. The wheel is pulled with a translational velocity of $v = 0.005\,\mathrm{m/s}$, within the first 10 seconds. After this time, the translational velocity is immediately changed to $v = 0.015\,\mathrm{m/s}$. This test configuration allows to investigate the transition at the velocity deadband $v_\mathrm{d} = 0.01\,\mathrm{m/s}$ from the static regime to the kinetic

Table 5.3.: Simulation time of different bristle numbers.

Number of Bristle	Computation time in s of BFEW	Computation time in s of BFCS
$n = 11$	17.7	17.5
$n = 31$	29.4	45.2
$n = 51$	40.2	68.6
$n = 101$	67.3	135
$n = 301$	184	390
$n = 1001$	606	1350

regime. In Table 5.3 the computation times of all tests with different radial numbers of bristles n are listed and it shows that the computational effort linearly rises with $\mathcal{O}(n)$ and the computation time of BFCS is two times higher than BFEW.

In case of BFEW, not every bristle is calculated, because only the bristles within the wheel-soil contact surface, which is $n/2$ at the maximum, need to be computed. Due to this fact, it becomes clear that in application, the radial number of bristles in BFEW should be chosen significantly higher than in BFCS to ensure, that there are always enough bristles within the contact-surface.

In order to achieve an equal bristle density within wheel-soil contact surface for both implementations, the radial number of bristles between BFEW and BFCS should have the relation

$$n_{\text{BFEW}} \approx \frac{2\pi}{|\theta_{\text{entry}}| + |\theta_{\text{exit}}|}\, n_{\text{BFCS}}. \tag{5.1}$$

Under the assumption that $n_{\text{BFCS}} = 20$ and the angle of the wheel-soil contact surface is $|\theta_{\text{entry}}| + |\theta_{\text{exit}}| = 60\,^\circ$, it leads to a sixfold radial number of bristles $n_{\text{BFEW}} = 120$ in BFEW, to ensure that at least 20 of these bristles are within the contact surface. However, the angles θ_{entry} and θ_{exit} are time-varying and they are also strongly dependent on the soil. As a result, this example is not universal, but it serves as a rough estimation and it shows that in application, the radial number of bristles should always be set distinctly higher in BFEW than in BFCS.

In Figure 5.4, the normalized shear stress is related to the simulation time (upper plot) and to the bristle deflection of one bristle (lower plot) for BFCS and Figure 5.5 shows the same results for the BFEW implementation. In order to compare the bristle deflections,

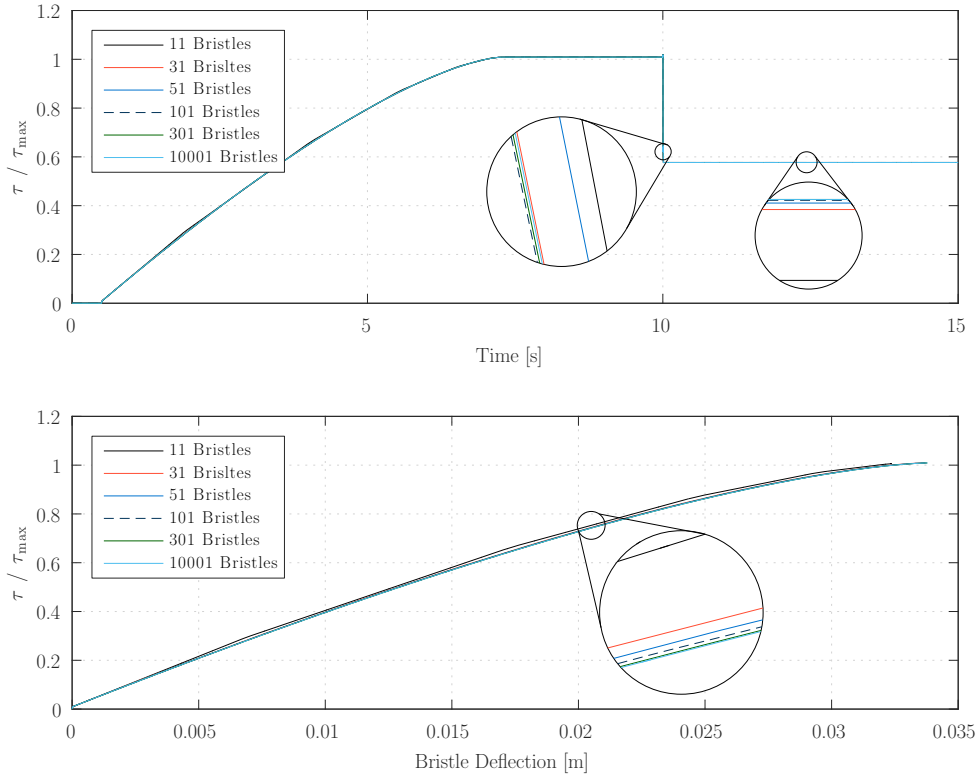

Figure 5.4.: Different radial numbers of bristles n for BFCS.

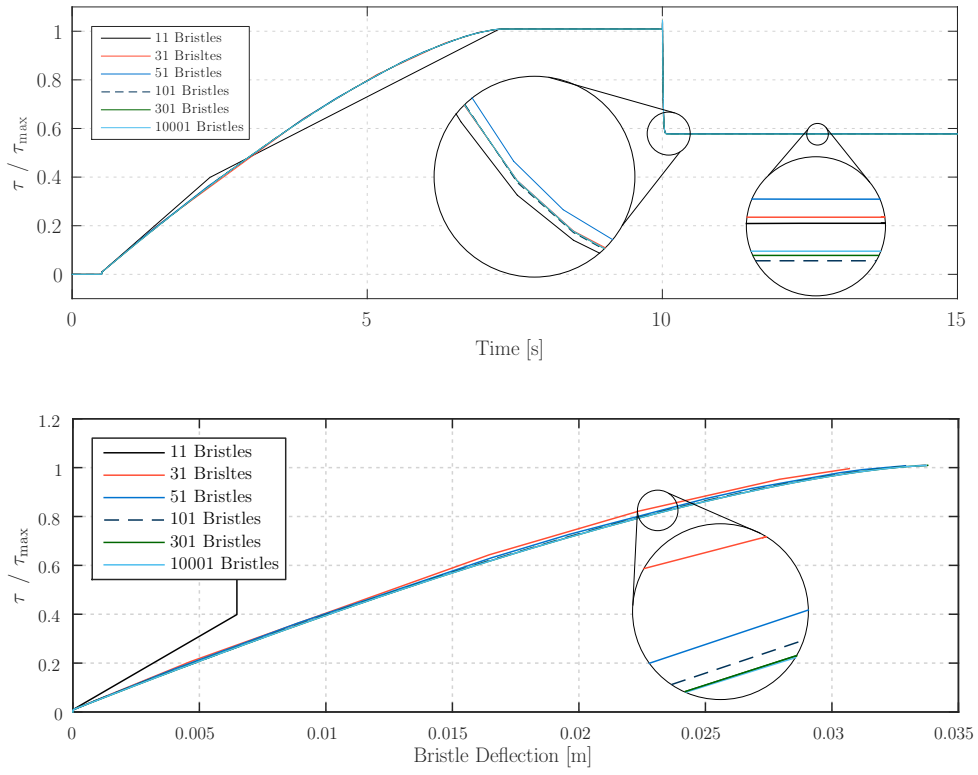

Figure 5.5.: Different radial numbers of bristles n for BFEW.

the bristle with the deepest penetration, respectively the bristle at the lowest point of the wheel surface is always considered for the lower plots of Figure 5.4 and Figure 5.5.
In either case, it can be seen that the shear stress increases until it reaches its maximum after approximately seven seconds. This implies that the strains of the bristles which have soil contact, continuously increase after the wheel started to be drawn. At the point in time, where the shear stress reaches its maximum, every bristle reached maximum deflection $s_{\max} = s_{\mathrm{s}\max}$, because the system is in the static regime. After 10 s, the velocity is set to $v = 0.015\,\mathrm{m/s}$ and thus, the tangential slip velocity of each bristle exceeds the velocity deadband $v_{\mathrm{d}} = 0.01\,\mathrm{m/s}$ and the system changes into the kinetic regime, leading to the lower maximum deflection $s_{\max} = s_{\mathrm{k}\max}$. The change of maximum deflection results in an abrupt decrease of the shear stress at $t = 10\,\mathrm{s}$, and the residual shear stress τ is now dependent on k_{kin}.
With an increasing number of bristles, the error of discretization decreases, as can be seen in Figure 5.6. This figure illustrates the normalized root-mean-squared error of different numbers of bristles related to the simulation with 1001 bristles. The error is less than 1 % for any number of bristles, except the simulation with $n = 11$ and BFEW, in which it is more than 4 % . The error can also be seen in the upper plot of Figure 5.5. At a simulation time of approximately 2 s, an abrupt change of the shear stress increase can be seen. Figure 5.6 also shows that the error of all simulations from 100 bristles are barely changing, which means that simulations with more than 100 bristles have no further benefit. Moreover, the error is distinctly less than 1 %, from $n = 11$ for BFCS and from

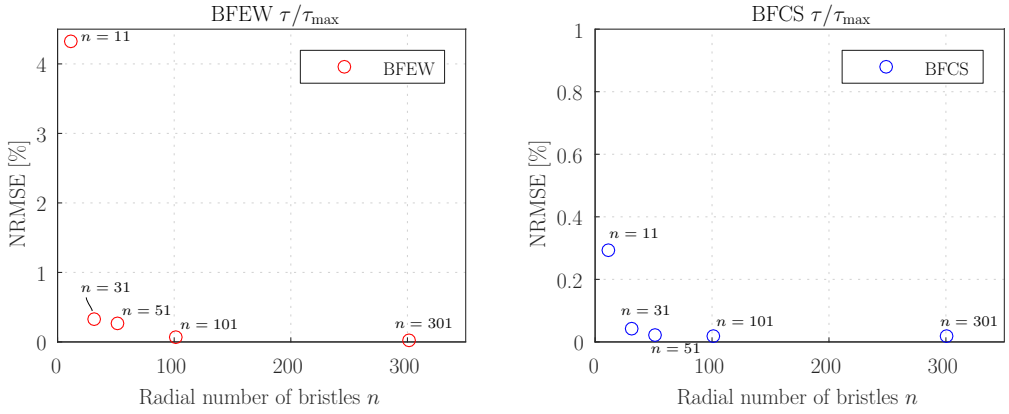

Figure 5.6.: Normalized root-mean-squared error of different numbers of bristles.

$n = 31$ for BFEW. For that reason, a recommended number of bristle is $N_{\text{Bristles}} \approx 20$ for the BFCS approach and $N_{\text{Bristles}} \approx 120$ for BFEW. This large number of bristles for BFEW is supposed to ensure that always enough bristles are within the wheel-soil contact surface.

5.3. Damping Comparison

As mentioned in 3, the original BCM algorithm provides a damping force $\boldsymbol{f}_{\text{D}}$ and a damping torque $\boldsymbol{t}_{\text{D}}$, as well as the bristle friction model extensions provide a damping term, as shown in Equation (2.10). The original BCM applies a damping force and torque to each contact patch directly, whereas in the BFCS and BFEW approach, a damping applies to each bristle. For that reason, both damping approaches are compared in the following section in order to find the most suitable damping approach.

In Figure 5.7 the wheel sinkage of the different damping approaches can be seen for both BCM extensions. In this test scenario the wheel moves straight with an acceleration ramp of $2\,{}^{\text{rad}}/_{\text{s}^2}$ until it reaches an angular velocity of $4\,{}^{\text{rad}}/_{\text{s}}$. In both cases, the bristle damping yields a better result and only with this damping approach it reaches a stationary behavior.

In case of the BFCS implementation, the original damping approach has no effect on the oscillating wheel sinkage, because this oscillation is caused by the changing bristle position within the contact surface and thus, it can only be adequately suppressed by the bristle damping. In contrast, both damping approaches have an effect on the BFEW algorithm, but the oscillation remains at a lower level if the original damping is used. This is a result of the bristles, which enter and leave the wheel-soil contact surface while the wheel turns and this effect induces also a slight oscillation. A damping of this phenomenon can only be done by damping the bristle directly. As a consequence, simulation results of this test scenario show that for both BCM extensions the bristle damping should be preferred.

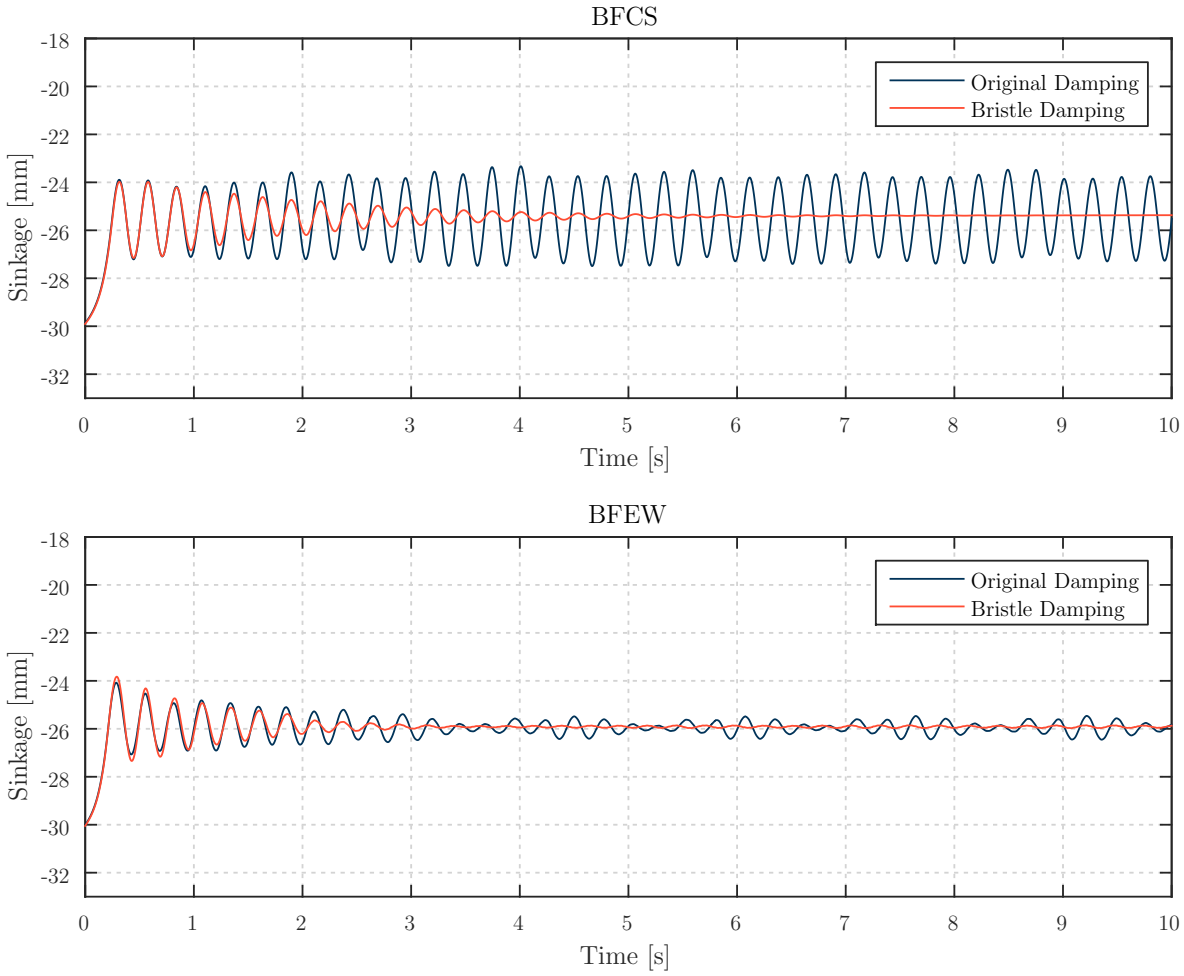

Figure 5.7.: Different damping approaches. Top: BFCS, bottom: BFEW.

5.4. Bristle Behavior Comparison

The different implementation of both BCM extensions have different effects on the behavior of the bristles. Each bristle in the BFCS implementation is always in contact with the surface and thus, each bristle is always exposed to a strain when the wheel is in motion, whereas a bristle of the BFEW approach is only strained when it is within the contact surface.

For this reason, in Figure 5.8 and Figure 5.9 the differences of both implementations are shown, when the driven wheel reaches the stationary state with an angular velocity of $\omega = 3.2\,\mathrm{rad/s}$, which corresponds to $v = 0.4\,\mathrm{m/s}$ by assuming zero slip and the wheel radius r_w. In Figure 5.8, the tangential slip velocity in x-direction ${}^\mathrm{C}v_{\mathrm{t},\,x}$, the maximum deflection ${}^\mathrm{C}s_{\mathrm{max},\,x}$, the bristle deflection ${}^\mathrm{C}s_x$, as well as the velocity deadband v_d of one bristle

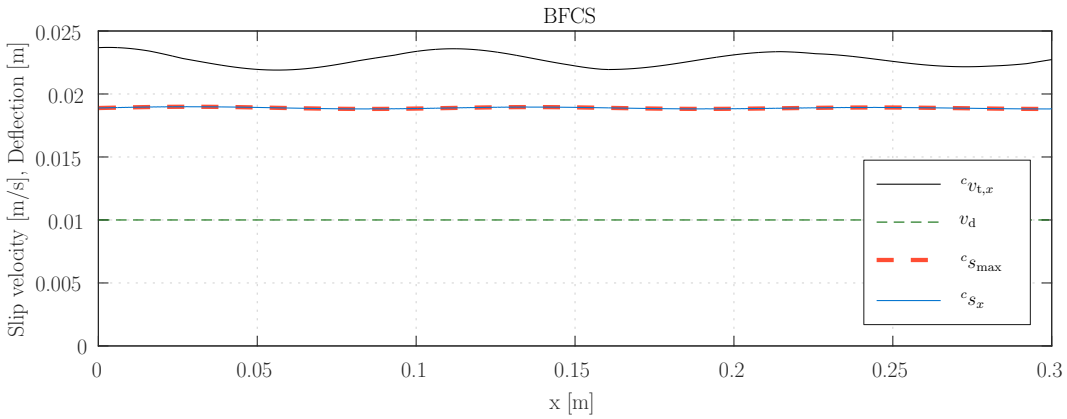

Figure 5.8.: Tangential velocity and bristle deflection of BFCS implementation.

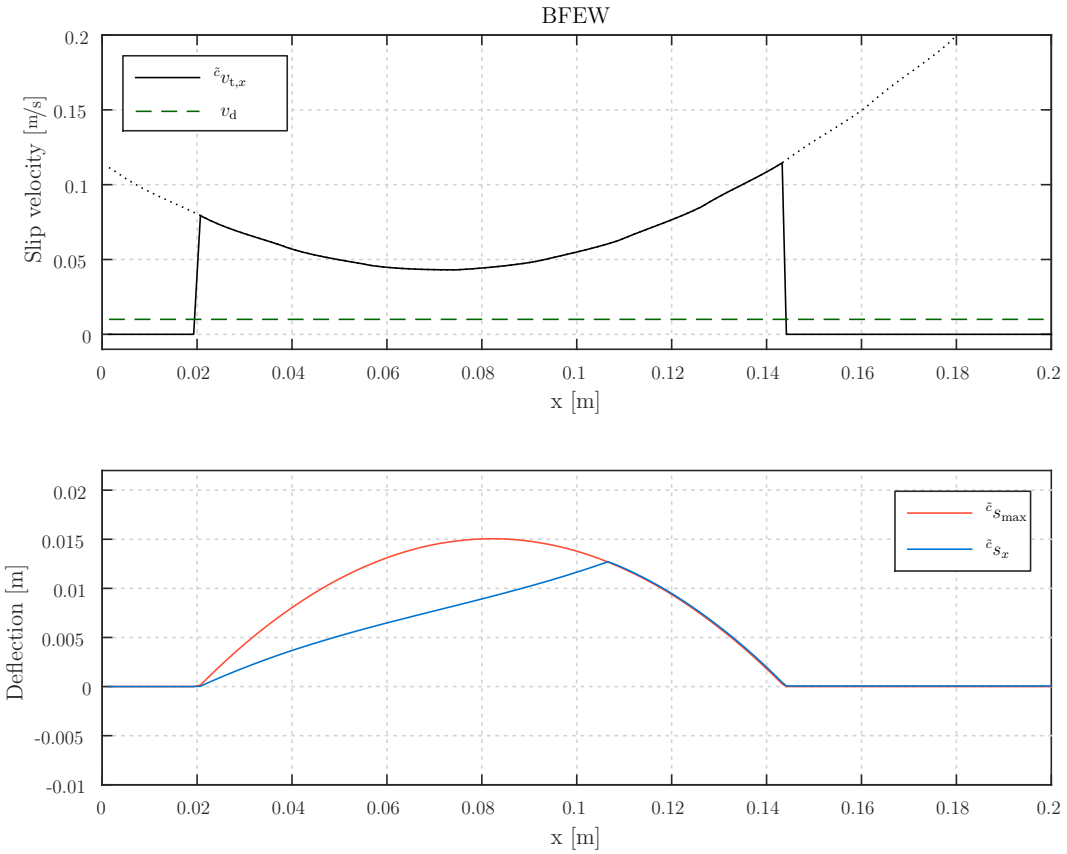

Figure 5.9.: Tangential velocity and bristle deflection of BFEW implementation. Top: tangential velocity, bottom: Maximum deflection and bristle deflection.

in the local contact system are plotted against the x position of the x-y plane, which is used as the soil plane. It can be seen, that the bristle's deflection of the BFCS approach reached its maximum deflection and it remains at the maximum in steady state. The tangential slip velocity has an oscillation, which remains even with damping. An expla-

nation for this oscillation is the already mentioned problem of the changing position of the bristle within the wheel-contact surface, as described in Section 4.3. As a result, the tangential slip velocity is used from different positions during the test and this leads to its oscillation.

On the contrary, the course of the longitudinal entry of the tangential velocity in the local contact point system ${}^{\tilde{\mathrm{C}}}v_{\mathrm{t},\,x}$ of a bristle in the BFEW approach has a completely different behavior due to its fixed position on the wheel surface, as it can be seen in the upper plot of Figure 5.9. ${}^{\tilde{\mathrm{C}}}v_{\mathrm{t},\,x}$ of one bristle has a sinusoidal course as the black dotted line indicates, however the BFEW implementation sets ${}^{\tilde{\mathrm{C}}}v_{\mathrm{t},\,x}$ to zero when the bristle is outside the contact surface and thus, the effective course is represented by the full black line. In the lower plot of Figure 5.9, the corresponding maximum deflection ${}^{\tilde{\mathrm{C}}}s_{\mathrm{max},\,x}$ and the current deflection ${}^{\tilde{\mathrm{C}}}s_x$ of the bristle against the position x are plotted and it can be seen that both courses follow the switching condition of ${}^{\tilde{\mathrm{C}}}v_{\mathrm{t},\,x}$ from zero to non-zero value, when the bristle enters the contact surface. Furthermore, the maximum bristle deflection of the corresponding bristle follows a quadratic course, while the bristle runs through the entire contact surface, which is caused by the quadratic normal stress distribution of Equation (4.20). The current bristle deflection of the corresponding bristle is increasing continuously, while the bristle runs through the contact surface, until it reaches the limit given by the maximum deflection at $x \approx 0.11\,\mathrm{m}$. Now the increase of the deflection is stopped and it follows the limitation of ${}^{\tilde{\mathrm{C}}}s_{\mathrm{max},\,x}$ until the bristle leaves the contact surface again.

Finally, these simulation results showed that the bristle friction model can be successfully integrated in the existing BCM model. In a next step, the model must be validated and for this reason, a test campaign on the SWT was performed which is described in the following chapter. After this, a final evaluation of BFCS and BFEW can be found in 7.5.

6. Experiment on the Single-Wheel Testbed (SWT)

In this chapter, the performed wheel experiments which are supposed to validate the model extensions are discussed. As already mentioned, the SWT as it can be seen in Figure 6.1, is used in order to identify the wheel reactions, as well as the model parameters [30]. For the tests, a loose lime, called "RMCS-13" is used as soil. It's BEKKER soil parameters can be found in Table 5.1.

6.1. Hardware

A schematic diagram of the current testbed at the RMC can be seen in Figure 6.2. The testbed is composed of a soil bin and a rail above the bin. A rover wheel is attached

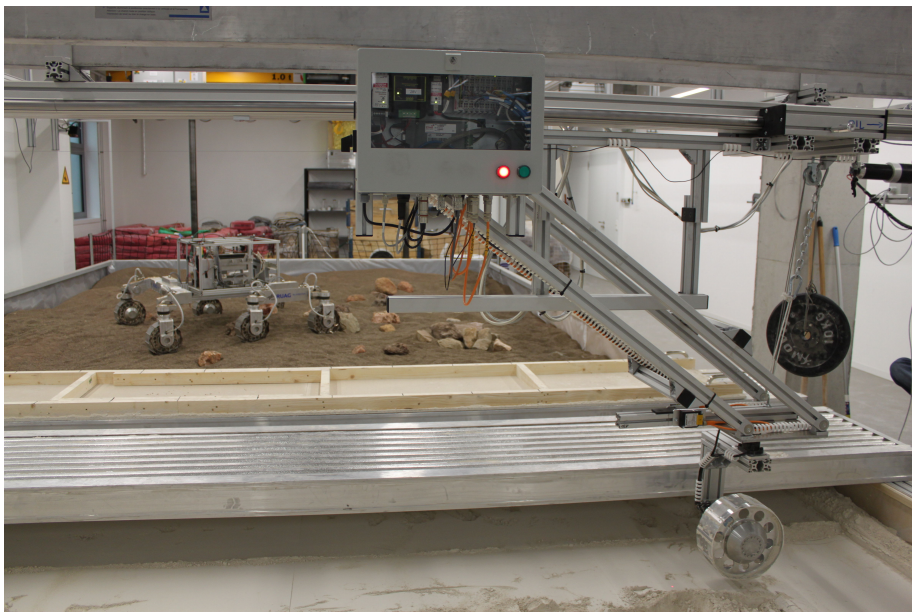

Figure 6.1.: Single-Wheel Testbed at the RMC.

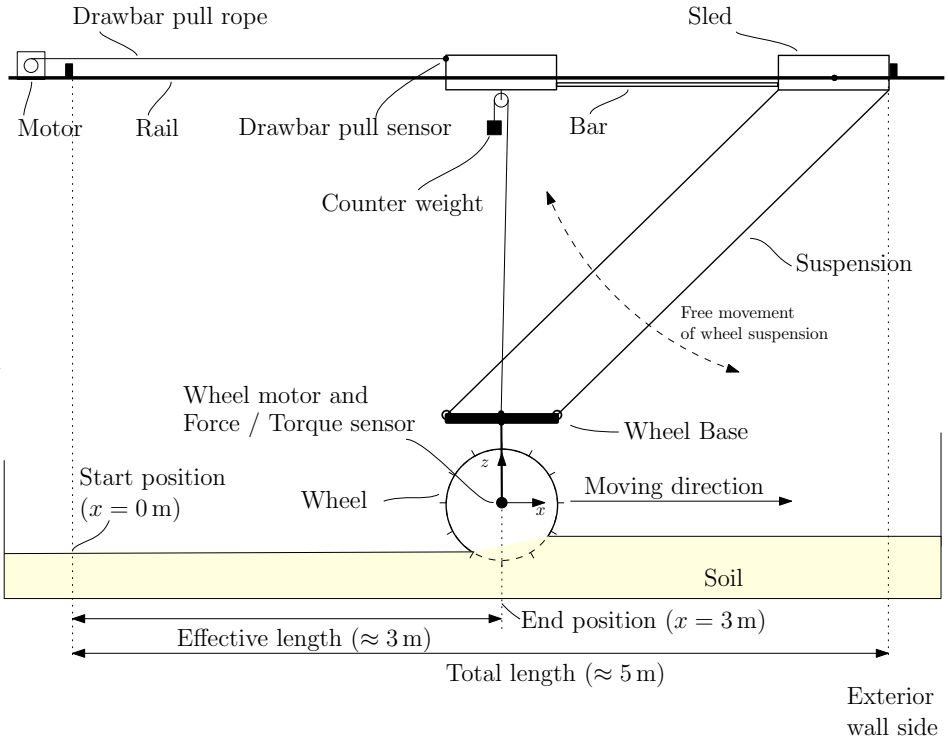

Figure 6.2.: Single-Wheel Testbed (schematic diagram).

to a motor which is connected to the suspension above by a force torque sensor. This suspension is fixed to a sled composed of two linear guides connected via a bar, which moves on the rail. The wheel suspension is a parallelogram kinematic, which has a freedom of movement, as the dashed arrow indicates in Figure 6.2. The configuration of the parallelogram kinematic enables the wheel to move free in z-direction, whereas it prohibits a free lateral movement (y-axis).

The SWT sled contains the control unit of the wheel and the sensors and if no test is performed the wheel can be suspended from this sled. In order to measure the drawbar pull force of the wheel, an additional rope can be used which is fixed on a rope drum on the one side and connected to the sled on the other side. The drawbar pull sensor, which is a load cell, is attached to the sled.

In order to setup a specific normal wheel load, a counterweight is used which is attached via a wire rope hoist to the wheel base, as can be seen in Figure 6.2.

6.2. Modular Wheel

For the experiment modular wheels are used, as illustrated in Figure 6.3. The advantage of this kind of wheel is that the wheel width and the number of grousers, as well as the grouser size can be modified and thus, it is possible to test a lot of different wheel designs and the influence of the grousers can be observed. The wheel used in this tests has a radius of 0.125 m and a width of 0.100 m and the number of grousers is set to 12. The shape of the grousers is rectangular and they have same width as the wheel surface which is 0.100 m.

For the first tests, wheels with different grouser heights, as well as a wheel without grousers, have been used. Later, for the model's validation and parameter identification only two different wheels have been tested, in order to perform all tests in a reasonable amount of time. The chosen wheels have the grouser heights $h_{\mathrm{G}} = 0.0075\,\mathrm{m}$ (Wheel_1) and $h_{\mathrm{G}} = 0.020\,\mathrm{m}$ (Wheel_2).

6.3. SWT Soil

6.3.1. Soil Preparation Methods

At the beginning of each experiment, the soil is loosened and then compressed in order to achieve constant test conditions. For this reason, it is important to determine an explicit

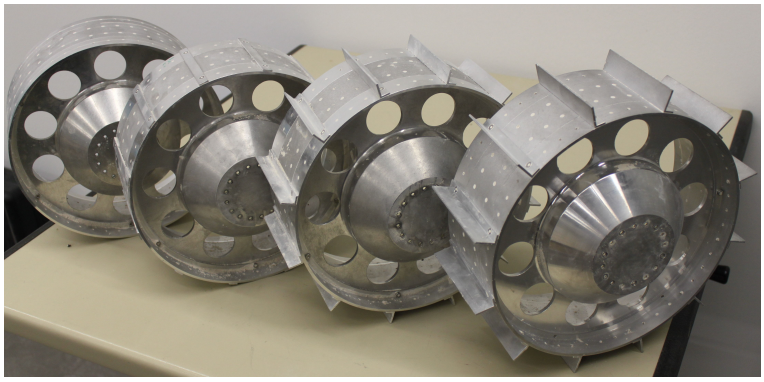

Figure 6.3.: Modular wheels, with different grouser heights.
From left: 1. no grousers; 2. grouser height = 2 mm;
3. grouser height = 15 mm; 4. grouser height = 20 mm

soil preparation method to ensure reproducibility of the experiment [5].

In the existing method, the soil is compressed by applying pressure to the soil with a styrofoam tile. The tile is placed at one end of the soil bin and a person starts to walk on the tile in a certain defined number of small steps. This procedure is repeated step-by-step for the entire soil surface. However, the problem of this compression method was that the styrofoam tile has not covered an entire wheel lane. As a consequence, this increases the probability of inhomogeneous soil compression, as well as an uneven soil surface, even in the same wheel lane. The effect of inhomogeneous compression can be seen on the left of Figure 6.4, which shows the old compression method of the SWT field campaign 2015. The unevenness of the soil surface is distinctly noticeable on the left side and there are also transitions visible, where one styrofoam tile ended and the next started. At this position the probability is particularly high that the soil condition changes, especially if different people stand on each styrofoam tile.

Due to these weaknesses regarding the soil homogeneity, a new soil compression method was elaborated in order to increase the homogeneity of soil. In order to compress the soil, a new tool was built, as it can be seen in Figure 6.5 which make it possible to compress one entire lane of soil in one step. After the soil has been loosened, the soil compression tool is placed on the soil, parallel aligned to the boundaries of the soil bin. Afterwards, two people with comparable weight go on the soil compression tool with a defined number

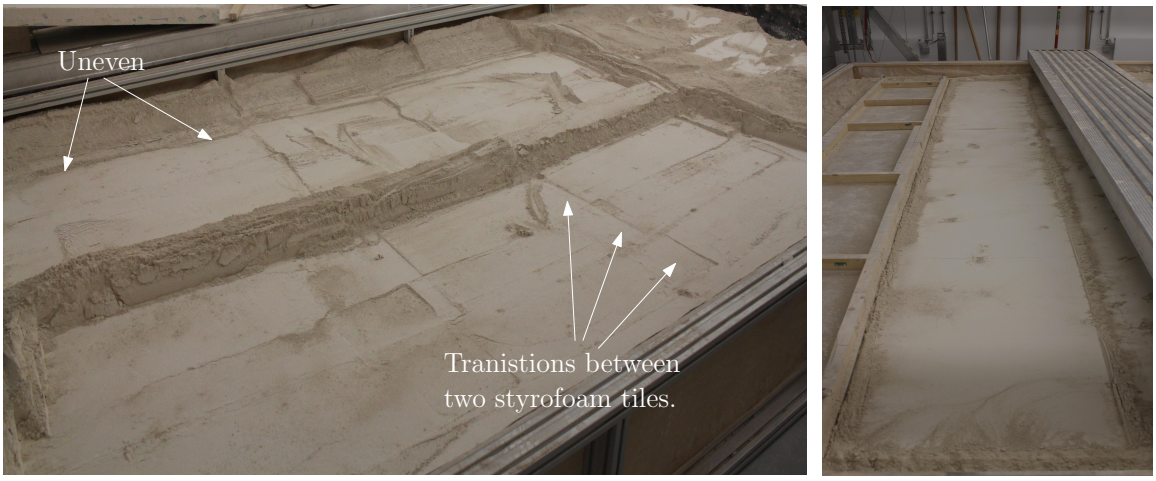

Figure 6.4.: Different soil compression methods. Left: old compression method with styrofoam tiles.
Right: new compression method with soil compression tool.

Figure 6.5.: Soil compression tool (left) and soil compression process (right)

of steps. Simultaneously, the people shift their weight alternatively on either sides. Marks on the tool surface help the people to keep the distance of the defined steps. The result of the new method is illustrated on the right of Figure 6.4 and it can be seen that the soil surface is more even and no transitions are present. The detailed instruction of this new soil preparation method can be found in Appendix A.2 and it should be mentioned that all tests described in this chapter are performed with this new method.

6.3.2. Soil Density

As a part of this work, the density of the soil was measured in different positions within the soil bin after soil compression in order to investigate the homogeneity of the new soil compression method. In order to identify the density, a tool which is illustrated in Appendix B is penetrated in soil in a manner that it is filled with a certain volume of soil. After this, the volume of soil is weighed and the density is determined by calculating the relationship between mass and volume. The mean density of the compressed RMCS-13 soil is $\rho_{\mathrm{RMCS-13,comp}} = 1078\,{}^{\mathrm{kg}}/_{\mathrm{m}^3} \pm 177.8$ and detailed results can be found in Appendix B.

6.4. Limitations of the SWT

In the following, the limits of the SWT are briefly discussed, which should always be considered if a test performed or measurement is interpreted.

6.4.1. Lane Width

In order to prevent all cross-influencing between tests, a minimum lane width between each test must be satisfied. An estimation of the SWT minimum lane width can be determined by considering the soil load distribution [41], [45], as illustrated in Figure 6.6. The equation of the minimum lane width W_{Lane}, which is also used in [3], yields

$$W_{\text{Lane}} = b_{\text{w}} + 2l = b_{\text{w}} \left(1 + \frac{\tan \phi}{\tan \left(45\,^\circ - \phi \right)} \right), \tag{6.1}$$

where b_{w} is the wheel width and ϕ is the friction angle of the soil. The friction angle of the soil RMCS-13, which is used in all experiments, is $38\,^\circ$ and the width of the wheel is $b_{\text{w}} = 0.1\,\text{m}$. From these values, a minimal lane width of $W_{\text{Lane}} = 0.74\,\text{m}$ follows. Due to the soil bin width of 2.8 m, a compromise needs to be found in order to perform tests within a reasonable amount of time. A lane width of $W_{\text{Lane}} = 0.60\,\text{m}$ is used as a compromise to achieve four wheel lanes in the soil bin.

6.4.2. Resistance of the Rail

When a wheel moves in driving direction during a SWT test, it has to overcome not only the motion resistance of soil but also the inertia of the wheel suspension and the resistance of the rail. The latter is induced by the friction between the linear guides and the rail and must be taken into account in the measurement's interpretation.

The resistance was measured by suspending the wheel and pulling the wheel suspension with the drawbar pull rope. This rope is connected to the sled via the load cell, which

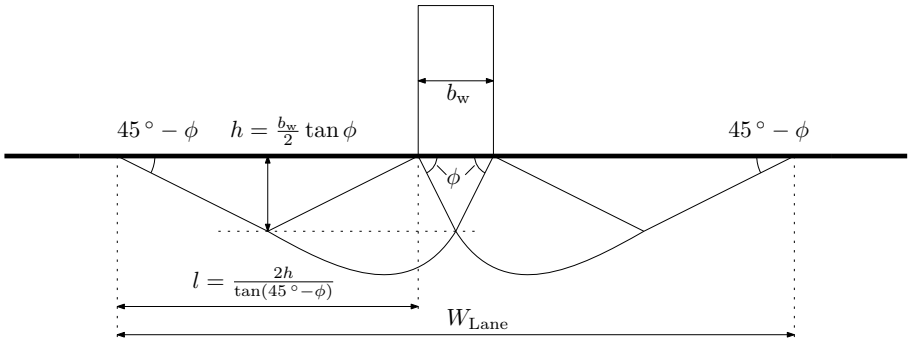

Figure 6.6.: Estimation of the SWT lane width W_{Lane} by considering load distribution of the soil, cf. [45].

measures the pulling force. The measurement results for both directions can be found in Appendix C. It can be seen that the resistance depends on the position of the sled, as well as the relative velocity between rail and sled.

When the wheel suspension is moved backwards, an additional resistance has to be overcome. It is caused by the drawwire sensor, which is used for the position and velocity measurement. In this case, an extra force is needed to extract the sensor wire, from the rope capstan [44].

6.4.3. Wheel Suspension Kinematic

Due to the constrained freedom of movement of the parallelogram kinematic, the wheel suspension either increases or decreases the wheel sinkage, depending on the moving direction. If the resistance between the sled and rail is too high or if the sled is completely fixed to the rail, and simultaneously the soil is not able to absorb the contact reaction forces and torques the soil will fail and the wheel will follow the limited direction of movement of the kinematic. As a result, the wheel digs in the soil and gets stuck, as can be seen in Figure 6.7, and the experiment must be stopped.

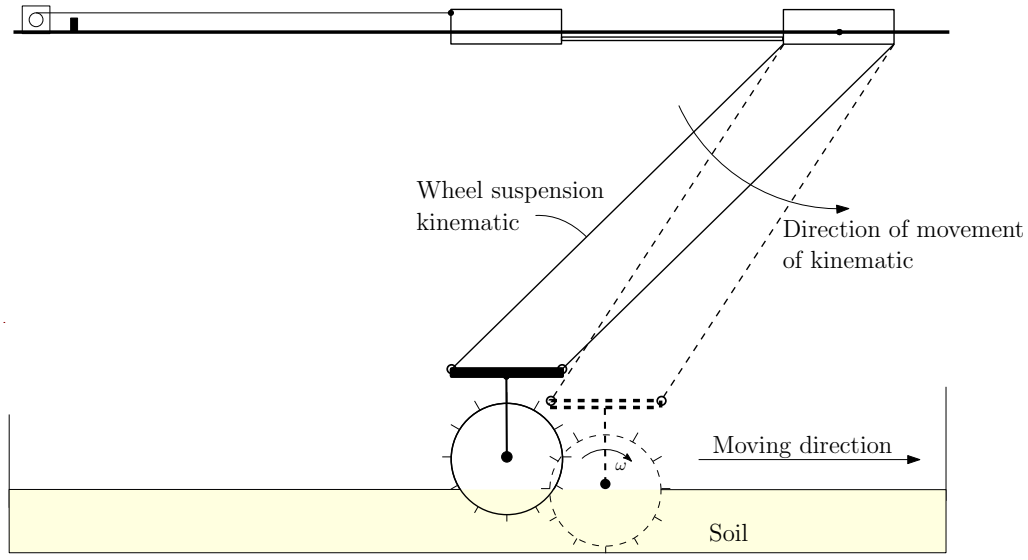

Figure 6.7.: The wheel suspension benefits the wheel sinkage.

6.4.4. Counterweight

Due to the wire rope hoist fixation of the counterweight, an oscillation is induced during an experiment. Particularly at the beginning of experiment, when the translational velocity changes abruptly, the counterweight begins to oscillate because of its inertia. Despite an adequate fastening of the counterweight, it can not be completely avoided that this oscillation is transmitted to the wheel suspension and thus, this effect is also visible in the measurement.

6.5. Test Scenarios

Within this thesis, three different test scenarios were performed in order to identify the parameter of the models and validate the models. For the parameter estimation and the investigation of the shear failure behavior the *Wheel Slip Test* and the *Wheel Pull Test* are performed, whereas the *Free Slip Test* is used for validation.

For the *Wheel Slip Test*, the sled is fixed and as a result the wheel has zero translational velocity v during the experiment whereas the angular velocity ω is set constant and nonzero. As a consequence, the wheel turns on the spot. However, the angular velocity ω needs to set negative, that the wheel would move against the common driving direction, if the sled would not be fixed to the rail. The reason for this is the limitation of the wheel suspension kinematic, which was already mentioned in 6.4.3. If the wheel would turn with positive angular velocity ω, it would immediately get stuck in soil, because in this direction the wheel suspension benefits a wheel sinkage, as it can only move down as indicated in Figure 6.7. Due to this, the wheel would rapidly sink and the experiment would need to be stopped after a few seconds because the motor needs to be shut down by the reached current limit. As a consequence, the *Wheel Slip Test* is performed with negative angular velocities. In this direction the kinematic of the suspension does not benefit the wheel sinkage.

In case of the *Wheel Pull Test*, the wheel is blocked, which means that the angular velocity ω is zero during the experiment and the wheel suspension is pulled with the drawbar pull rope. As a result, the wheel slides over the soil surface along the entire testbed length. Note, that for this test, the rope is diverted with a guided roll in order to pull the

wheel suspension in the common movement direction as shown in Figure 6.2. In both test scenarios, reaction forces and torques of the wheel-soil contact are investigated and the parameter k_{kin}, which depends on the soil and the grouser height, is identified. Table 6.1 and Table 6.2 show all test configurations of the *Wheel Slip Test* and the *Wheel Pull Test*.

Note that each test configuration is repeated at least three times and each *Wheel Pull Test* is performed with multi-pass iterations.

In case of the *Free Slip Test* the angular velocity is set to constant values and the translational velocity is time-varying and depends on the slip i. The slip i is defined as

$$i = 1 - \frac{v}{\omega r_{\mathrm{w}}}, \tag{6.2}$$

where v is the longitudinal translational velocity of the wheel, ω the angular velocity of the wheel and the wheel radius r_{w}. During the *Free Slip Test*, the wheel suspension is able to move freely. The wheel moves along the entire testbed length and overcomes the resistance of the soil and the resistance induced by the friction of the wheel suspension rail contact. The measurements of the reaction forces and torques are used in order to investigate the validity of the model extensions. The test configuration of the *Free Slip Test* are finally listed in Table 6.3. Also, each *Free Slip Test* configuration is repeated at

Table 6.1.: Settings of the *Wheel Slip Test*.

Test configuration ID	1	2	3	4
Wheel	Wheel_1	Wheel_1	Wheel_2	Wheel_2
Translational velocity v_{DBP}	$0\,\mathrm{m/s}$	$0\,\mathrm{m/s}$	$0\,\mathrm{m/s}$	$0\,\mathrm{m/s}$
Angular velocity ω	$-0.8\,\mathrm{rad/s}$	$-1.6\,\mathrm{rad/s}$	$-0.8\,\mathrm{rad/s}$	$-1.6\,\mathrm{rad/s}$

Table 6.2.: Settings of the *Wheel Pull Test*.

Test configuration ID	5	6	7	8
Wheel	Wheel_1	Wheel_1	Wheel_2	Wheel_2
Drawbar pull velocity v	$0.05\,\mathrm{m/s}$	$0.1\,\mathrm{m/s}$	$0.05\,\mathrm{m/s}$	$0.1\,\mathrm{m/s}$
Angular velocity ω	$0\,\mathrm{rad/s}$	$0\,\mathrm{rad/s}$	$0\,\mathrm{rad/s}$	$0\,\mathrm{rad/s}$
Iterations (multi-pass)	2	2	2	2

Table 6.3.: Settings of the *Free Slip Test*.

Test configuration ID	9	10	11	12
Wheel	Wheel_1	Wheel_1	Wheel_2	Wheel_2
Desired translational velocity v_{Des} (Zero slip assumed)	$0.1\,^{\text{m}}/_{\text{s}}$	$0.2\,^{\text{m}}/_{\text{s}}$	$0.1\,^{\text{m}}/_{\text{s}}$	$0.2\,^{\text{m}}/_{\text{s}}$
Angular velocity ω	$0.8\,^{\text{rad}}/_{\text{s}}$	$1.6\,^{\text{rad}}/_{\text{s}}$	$0.8\,^{\text{rad}}/_{\text{s}}$	$1.6\,^{\text{rad}}/_{\text{s}}$
Iterations (multi-pass)	2	2	2	2

least three times and performed with multi-pass iterations.

6.6. SWT Simulation in Dymola

In order to achieve adequate simulation results, which can be compared to the performed test scenarios of 6.5, the SWT was implemented in *Dymola*. The SWT visualization of the simulation is illustrated in Figure 6.8. For suitable simulation results, it is important to implement the friction between wheel suspension and rail, which depends on the position x in the testbed and the translation velocity. As a consequence, the measurement results of the experiment, described in Section 6.4.2 and shown in Appendix C are curve-fitted and stored in a 2D look-up table in the SWT model. For the curve-fit a polynomial with

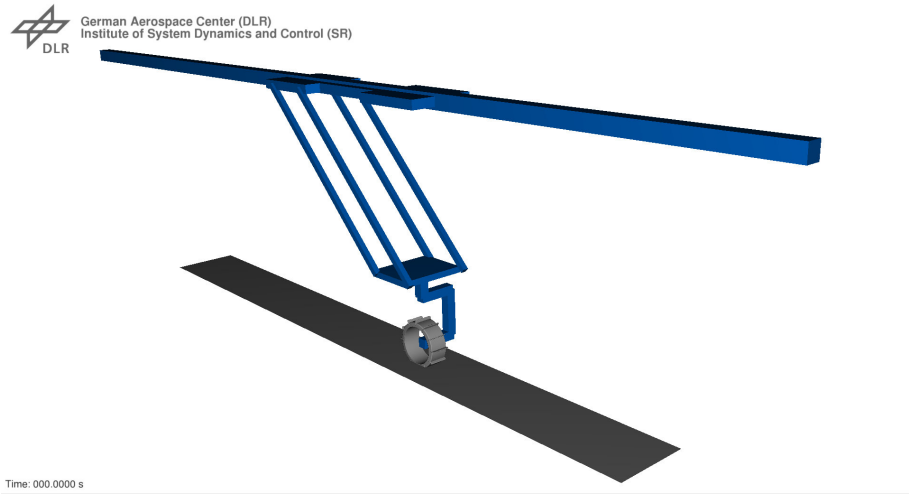

Figure 6.8.: *Dymola* simulation of the SWT.

Table 6.4.: Polynomial coefficients of curve fits.

Polynomial coefficients	k_1	k_0
$v = -0.1\,\mathrm{m/s}$	-3.37	-28.06
$v = -0.5\,\mathrm{m/s}$	-3.40	-26.75
$v = -0.025\,\mathrm{m/s}$	-3.32	-25.90
$v = 0.025\,\mathrm{m/s}$	2.971	0.1674
$v = 0.05\,\mathrm{m/s}$	3.366	0.232
$v = 0.1\,\mathrm{m/s}$	4.616	0.02926

a degree of one is used, as

$$f_x = k_1 x + k_0, \tag{6.3}$$

where x is the testbed position, as well as k_1 and k_0 are the polynomial coefficients of the fits and depend on the relative velocity between rail and wheel suspension. All values for k_1 and k_0 for all velocities, which are measured and fitted, are listed in Table 6.4. For other velocities, *Dymola* interpolates curves, stored in the 2D look-up table, linearly [8]. The result can be seen in Figure 6.9. In order to perform all test scenarios of 6.5 in

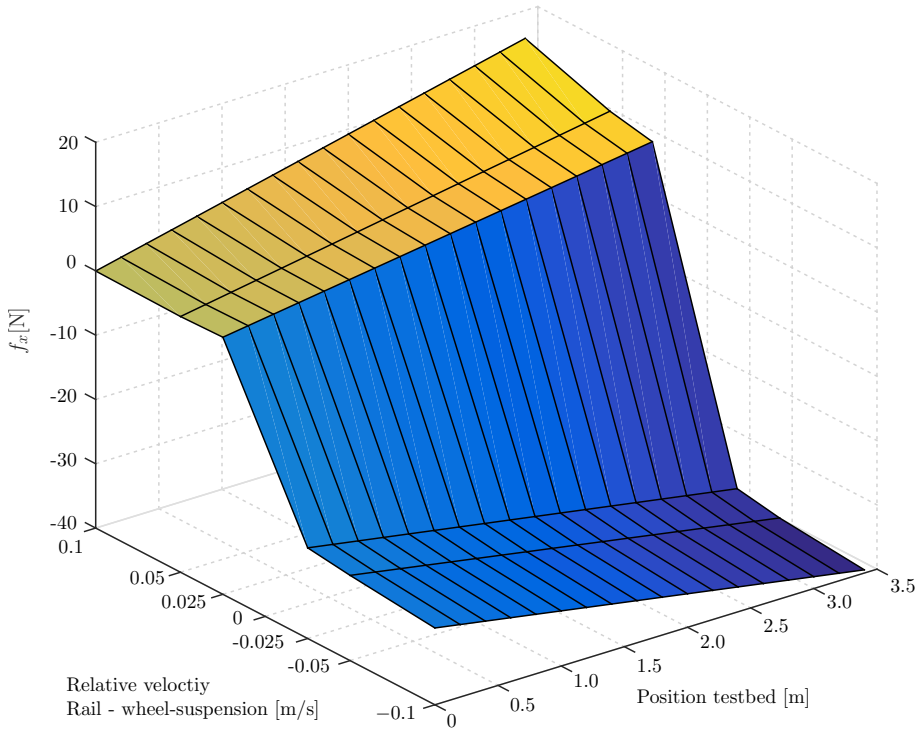

Figure 6.9.: 2D look-up table of the rail wheel suspension resistance.

simulation, the SWT model has been developed with all features of the real SWT. As a result, the same input parameters can be set as in the real system, as well as the same output parameter can be obtained.

7. Results and Validation

In this chapter, the results of the experiments, which are introduced in the previous chapter, are considered and discussed, as well as being compared with *Dymola* simulation in order to identify parameters and to validate the model extensions.[1]

7.1. Wheel Slip Test

In the following, the results of the *Wheel Slip Test* can be seen. Figure 7.1 and Figure 7.2

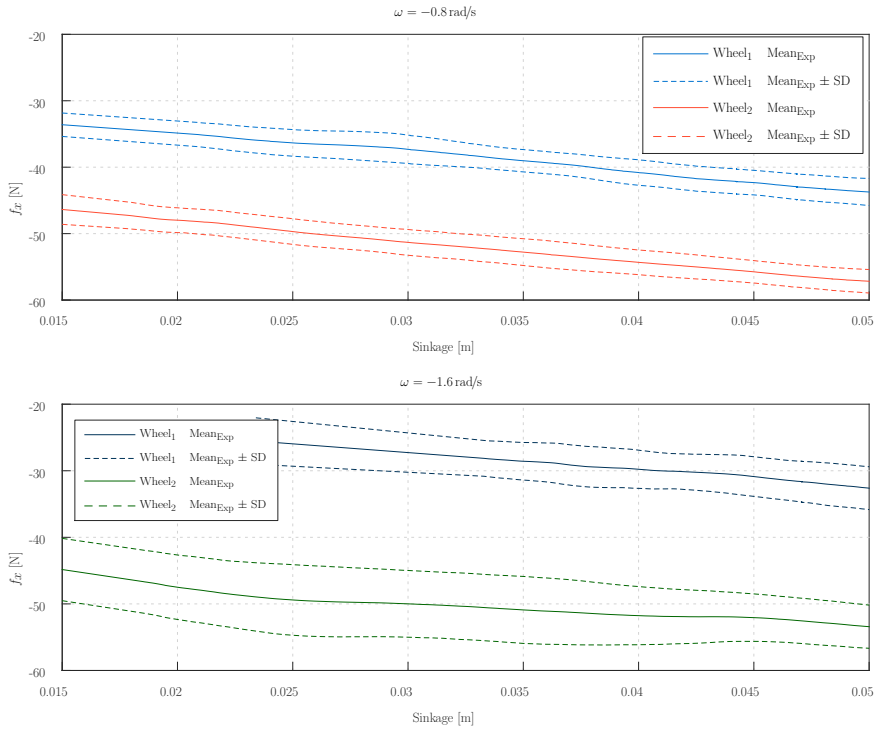

Figure 7.1.: Wheel Slip Test, force x f_x against sinkage.

[1]The following values for the bristle parameters were used:
BFCS: $k_\mathrm{b} = 300000\,\mathrm{N/m^3}$, $c_\mathrm{b} = 40000\,\mathrm{Ns/m^3}$, $v_\mathrm{d} = 0.01\,\mathrm{m/s}$, $10 \times 3\,(n \times m)$ bristles
BFEW: $k_\mathrm{b} = 500000\,\mathrm{N/m^3}$, $c_\mathrm{b} = 40000\,\mathrm{Ns/m^3}$, $v_\mathrm{d} = 0.01\,\mathrm{m/s}$, $40 \times 3\,(n \times m)$ bristles

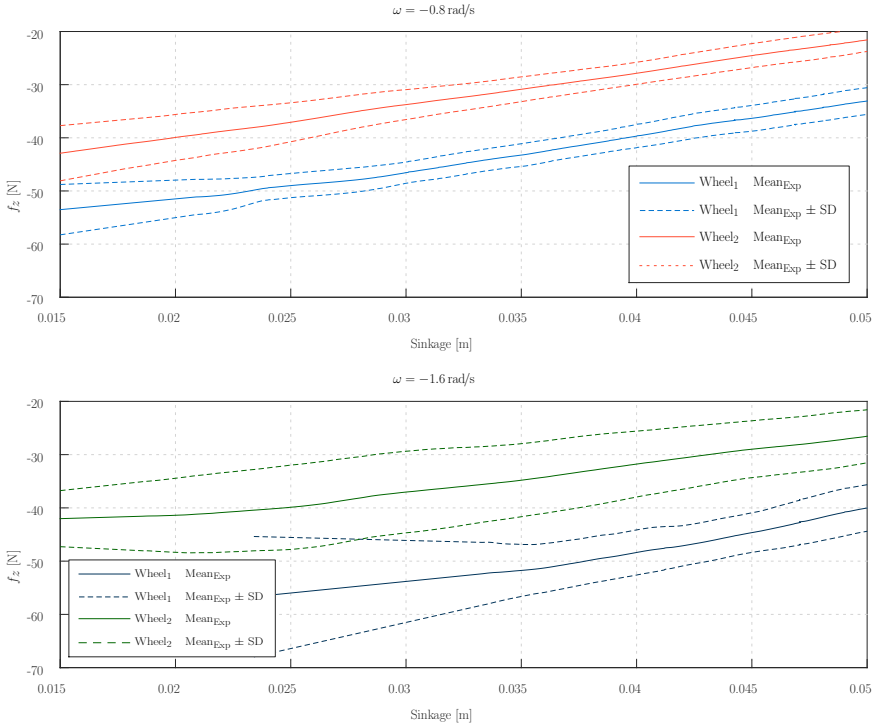

Figure 7.2.: Wheel Slip Test, force z f_z against sinkage.

show the tractive force f_x and the normal force f_z of Wheel$_1$ and Wheel$_2$. Both wheels show an increase of the tractive force with an increasing soil penetration, which is due to the larger wheel-soil contact surface. Furthermore, the influence of the grouser can be seen, as Wheel$_2$ permanently has a higher tractive force of approximately 10 N than Wheel$_1$.

However, the course of the normal force shows an unusual behavior in all *Wheel Slip Tests*, because the normal force decreases with an increasing sinkage, as Figure 7.2 shows. The expected normal force behavior would be a nearly constant value for the whole test, because the vertical wheel load is not changing during the test.

For this reason, one *Wheel Slip Test* is considered in detail to identify the reason for this behavior.[2] Figure 7.3 shows several moments of the experiment video record. On the left of Figure 7.3, the first second is shown and it can be seen, that the shear failure of the soil sets in. By the fourth second, the wheel has dug off a layer of soil and this soil remains in the areas between the grousers. As the movie shows, the wheel sinks rapidly during this time, because it digs up more and more soil. This effect stops after the wheel has

[2]Experiment test campaign ID 55: Wheel$_1$, $\omega = -0.8\,\mathrm{rad/s}$, $v = 0\,\mathrm{m/s}$

Figure 7.3.: Moments from experiment ID 55 video record. From left to right: 1 s, 4 s, 7 s and 10 s

done one full rotation, which is approximately after 7 s. After this time, the areas of the wheel which are completely laden with sand reach back down to the wheel-soil contact surface and thus, the grousers no longer have any effect. The wheel sinking also stops completely at the same point in time as can be seen in the experiment video record. The effect without sinking is observable until the tenth second, after that, the wheel sinks again for a short time until the force torque sensor reaches the soil and the experiment is stopped. The second sinking is because the sand on the wheel's surface between the grousers begins to fall down from the wheel surface and the grousers can dig the soil of the contact surface again. The wheel sinkage has been observed in the corresponding video record of ID 55 and a similar effect can also be seen in the wheel sinkage measurement, as shown in Figure 7.4. For a better overview, the time points of the images in Figure 7.3 are marked as black dashed lines in the wheel sinkage Figure 7.4. In Figure 7.5, the tractive and normal force (top plot) of experiment ID 55 are illustrated with the same dashed lines to identify the time moments of Figure 7.3. The course of the normal force shows a tremendous decrease, within the respective time interval (0 s to 7 s) that a rapidly wheel sinking can be observed. In the moment (8 s) when the wheel stops sinking, the normal force goes back to the initial amount (0 s to 1 s). From the tenth second the normal force decreases again, which is the same moment where also the second wheel sinking sets in. In the lower plot of Figure 7.5, the friction angle of experiment ID 55 is illustrated. The green dashed line shows the measured friction angle of soil RMCS-13, obtained by the method of Apfelbeck [1] and listed in Table 5.1. It can be seen, that the friction angle is only in the beginning of the experiment and between the eighth and tenth second near to the a value of $\phi = 38\,^\circ$. For this reason, it must be assumed that the force measurement

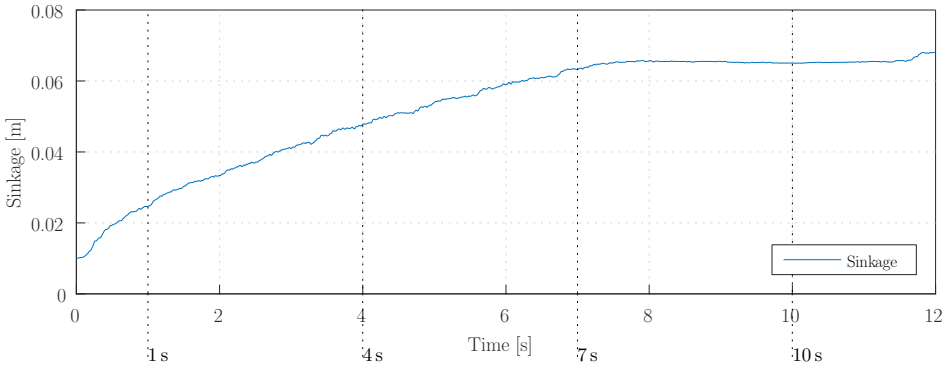

Figure 7.4.: Wheel sinkage against time of ID 55.

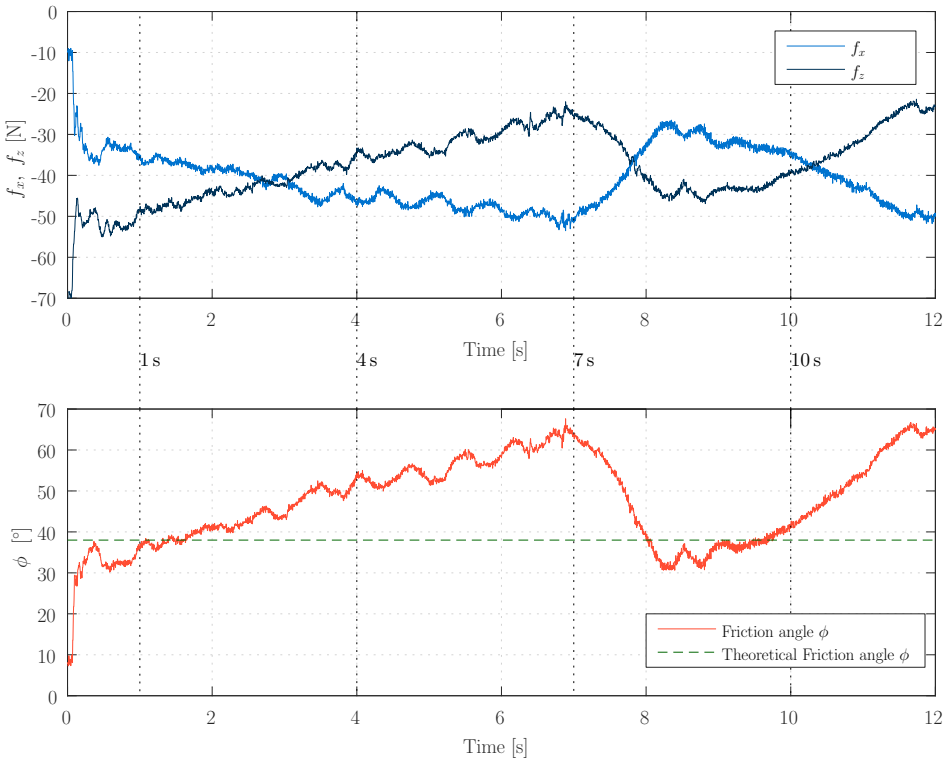

Figure 7.5.: Tractive force, normal force (top plot) and friction angle (bottom plot) against time of ID 55.

is not properly in case of rapid wheel sinking.

A possible explanation of this effect is, that in this test scenario a negative angular velocity for the wheel was used. While the wheel turns, the sinkage increase, because the wheel digs the soil and consequently it moves down. However, the wheel suspension benefits a decrease of sinkage due to its limited freedom of movement and this leads to a force which counteracts the normal load, while the wheel sinks. As a result, the force-torque sensor measures a decrease of the normal force, when the wheel rapidly sinks.

Due to this effect, the *Wheel Slip Test* is unsuitable for an exact parameter identification of k_{kin} and should only be used for a rough parameter estimation. For parameter estimation, only those parts of the experiments that have trustworthy normal force results are used, which are in the beginning of the experiment. In the following, different k_{kin} have been tested in simulation to find the most suitable value. The tractive force f_x of the experiment is compared with BFCS in Figure 7.6 and with BFEW in Figure 7.7. For both figures, in the upper plot the angular velocity $\omega = -0.8\,\text{rad/s}$ is shown and in the lower plot $\omega = -1.6\,\text{rad/s}$ can be seen. The original BCM approach is also shown in both Figures. The results show, that both extensions limit the tractive force by adjusting k_{kin}. The higher k_{kin}, the higher the tractive force f_x. As a result, k_{kin} can be used as limitation for the shear stress of the wheel-soil contact.

The tractive force of the original BCM implementation is distinctly too high in each test. This is because the original BCM has no reduction for the shear stress as do the bristle friction models. The peak of tractive force f_x in the beginning of the original BCM implementation can be explained by the missing modeling of dynamic sinkage, which is caused by wheel slip, as well as the soil digging caused by the grouser [5]. As can be seen in Figure 7.8 and Figure 7.9, which illustrate the wheel sinkage against time, the wheel sinkage of all simulations decreases, whereas the experiments have an increasing wheel sinkage. All BCM implementations only model static sinkage based on the equations of Bekker, and the increasing sinkage caused by motion resistance and slip of the wheel and soil digging by the grousers is not included [27]. The high shear strength in case of the original BCM leads to high tractive force and the wheel suspension kinematic benefits a decrease of sinkage in case of a negative angular velocity. In reality, this effect is not observable because of the dynamic sinkage effect, respectively the displacement of soil caused by the wheel grousers and it will lead to an increasing wheel sinkage despite of the wheel suspension characteristics.

Figure 7.6 shows that the tractive force of BFCS has also a negative peak in the beginning of the experiment, whose size depends on the chosen k_{kin} and angular velocity. Due to the sudden change of the angular velocity in the first 0.2 s an abrupt change of the wheel sinkage is induced, if k_{kin} is small enough. At this point in time, the bristle deflection increases and after a while the bristle's state changes from static regime to kinetic regime

and the bristle deflection decreases abruptly. The effect is stronger if k_{kin} is smaller, because then the difference between static and kinetic regime has more effect and the abrupt change of the sinkage benefits this effect. Therefore, this effect can only observed if k_{kin} is under a certain level and the velocity is low enough.

This effect can also observed in BFEW, as the upper plot of Figure 7.7 shows. In this plot a small peak can be seen in case of BFEW $k_{\text{kin}} = 0.10$ and thus, this effect is significantly weaker than in BFCS. The explanation for this is that the bristles of BFCS remain for a longer time in the static regime as they are fixed to the wheel-soil contact surface and this surface does not change during the simulation, because the wheel turns on the spot in the *Wheel Slip Test*. Furthermore, the changing number of bristles which are within the contact surface can be seen in the BFEW simulations as small discontinuities in the courses of tractive force f_x. In case of $-0.8\,{}^{\text{rad}}/_{\text{s}}$, the distance between two discontinuities is $\approx 0.2\,\text{s}$ and in case of $-1.6\,{}^{\text{rad}}/_{\text{s}}$ it is $\approx 0.1\,\text{s}$. This is roughly the time it takes for the wheel to traverse the distance between two bristles at the corresponding angular velocity. [3]

As parameter estimation of k_{kin}, the tractive performance of simulation is compared with the tractive performance of the experiment. For Wheel_1 a $k_{\text{kin}} = 0.10 - 0.15$ and for Wheel_2 a $k_{\text{kin}} = 0.15 - 0.20$ seems suitable for BFCS and BFEW. These values match the tractive performance of the experiments best.

[3] For BFEW simulation, 40×3 bristle were used. Wheel radius $r_{\text{w}} = 0.125\,\text{m}$

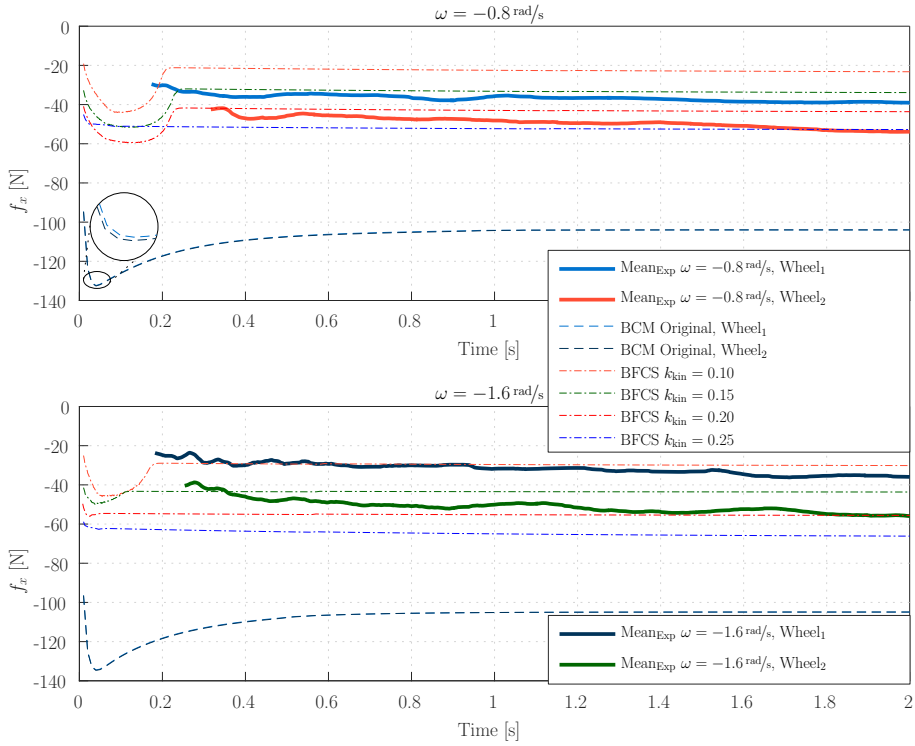

Figure 7.6.: *Wheel Slip Test*, tractive force f_x, BFCS comparison.

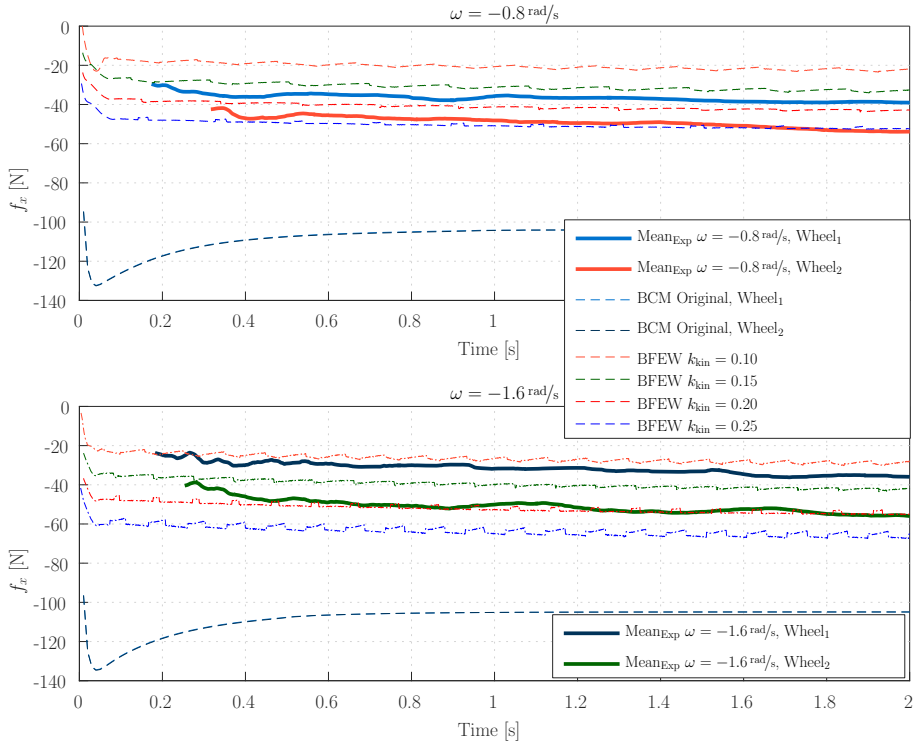

Figure 7.7.: *Wheel Slip Test*, tractive force f_x, BFEW comparison.

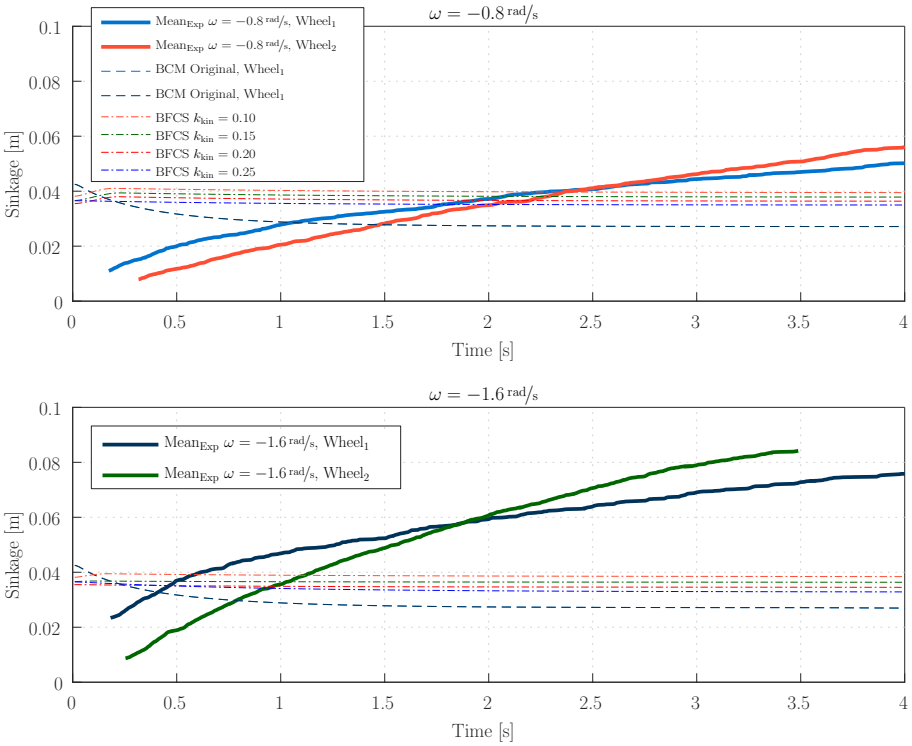

Figure 7.8.: *Wheel Slip Test*, sinkage, BFCS comparison.

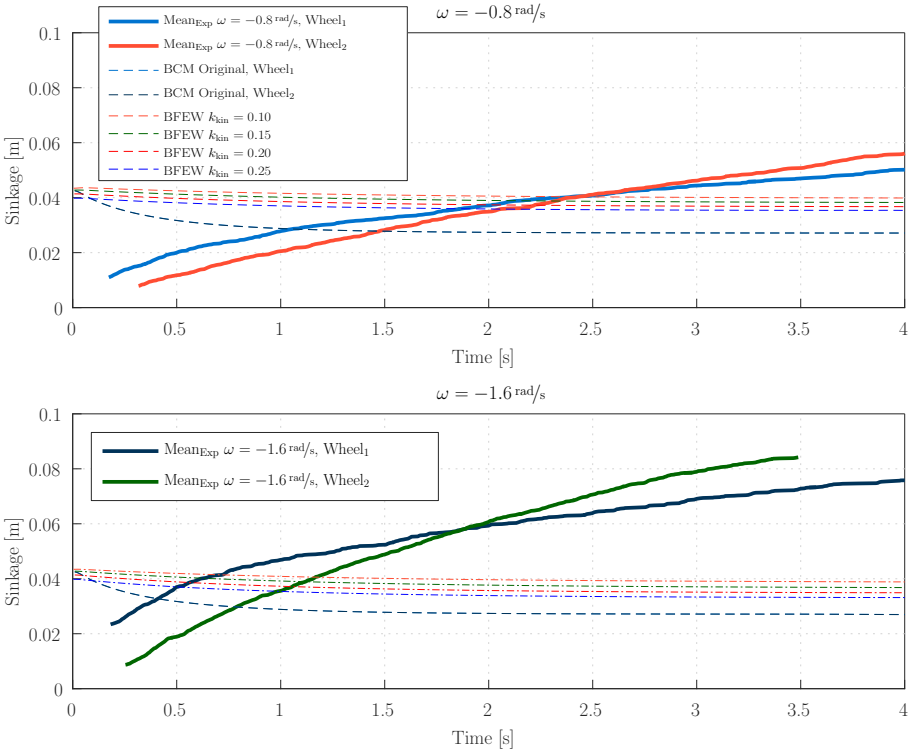

Figure 7.9.: *Wheel Slip Test*, sinkage, BFEW comparison.

7.2. Wheel Pull Test

In Figure 7.11 and Figure 7.12, the experimental results of the *Wheel Pull Test* for Wheel_1 for both velocities $v_{\text{DBP}} = 0.05\,\text{m/s}$ and $v_{\text{DBP}} = 0.1\,\text{m/s}$ are illustrated. The results for Wheel_2 are illustrated in Figure 7.13 and Figure 7.14. In each Figure, the upper plot is is the tractive force f_x, the center plot is the normal force f_z and the lower plot the wheel sinkage against the position in the testbed. It can be seen that both forces vary considerably in each *Wheel Pull Test*.

In order to explain this behavior, Figure 7.10 shows two moments of a *Wheel Pull Test* with ID 79.[4] An amount of soil accumulates in front of the wheel, caused by bulldozing. This means an additional resistance which needs to be overcome while pulling the wheel and this results in a higher force f_x. Moreover, the amount of accumulated soil in front of the wheel is not constant but it alternates between large and small amounts. At the beginning of the experiment, the amount of bulldozed soil in front the wheel increased tremendously, as well as the wheel sinkage. This high bulldozing resistance could be observed, because the wheel was blocked and only pulled. However, after a while the amount of soil was large enough and it acted like a wedge, which pushed the wheel up again, decreased the amount of soil in front of the wheel and the effect started over.

The force plots also show oscillations at several moments, especially for Wheel_2 as Figure 7.14 shows between 1.7 m and 2.2 m. A possible explanation for this effect is inhomogeneous

Figure 7.10.: *Wheel Pull Test*, Wheel_2, $v_{\text{DBP}} = 0.1\text{m/s}$, tractive force f_x, normal force f_z, sinkage. Left: a large amount of soil in front of the wheel. Right: a small amount of soil in front of the wheel.

[4] Experiment test campaign ID 79: Wheel_1, $\omega = 0\,\text{rad/s}$, $v_{\text{DBP}} = 0.1\,\text{m/s}$

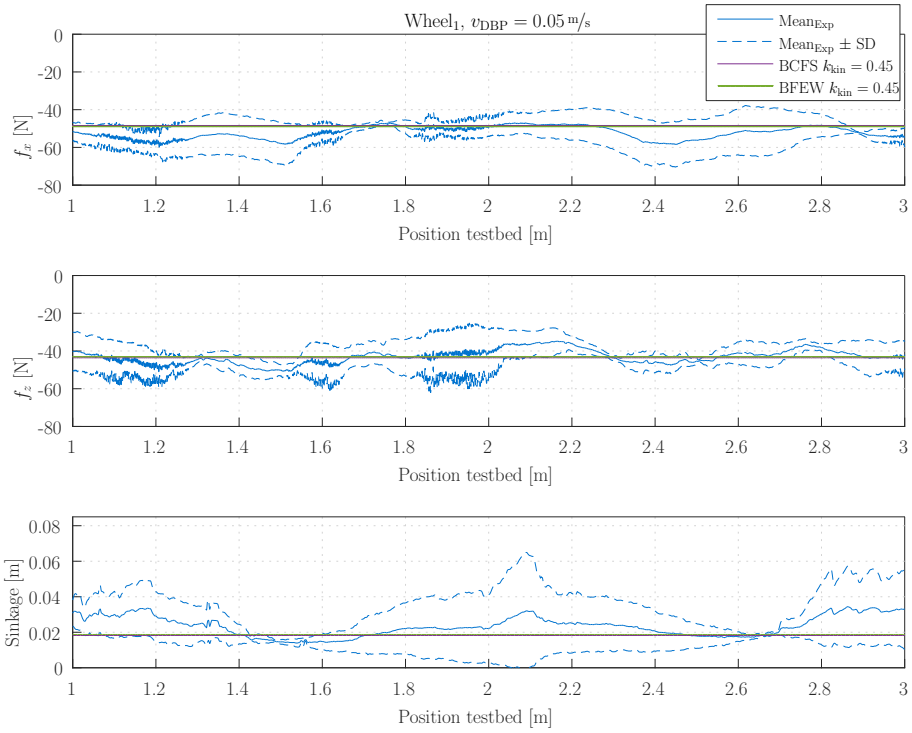

Figure 7.11.: *Wheel Pull Test*, Wheel$_1$, $v_{DBP} = 0.05$m/s, tractive force f_x, normal force f_z, sinkage.

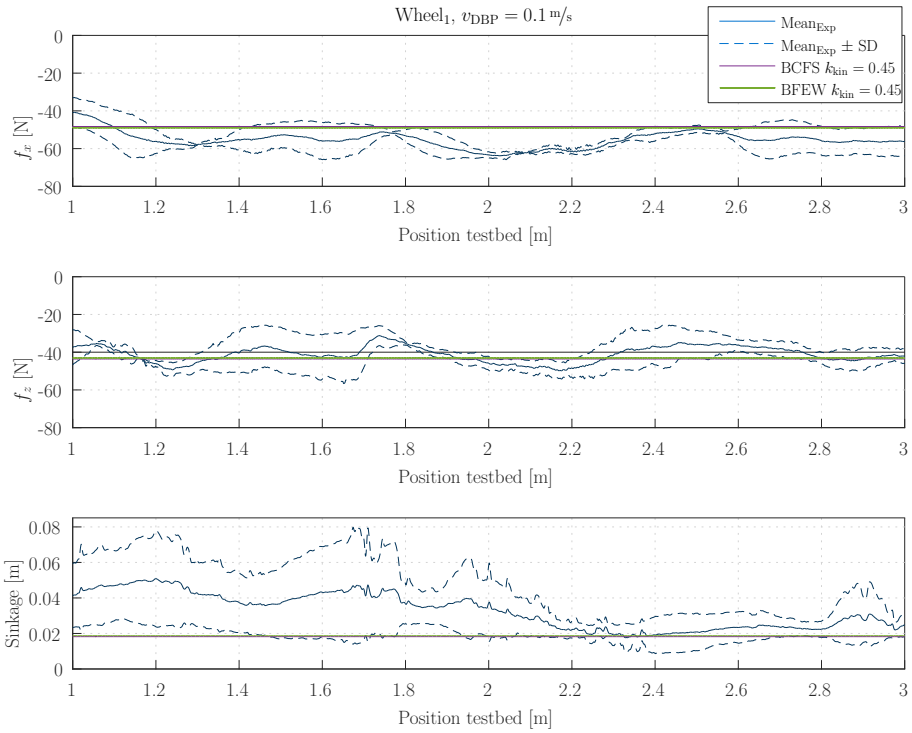

Figure 7.12.: *Wheel Pull Test*, Wheel$_1$, $v_{DBP} = 0.1$m/s, tractive force f_x, normal force f_z, sinkage.

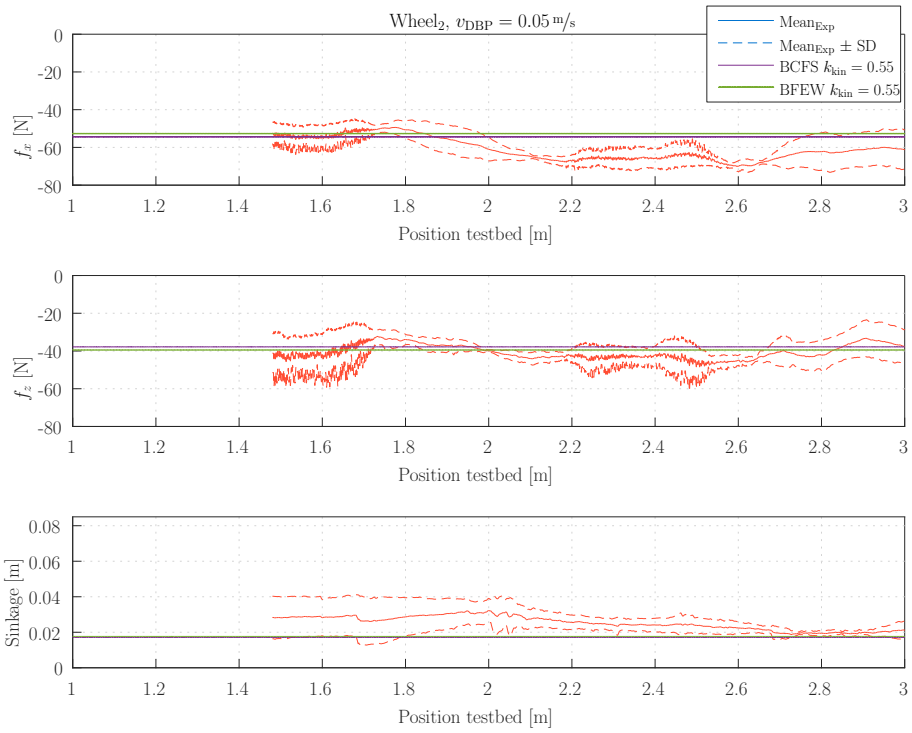

Figure 7.13.: *Wheel Pull Test*, Wheel$_2$, $v_{DBP} = 0.05$m/s, tractive force f_x, normal force f_z, sinkage.

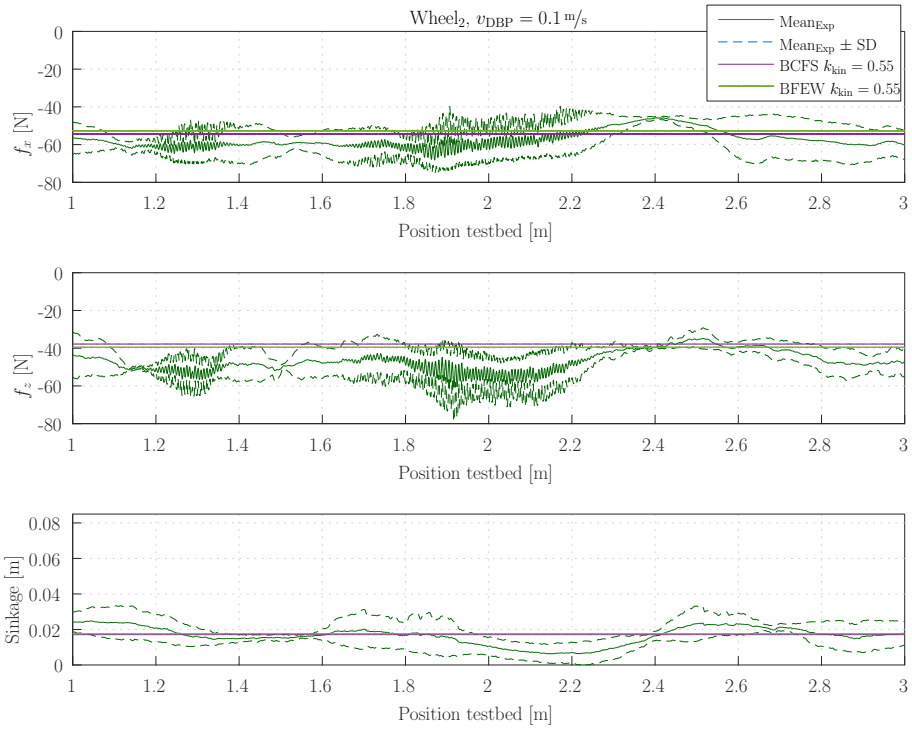

Figure 7.14.: *Wheel Pull Test*, Wheel$_2$, $v_{DBP} = 0.1$m/s, tractive force f_x, normal force f_z, sinkage.

failure of soil and the resistance between SWT rail and the sled. Through flexibility of the kinematic, the wheel suspension can have a spring effect, which leads to an oscillation of the system. The results of the *Wheel Pull Test* show that the bulldoze effect has a significant influence on the experiment's results. However, this effect is neither considered by the original BCM, nor by the BCM extensions. As a result, the *Wheel Pull Test* is unsuitable for a parameter estimation of k_{kin}. In order to demonstrate this, the simulation results for both BCM extensions are shown in Figures 7.11, 7.12, 7.13 and 7.14. As can be seen, compared to the *Wheel Slip Test*, substantially higher values need to be chosen in order to achieve similar results as in the experiments. For Wheel_1 it is $k_{\text{kin}} = 0.45$ and for Wheel_2 it is $k_{\text{kin}} = 0.55$. Moreover, the simulation results show a constant course during the entire test, because the bulldoze effect is not considered.

7.3. Free Slip Test

In the following, the *Free Slip Test* experiment and simulation results are shown in order to investigate the validity of the bristle friction model extensions for BCM and they are also compared to the original BCM. The results of Wheel_1 are shown in Figure 7.15 and Figure 7.16 for desired translational velocity $v_{\text{Des}} = 0.05\,\text{m/s}$ (zero slip assumed). For velocity $v_{\text{Des}} = 0.1\,\text{m/s}$, the experiments for Wheel_1 failed. All tests needed to be stopped after a few seconds, because the wheel got stuck in the soil, caused by a strong dynamic sinkage.

The results show adequate simulation results for f_x, t_y and f_z for the original BCM, as well as the BFCS and BFEW for $k_{\text{kin}} = 0.15$, which is the estimated value from the *Wheel Slip Test*. However, the BFCS implementation shows a strong oscillation within the first 30 cm for low velocities. This oscillation occurs despite an implemented damping of the wheel suspension in simulation. An explanation for this oscillation is the mentioned change of the contact surface size, which induced an unintentional motion of bristles. The oscillation also affects the wheel suspension kinematic and the sled and thus, this oscillation is strongly visible in the plots of the tractive performance f_x and t_y. Another conspicuousness in the experiment results of f_x and t_y plots are the peaks at position $\approx 1.4\,\text{m}$. The explanation for this is that the SWT rail actually consists of two parts. The

transition of these two parts is exactly at this position and it is an additional resistance between sled and rail. However, this effect is not implemented in simulation, because the resistance between sled and rail is approximated as a polynomial with a degree of one. The lack of dynamic sinkage in simulation can also be seen in this test scenario. The upper plot of Figure 7.16 shows, that the wheel sinkage has a significant error in simulation compared to the experiment. The mean of slip i in the experiments is roughly 50%, as visible in the lower plot of Figure 7.16. However, the standard deviation is so high, that the true value can lie almost in the entire range between 0 to 1. As a consequence, the slip measurement results for this test scenario are not trustworthy enough to compare them with simulation results. The slip of the original BCM is almost zero, which means that the prediction of the shear strength is significantly too high. In case of BFCS, the oscillation problem in the beginning can also be seen in the slip plot. For a short time, the slip is negative, which is an unrealistic behavior. An explanation for this is, that the wheel suspension moves slightly back and forth, which is induced by this oscillation. As a result, the wheel suspension pulls the wheel for a short time. At this point, the slip is negative, because the longitudinal translational velocity of the wheel is higher than the product of $\omega\, r_{\mathrm{w}}$.

In Figure 7.17 and Figure 7.18, the mean results of f_x and t_y, as well as wheel sinkage and slip against the desired velocity v_{Des} are illustrated for Wheel_2. Furthermore, the standard deviation (SD) and the standard deviation scalar (SD scalar) are plotted. The latter is an indicator for the quality of the measurement. The lower SD scalar, the better the measurement. The results show an increasing error of the original BCM simulation with increasing velocity. The tractive performance is significantly too high at $v_{\mathrm{Des}} = 0.2\,\mathrm{m/s}$. On the contrary, the tractive performance of both bristle friction models show consistency to the experiment results with suitable values for k_{kin}. The already mentioned lack of dynamic sinkage is also clearly visible. The slip measurement results for Wheel_2 are more trustworthy than for Wheel_1, because the true value lies within a smaller SD range. BFCS and the original BCM have a good consistency to the measurement result. BFEW has good prediction for $v_{\mathrm{Des}} = 0.1\,\mathrm{m/s}$ and whereas for $v_{\mathrm{Des}} = 0.2\,\mathrm{m/s}$ the slip prediction is too high, which is an indication for a too high k_{kin}.

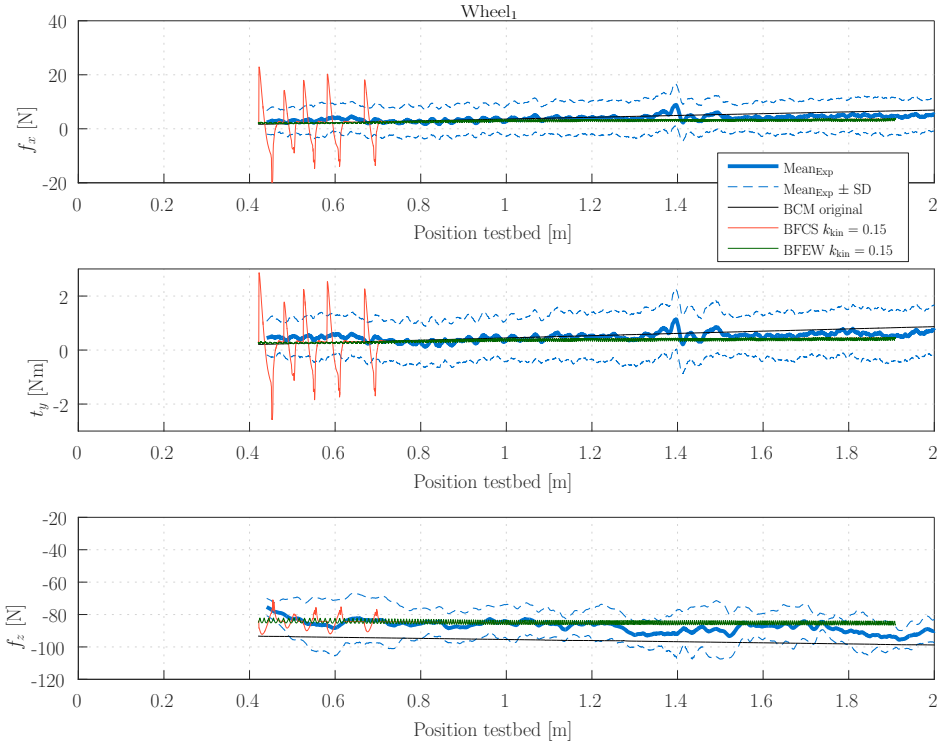

Figure 7.15.: *Free Slip Test*, Wheel$_1$, $v_{Des} = 0.05^{m}/_{s}$, tractive force f_x, torque t_y, normal force f_z.

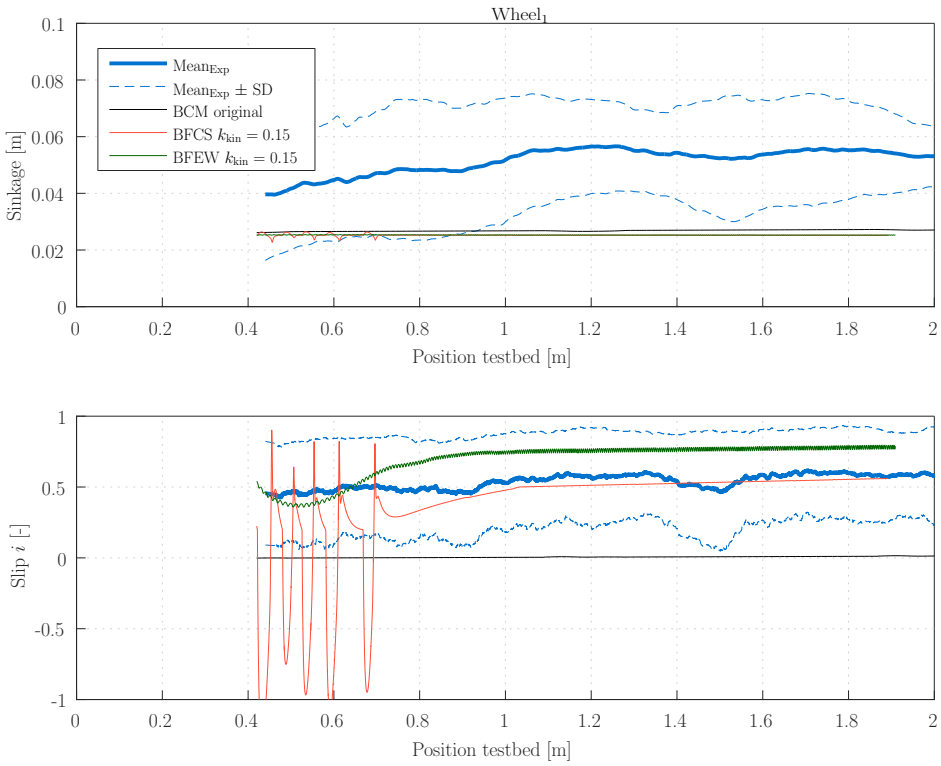

Figure 7.16.: *Free Slip Test*, Wheel$_1$, $v_{Des} = 0.05^{m}/_{s}$, sinkage, slip i.

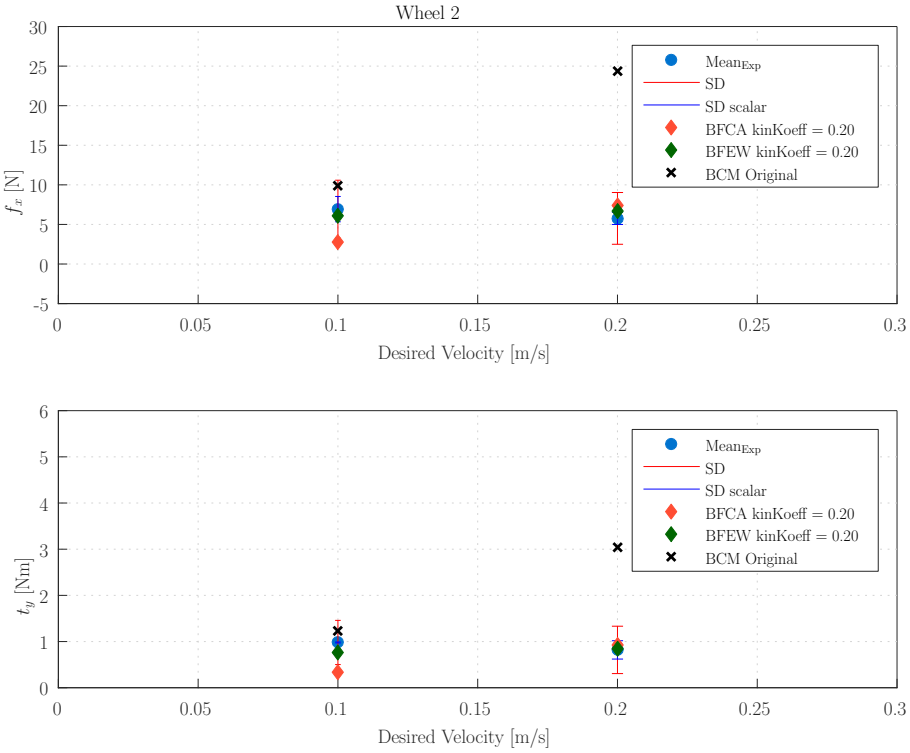

Figure 7.17.: *Free Slip Test*, Wheel$_2$, tractive force f_x, torque t_y.

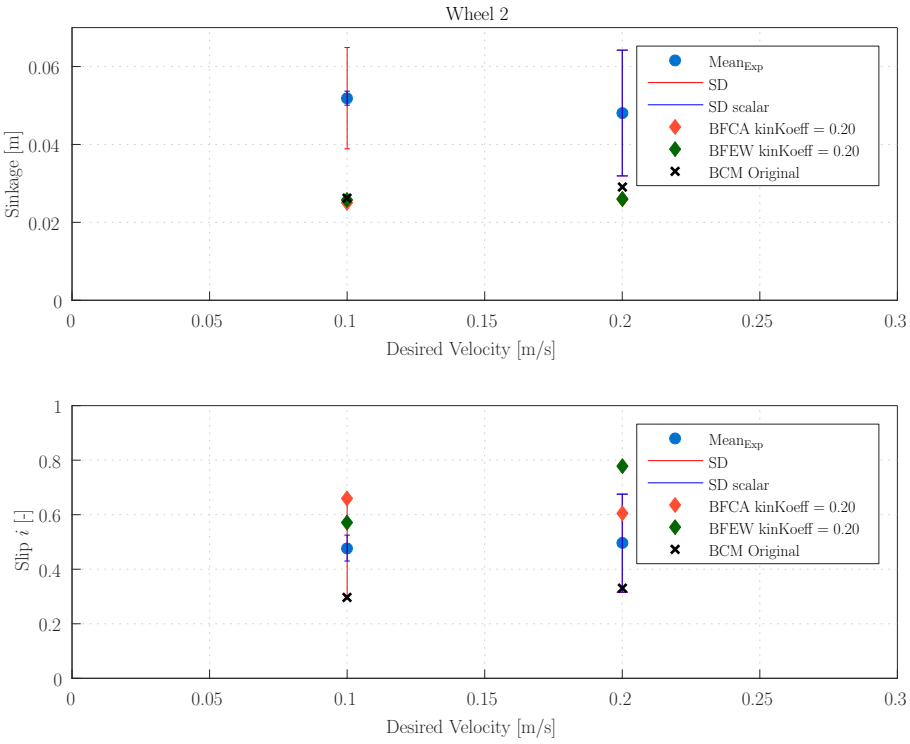

Figure 7.18.: *Free Slip Test*, Wheel$_2$, sinkage, slip i.

7.4. Computational Effort

In the following, the computational effort of the simulated test scenarios is considered from a real-time capability point of view. The original BCM is compared to the new implementations in Table 7.1. It is important to keep in mind that the simulation also includes visualization and contact detection, which also need considerable computational effort. As a result, it is not easily possible to determine the absolute effort of the model. For this reason, the multiplication of the computational effort related to the original BCM is considered.

The BFCS implementation has approximately a 1.5 times higher effort than the original BCM and for the BFEW implementation an effort 4 times higher is needed. However, it should be mentioned that for the BFEW more than a sixfold number of bristles, respectively contact patches is used compared to BFCS and BCM.

Table 7.1.: Computational effort of simulated test scenarios.

Test scenario	*Wheel Slip Test*	*Wheel Pull Test*	*Free Slip Test*
Simulation time	25 s	30 s	60 s
Computational effort (mean) in [s]			
BCM original (10×3) Contact patches	29	44	65
BFCS extension (10×3) Bristles	34	79	107
BFEW extension (40×3) Bristles	120	130	296

7.5. Evaluation

Both bristle friction extensions show, that they can limit absorption of contact reaction forces and torques of the soil and that this limitation depends on k_{kin}. In case of good parameter estimation of k_{kin}, this leads to an adequate consistency with the tractive performance of the wheel in experiments. Due to this limitation, the slip is also predicted distinctly higher than in the original BCM approach. The wheel sinkage is in all models significantly too low, because semi-empirical approaches based on the equations of

Bekker and Wong [45] do not consider dynamic sinkage.

However, the oscillation of the BFCS, caused by the changing bristle position within the contact surface, is still a problem and it impairs all simulation results. Due to this alternating bristle position, the tangential slip velocity from a different position of the wheel-soil contact surface is used to calculate bristle deflection. As a consequence, this bristle fixation is not suitable, because the oscillation can not be avoided and it impairs the results too strongly, as can be seen especially well in Figure 7.15 and Figure 7.16.

BFEW achieves better results than BFCS, as Figure 7.15 and Figure 7.16 show. In this approach there is only a slight oscillation, induced by the bristles which enter and leave the contact surface. The effect can be kept low by a sufficiently large number of bristles. For this reason, a fixation of the bristles on the wheel surface is significantly more reasonable. Through the fixed bristle position on the wheel surface, the tangential slip velocity is always used from the same position of the wheel surface and for computation of the bristle deflection.

The computation of the bristle deflection always needs information of previous time steps and it results in an increase of computational effort, which can hardly be avoided. In case of the BFCS, the additional effort is reasonable, whereas in case of BFEW, the computational effort is up to 4 times higher than the original BCM, because a significantly higher number of bristles needs to be used for this model, as mentioned in 5.2.

The problem of the model parameter k_{kin} is that it depends on the wheel (e.g. size of the grousers), as well as soil properties and thus, a parameter identification needs always to be done for each different wheel-soil pair.

In conclusion, the bristle fixation of the BFCS is unsuitable, because the occurring oscillation significantly impairs the simulation results. On the contrary, BFEW achieves adequate results and for a good k_{kin} parameter estimation the shear stress prediction achieves better results than the original BCM. The disadvantage of this extension is the considerably higher computational effort compared to the original BCM.

8. Conclusion and Outlook

8.1. Conclusion

The bristle friction model was introduced as an alternative approach of shear stress prediction in the existing wheel-soil contact model BCM and subsequently analyzed in *Dymola*. Within this work, a field campaign was performed in order to investigate the validity of the bristle friction extensions. Finally, the experiment results were discussed, investigated and compared to the simulation results.

In Chapter 4, the integration of the extended bristle friction model into the existing BCM was introduced. In this context, two approaches with different bristle fixation and distribution were elaborated, the BFCS with the bristles fixed on the contact surface and the BFEW with the bristles fixed on the entire wheel surface.
Both model extensions were analyzed in the modeling and simulation tool *Dymola*. The influence of the bristle stiffness and bristle damping coefficient were investigated, as well as different numbers of bristles in order to find suitable parameter values and numbers of bristles. Moreover, the damping methods of the original BCM and the bristle damping were compared.
In order to investigate the validity of BFEW and BFCS, a field campaign was performed on the Single-Wheel Testbed. Within this work, a new soil compression method was introduced, in order to improve the homogeneity of the soil density. After that, three different test scenarios were introduced for parameter estimation of k_{kin} and for model validation.
The results of Chapter 5 and Chapter 7 show that the bristle friction can be integrated into the existing BCM. However, the tests scenarios, which were chosen for the parameter

identification of k_{kin} prove to be suitable only to a limited extent. The main problem is that the dynamic sinkage and the bulldozing resistance, which are not considered in the models, have influenced the measurement results too strongly. As a result, the behavior of the tangential stress could not be considered separately and only parameter estimation was possible.

Due to the fact that k_{kin} is different for each wheel-soil pair, the obtained simulation results are only valid for the current soil and wheels. Further tests with different wheel-soil pairs are needed, in order to investigate a more general validity. However, due to the limited time frame more tests scenarios would go beyond the scope of this thesis.

8.2. Outlook

Finally, several suggestions for further developments are given, which can also be used as starting point for future works. Due to the idea that the bristle deflection shall depict the shear displacement also for compressed soil, the bristle deflection should behave like the dashed line in Figure 8.1 in order to achieve an approximation of the red line. However, the switching condition of the bristle model is only velocity-dependent. Thus, if the angular velocity of the wheel will be slowly increased, the bristle deflection can act as the dashed line. If the angular velocity is set to a high value immediately (e.g. a step function) the peak is skipped and the bristles behave similarly to the blue line. For this reason, an improvement to the bristle friction extension would be the implementation of an additional switching condition, which prevents the bristle from switching too early. A possible approach could be that the transition from static and to the kinetic regime only happens if v_{d} is exceeded and simultaneously the bristle deflection exceeds a certain value. As a result, the transition is not only velocity-dependent, but also depend on the deflection. Through such a modification the behavior, as the dashed line in Figure 8.1 indicates, would also be reached in case of high accelerations of the wheel. However, also suitable switching rules for the transition back to the static regime need to be found, to ensure that the static regime is not missed in simulation.

Due to the high computational effort of BFEW, a future work could also be a code analysis and optimization in order to increase the real-time capability of the model. A starting

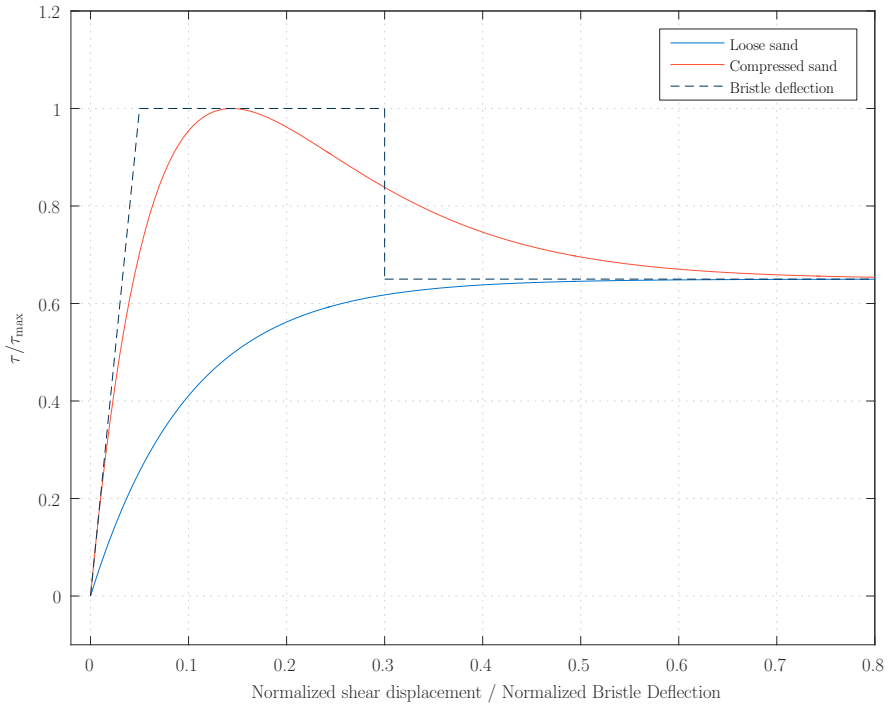

Figure 8.1.: Shear displacement of compressed and loose soil and bristle deflection.

point could be to find ways to reduce the number of bristles without decreasing the accuracy of the model.

In order to improve the parameter identification for the bristle friction extension, additional tests could be performed in future works. The influence of the effects, which are not included in the model, should be kept low. The *Wheel Pull Test* scenarios were performed with a blocked wheel. The test could be repeated with an unblocked wheel in order to keep the bulldozing resistance lower. A second possibility is to perform the *Wheel Slip Tests* on defined constant fixed sinkages. For this reason, the wheel suspension kinematic must be fixed or limited by a rope in vertical direction. Such a test configuration should make it possible to investigate, the shear stress at defined wheel sinkage and the problem of normal force measurement as it appeared in 7.1 should not occur. Another test would be to perform start up tests with different accelerations or different final velocities, in order to observe shear failure behavior of soil by a slow increasing angular velocity of the wheel.

As already mentioned, k_{kin} depends on the wheel-soil pair and therefore further tests for other wheels and soils are recommended. Through additional tests with other wheels it

might be possible to extract a reference point for the influence on k_{kin} by the grouser size. This could reduce the need of testing many wheels with different grousers in the same soil for future works. Instead of this, the tests on the same soil could be performed with one or two wheel types and for the other types k_{kin} could be estimated.

Constructive modifications on the SWT could improve the experiment results. The counterweight still induces oscillation, especially in the beginning of the experiment, when the velocity of the wheel suspension abruptly changes and further constructive modifications should reduce the influence of the counterweight. Another problem of the SWT is a sagging of the drawbar pull rope. Especially for tests, in which the rope needs to be redirected by a guide roller in order to pull the wheel in forward longitudinal moving direction. In this case, the rope sags and acts like a spring and results in an inhomogeneous pull of the wheel suspension. In order to reduce that problem, a linear motor could be used to pull the sled of the SWT.

Further development of a testbed is introduced in Buses work [3], which considers a robotic Single-Wheel Testbed (SWT). Instead of a rail and wheel suspension, a robot arm is used to guide the wheel. One advantage of this method is that the degrees of freedom can be increased. Thus, it is also possible to run tests with curves or with a tilted wheel.

A further advantage would be the realization of test automation, which makes it possible to perform entire series of experiments automatically. This procedure could help to identify k_{kin} rapidly for different types of wheels and different types of soil. Moreover, an automation of the soil preparation will be also developed. The robot arm could help to improve the accuracy of soil compression significantly, in order to achieve better reproducibility [3].

Appendices

A. Soil Preparation Method

In order to achieve best possible homogeneous soil conditions for experiments in the Single-Wheel Testbed (SWT) it is recommended to observe the following soil preparation instructions. Note that this soil preparation method was used for all experiments which are done within this thesis.

A.1. Soil Loosening Instruction

- The air ventilation must be turned on, during the entire preparation process in order to minimize dust formation.
- If the soil surface is rather uneven, even the surface with a large rake (Figure A.2).
- The soil must be loosened with the small rake (Figure A.1). Ensure that the rake reaches the bottom of the soil bin in order to loose all layers of the sand.
- Even the soil surface with large rake again (Figure A.2).

A.2. Soil Compression Instruction

- Place the soil preparation tool (SPT) on the even raked soil aligned parallel with the soil bin side walls.
- Ensure that the two people which are compress the soil have nearly the same weight.
- Person 1 (P_1) steps on the middle of the SPT. Position 1_{P_1} in Figure A.3.

Figure A.1.: Small rake

Figure A.2.: Large rake

- Person 2 (P_2) steps on the begin of the SPT. Position 1_{P_2} in Figure A.3.
- P_1 goes from Position 1_{P_1} to Position 2_{P_1} on the outer timbers step by step. Each individual foot step is marked on the SPT. The person puts its foot center on the mark. On each step the person shifts its weight on one side by doing three swaying movements.
- P_2 does the same from Position 1_{P_2} to Position 2_{P_2} by following the rhythm and velocity of P_1 .
- When P_1 and P_2 reached Position 2_{P_1}, respectively 2_{P_2}, both turn around an go back in the same manner from Position 2_{P_1} / 2_{P_2} to 3_{P_1} / 3_{P_2} to the initial position.
- However, now P_2 sets the rhythm and velocity of the movements and P_1 follows.
- Both stop when they reached their initial position 3_{P_1} respectively 3_{P_1}.
- Both persons leave the SPT simultaneously.
- One person steps on the SPT again at Position 4.
- The person goes foot by foot from Position 4 to Position 5, but now not on the outer timbers, but in the center of the SPT.
- The person leaves the SPT and the SPT is removed. The lane is now compressed.
- Repeat the procedure for the next lane. Note that, at least a distance of three finger breadth should be kept between two lanes.

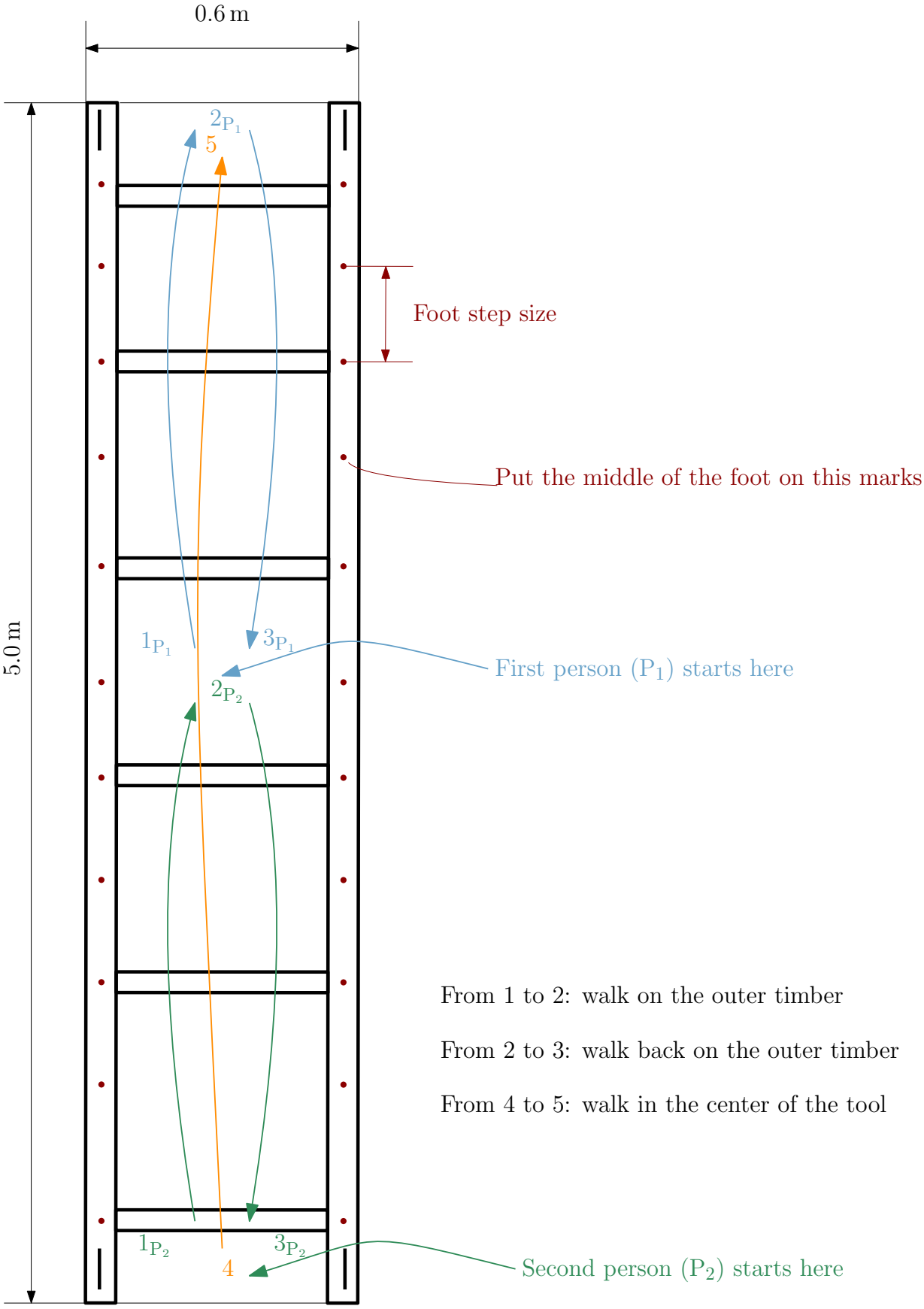

Figure A.3.: Compressing instruction on the soil preparation tool (top view)

B. Soil Density Results

In this section the results of the soil density measurement are listed. For the density measurements the soil penetration tool was used as it can be seen in Figure B.1 on the left. In order to determine the soil density, this tool was penetrated three times at each point A,B and C in the soil bin. The location of that points are shown on the right of Figure B.1. The soil penetration tool is in each measurement loaded by the same cuboid volume of soil with the width and depth of $d = 0.05\,\mathrm{m}$ and the height of $h = 0.12\,\mathrm{m}$ which leads to a volume of $V = 0.0003\,\mathrm{m}^3$. Finally, the mass of the amount of soil was measured, the soil density calculated and listed in Table B.1.

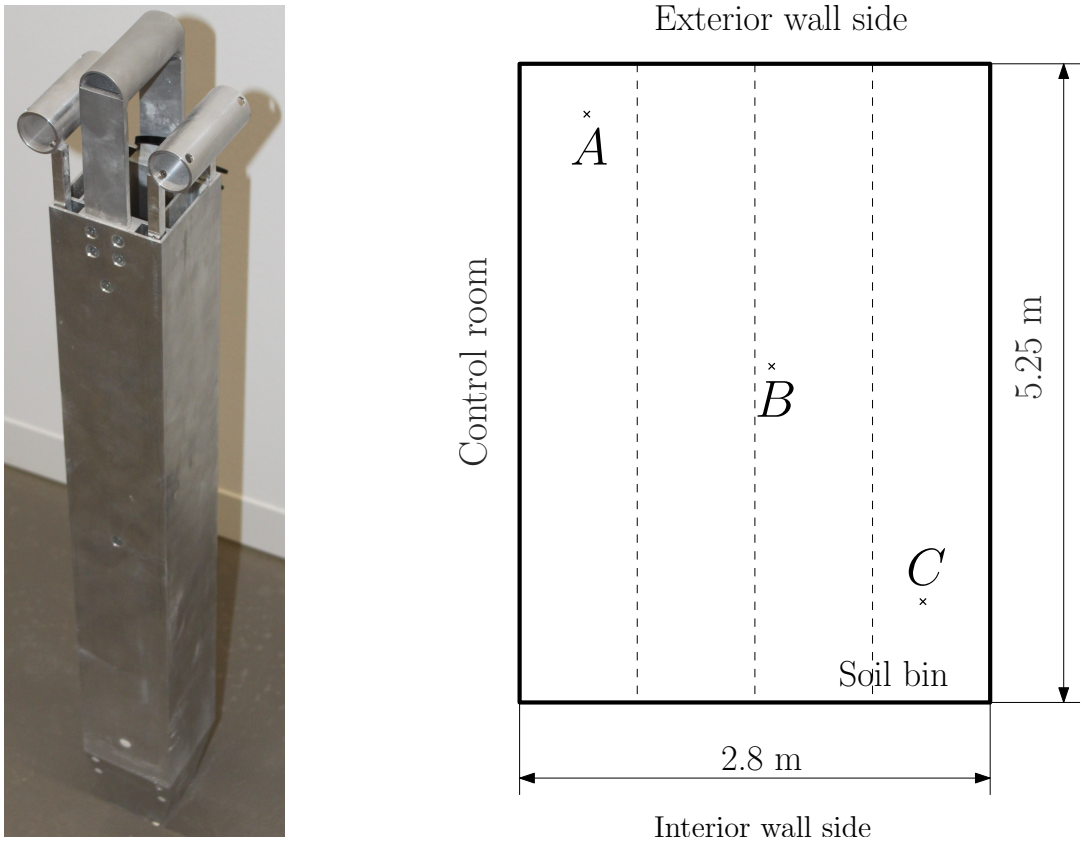

Figure B.1.: Left: soil penetration tool for soil density measurements.
Right: location of density measurements in the soil bin of the SWT

Table B.1.: Soil density results

Measurement	Soil mass in kg	Soil density in $^{kg}/_{m^3}$	Soil density in $^{kg}/_{m^3}$
A_1	0.35	1167	
A_2	0.37	1233	1178 ± 50.8
A_3	0.34	1133	
B_1	0.30	1000	
B_2	0.35	1167	1122 ± 107.2
B_3	0.36	1200	
C_1	0.20	667	
C_2	0.29	967	933 ± 251.7
C_3	0.35	1167	

Total soil density mean and standard deviation:

$\rho_{\mathrm{RMCS-13,comp}} = 1078\,^{kg}/_{m^3} \pm 177.8$

C. Resistance of the SWT Rail

In Figure C.1 the measured resistance force against the position of the wheel is plotted for different velocities in positive direction, i.e. from start position $\approx 0\,\mathrm{m}$ to end position $\approx 3\,\mathrm{m}$ (exterior wall side) of the soil bin.

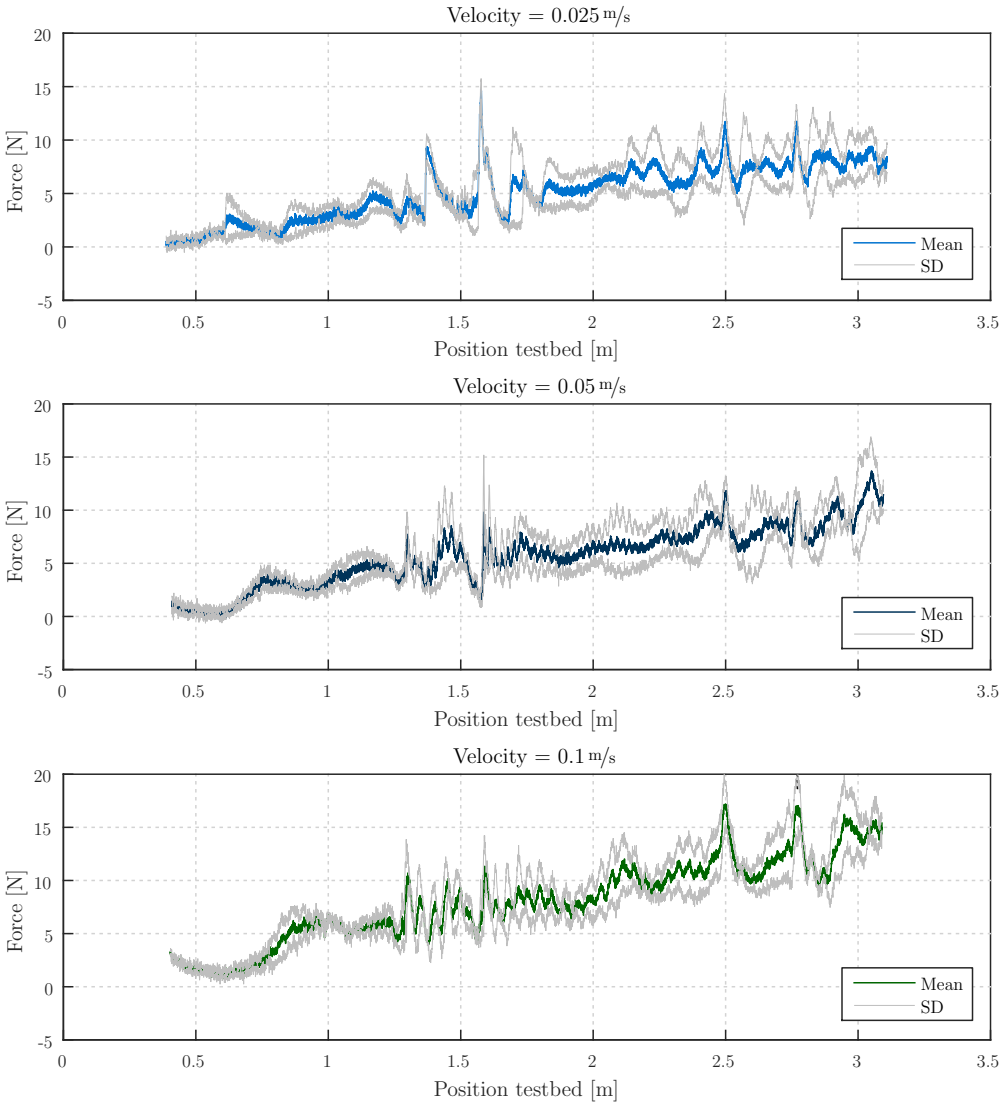

Figure C.1.: Resistance force of the SWT rail against to the position with different velocities (Unfiltered). From start position $\approx 0\,\mathrm{m}$ to end position $\approx 3\,\mathrm{m}$ (exterior wall side).

Moreover, a moving average plot[1] is given again in Figure C.2 for a better overview and comparison of the resistance force courses.

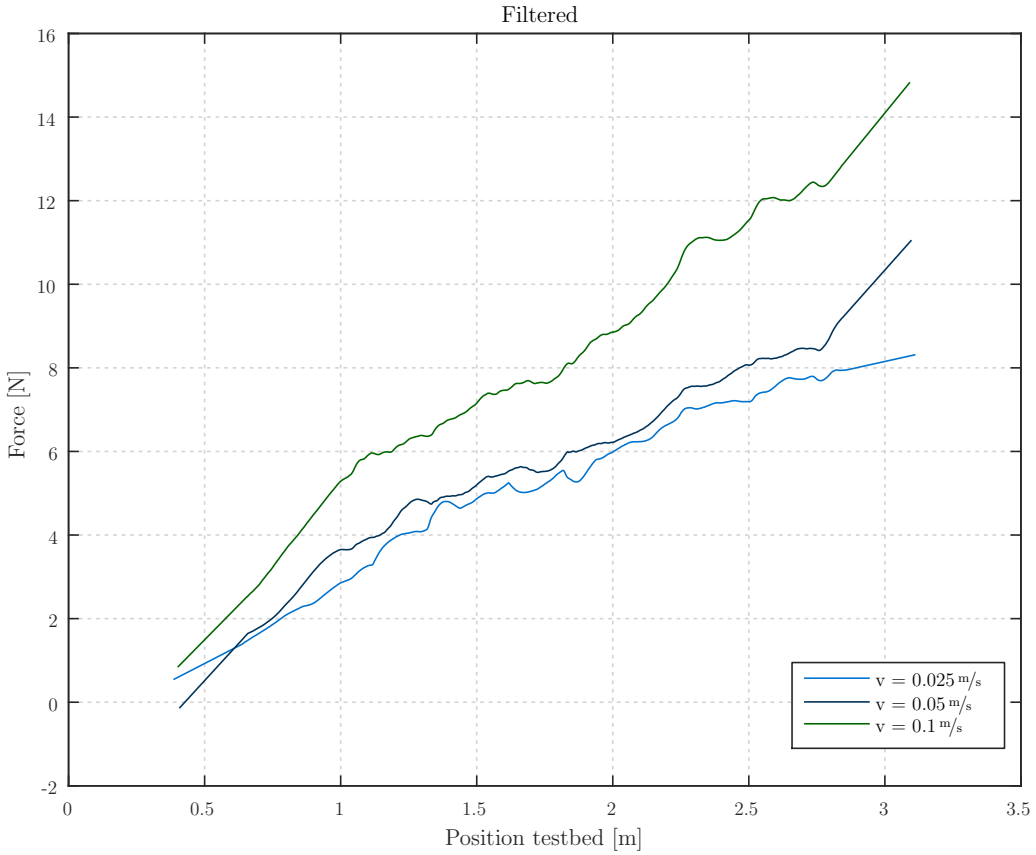

Figure C.2.: Resistance force of the SWT rail against to the position with different velocities (Filtered). From start position ($\approx 0\,\mathrm{m}$) to end position ($\approx 3\,\mathrm{m}$, exterior wall side).

[1]Plot smoothed by the Savitzky-Golay filter:
Degree: 1
Span: 5000
Size of each plot array ≈ 27500

In Figure C.3 the measured resistance force against the position of the wheel is plotted for different velocities in the opposite direction. This resistance is caused by the friction of the rail and the extraction of the drawwire sensor[2] and occurs if the SWT suspension is moved in negative direction, i.e. from end position $\approx 0\,\mathrm{m}$ (exterior wall side) to the start position ($\approx 3\,\mathrm{m}$) of the soil bin.

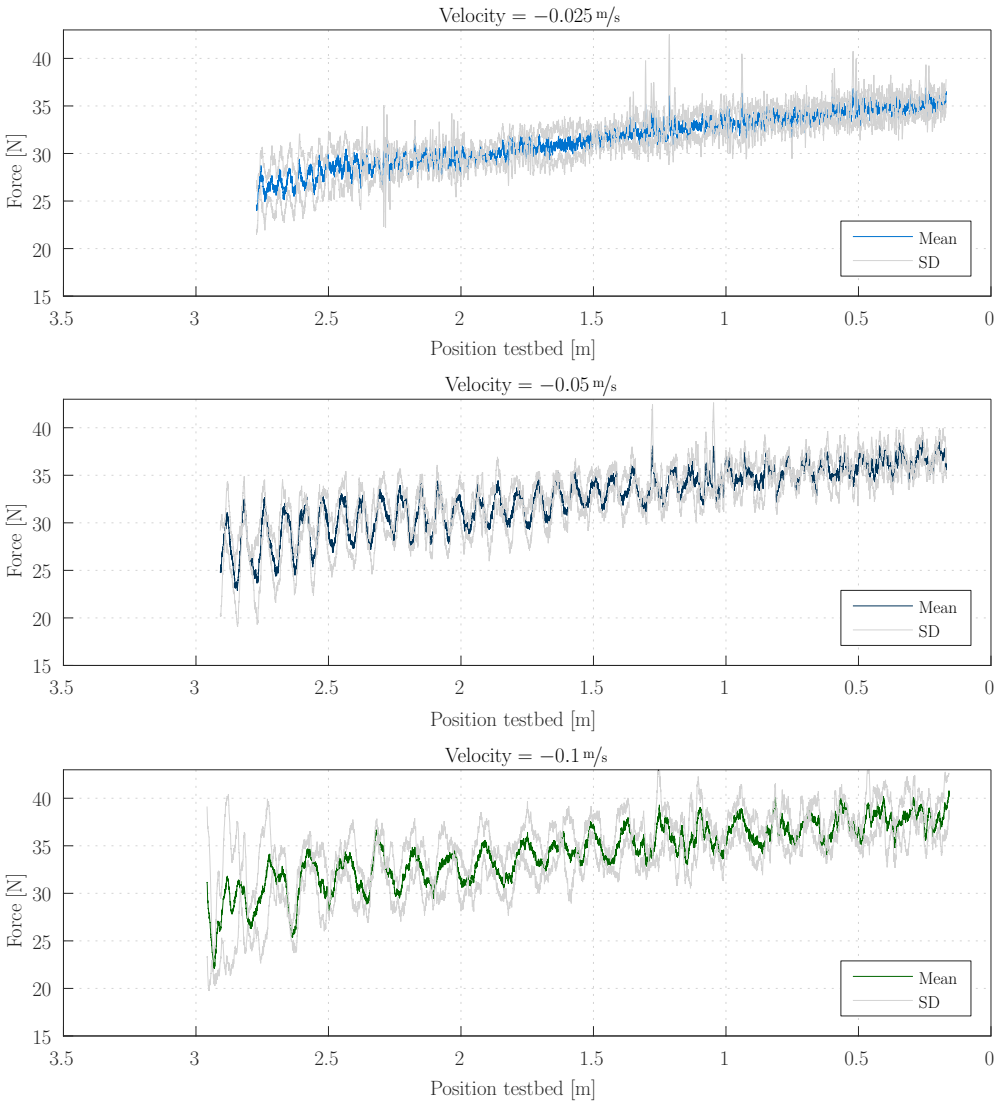

Figure C.3.: Resistance force of the SWT rail against to the position with different velocities (Unfiltered). From end position $\approx 3\,\mathrm{m}$ (exterior wall side) to start position $\approx 0\,\mathrm{m}$.

[2]Drawwire sensor - SX120 is used

The force which is needed to extract the drawwire sensor can range between 8.0 N and 11.6 N [44]. Finally, a moving average plot[3] can be seen in Figure C.4 for a better overview and comparison of the resistance force courses.

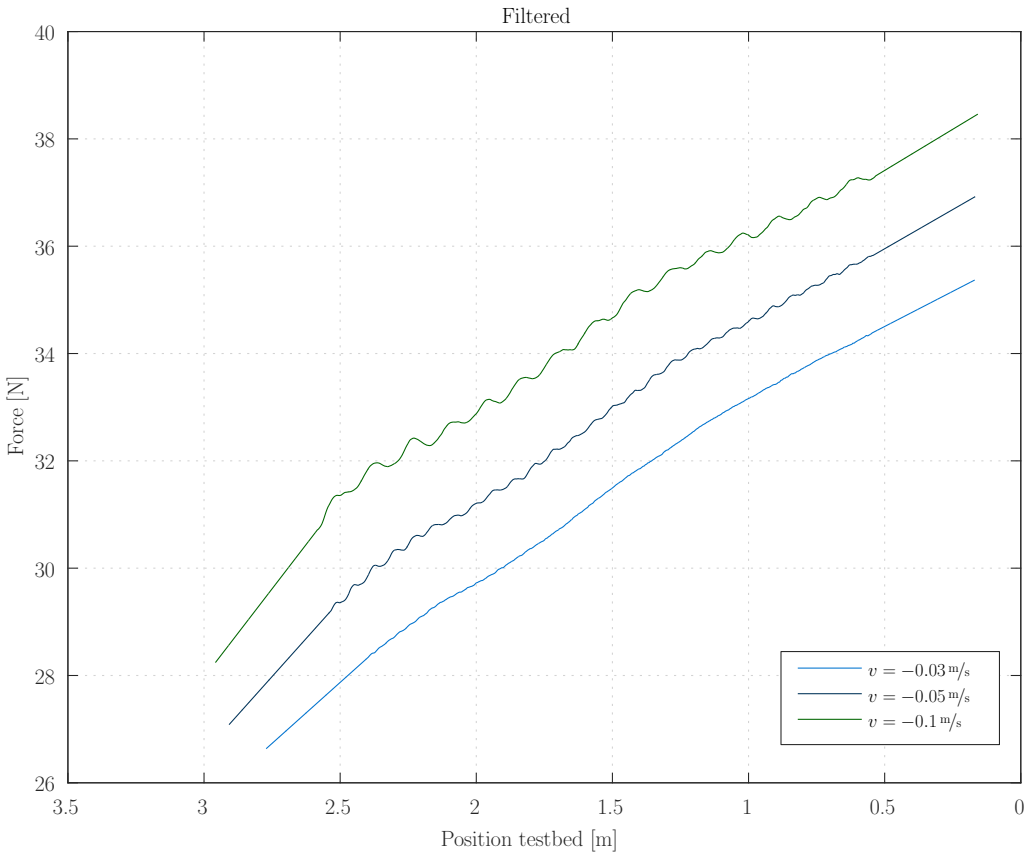

Figure C.4.: Resistance force of the SWT rail against to the position with different velocities (Filtered). From end position $\approx 3\,\mathrm{m}$ (exterior wall side) to start position $\approx 0\,\mathrm{m}$.

[3]Plot smoothed by the Savitzky-Golay filter:
Degree: 1
Span: 5000
Size of each plot array ≈ 27500

Bibliography

[1] Apfelbeck, Maximilian ; Kuss, Sebastian ; Rebele, Bernhard ; Schäfer, Bernd: A systematic approach to reliably characterize soils based on Bevameter testing. In: *Journal of Terramechanics* 48 (2011), S. 360–371. – ISSN 00224898

[2] Bekker, M G.: *Off-the-road locomotion: research and development in terramechanics*. University of Michigan Press, 1960

[3] Buse, Fabian: *Machbarkeitsstudie für einen roboterbasierten Radprüfstand zur Entwicklung von Mars Mondrovern*, RWTH Aachen, Master's Thesis, 2015. – 87 S.

[4] Dahl, P R.: A Solid Friction Model. In: *The Aerospace Corporation. Technical report* 158 (1968)

[5] Ding, Liang ; Deng, Zongquan ; Gao, Haibo ; Nagatani, Keiji ; Yoshida, Kazuya: Planetary rovers' wheel-soil interaction mechanics: new challenges and applications for wheeled mobile robots. In: *Intelligent Service Robotics* 4 (2011), Nr. 1, 17–38. http://dx.doi.org/10.1007/s11370-010-0080-5. – DOI 10.1007/s11370–010–0080–5. – ISSN 1861–2776

[6] DLR: *Explorationssysteme*. http://www.dlr.de/irs/desktopdefault.aspx/tabid-4505/. – (visted on 20.04.2016)

[7] DLR: *Herausragende Leistung beim SpaceBot Camp 2015*. http://www.dlr.de/rmc/rm/desktopdefault.aspx/tabid-3755/17612_read-44875/. – (visted on 25.02.2016)

[8] Dynasim AB: *Dymola User's Manual*. 2004

[9] Ellery, A.: *Planetary Rovers: Robotic Exploration of the Solar System*. Springer Berlin Heidelberg, 2015 (Springer Praxis Books). https://books.google.de/books?id=sLhPCwAAQBAJ. – ISBN 9783642032592

[10] ESA: *Mögliche Oasen für ExoMars*. http://m.esa.int/ger/ESA_in_your_country/Germany/Moegliche_Oasen_fuer_ExoMars. Version: May 2014. – (visted on 25.02.2016)

[11] Favaedi, Yalda ; Pechev, Alexandre ; Scharringhausen, Marco ; Richter, Lutz: Prediction of tractive response for flexible wheels with application to planetary rovers. In: *Journal of Terramechanics* 48 (2011), Nr. 3, 199–213. http://dx.doi.org/10.1016/j.jterra.2011.02.003. – DOI 10.1016/j.jterra.2011.02.003. – ISSN 00224898

[12] Fillmore, Steven ; Liang, Jianxun ; Ma, Ou: Experimental Validation of a 2D Bristle Friction Force Model. In: *ASME 2010 Dynamic Systems and Control Conference*. Cambridge, Massachusetts, USA : ASME, January 2010, S. 663–670

[13] Ghotbi, Bahareh ; Gonz, Francisco ; Angeles, Jorge: Effect of Multi-pass on the Mobility of Wheeled Robots on Soft Terrain. (2014), S. 6612–6617. ISBN 9781479936847

[14] Haessig D. A., Jr. ; Friedland, B: On the Modeling and Simulation of Friction. In: *Journal of Dynamic Systems, Measurement, and Control* 113 (1991), sep, Nr. 3, S. 354–362. http://dx.doi.org/10.1115/1.2896418. – DOI 10.1115/1.2896418. – ISSN 0022–0434

[15] Hellerer, Matthias ; Bellmann, Tobias ; Schlegel, Florian: The DLR Visualization Library - Recent development and applications. In: *Proceedings of the 10th International Modelica Conference* (2014), S. 899–911. http://dx.doi.org/10.3384/ECP14096899. – DOI 10.3384/ECP14096899

[16] Hinrichs, N. ; Obstreich, M. ; Popp, K.: On the modelling of friction oscillators. In: *Journal of Sound and Vibration* 216 (1998), Nr. 3, 435–459. http://dx.doi.org/10.1006/jsvi.1998.1736. – DOI 10.1006/jsvi.1998.1736. – ISSN 0022460X

[17] Iagnemma, Karl ; Senatore, Carmine ; Trease, Brian: Terramechanics Modeling of Mars Surface Exploration Rovers for Simulation and Parameter Estimation. In: *ASME Proceedings: 8th International Conference on Multibody Systems, Nonlinear Dynamics, and Control* (2011), 1–8. http://dx.doi.org/10.1115/DETC2011-48770. – DOI 10.1115/DETC2011–48770. ISBN 9780791854815

[18] Karnopp, D: Computer Simulation of Stick-Slip Friction in Mechanical Dynamical Systems. In: *Journal of Dynamic Systems, Measurement, and Control* Bd. 107, 1985, S. 420–436

[19] Krämer, Andreas ; Kempkes, Joachim: Modellierung und Simulation von nichtlinearen Reibungseffekten bei der Lageregelung von Servomotoren. In: *FHWS Science Jorunal* 1 (2013), Nr. 2, S. 47–57

[20] Krenn, R ; Gibbesch, A ; Hirzinger, G: Contact dynamics simulation of rover locomotion. In: *9th International Symposium on Artificial Intelligence, Robotics and Automation in Space* (2008). http://core.kmi.open.ac.uk/download/pdf/11084830.pdf

[21] Krenn, R ; Köppern, J ; Bünte, T ; Brembeck, J ; Gibbesch, A ; Bals, J: Model-based control approaches for overactuated planetary rovers and robotic, electrically powered vehicles [Modellbasierte Regelungsansätze für überaktuierte planetare Rover und robotische Elektromobile]. In: *at-Automatisierungstechnik* 61 (2013), Nr. 3, 183–194. http://dx.doi.org/10.1524/auto.2013.0022. – DOI 10.1524/auto.2013.0022. – ISSN 0178–2312

[22] Krenn, Rainer ; Hirzinger, Gerd: SCM - A Soil Contact Model for Multi-Body System Simulations. In: *11th European Regional Conference of the International Society for Terrain-Vehicle Systems - ISTVS 2009* (2009)

[23] Laughery, Sean ; Gerhart, Grant ; Goetz, Richard: Bekker's Terramechanics Model for Off-Road Vehicle Research. In: *US Army TARDEC. MI 48397-5000* (1990), 31. http://oai.dtic.mil/oai/oai?verb=getRecord&metadataPrefix=html&identifier=ADA457955

[24] Liang, Jianxun ; Fillmore, Steven ; Ma, Ou: An extended bristle friction force model with experimental validation. In: *Mechanism and Machine Theory* 56 (2012), October, 123–137. http://dx.doi.org/10.1016/j.mechmachtheory.2012.06.002. – DOI 10.1016/j.mechmachtheory.2012.06.002. – ISBN 0094–114X

[25] Lichtenheldt, Roy ; Schäfer, Bernd: Locomotion on soft granular soils: A discrete element based approach for simulations in planetary exploration. In: *12th Symposium on Advanced Space Technologies in Robotics and Automation: ASTRA 2013* http://elib.dlr.de/82475/

[26] Liu, J. ; Gao, H. ; Deng, Z.: Effect of Straight Grousers Parameters on Motion Performance of Small Rigid Wheel on Loose Sand. In: *Information Technology Journal* 7 (2008), S. 1125–1132. http://dx.doi.org/10.3923/itj.2008.1125.1132. – DOI 10.3923/itj.2008.1125.1132

[27] Lyasko, Modest: Slip sinkage effect in soil-vehicle mechanics. In: *Journal of Terramechanics* 47 (2010), Nr. 1, 21–31. http://dx.doi.org/10.1016/j.jterra.2009.08.005. – DOI 10.1016/j.jterra.2009.08.005. – ISSN 00224898

[28] Ma, Ou ; Liang, Jianxun ; Fillmore, Steven: A 2D Bristle Friction Force Model for Contact Dynamics Simulations. In: *ASME 2009 Dynamic Systems and Control Conference*. Hollywood, California : ASME, 2009, S. 501–508

[29] Marques, Filipe ; Flores, Paulo ; Lankarani, Hamid M.: On the Frictional Contacts in Multibody System Dynamics. In: *ECCOMAS Thematic Conference on Multibody Dynamics* (2015), 565–576. http://www.multibody2015.org/admin/files/fileabstract/a343.pdf

[30] Moreland, Scott: *Traction Processes of Wheels in Loose, Granular Soil*, Diss., 2013. http://repository.cmu.edu/cgi/viewcontent.cgi?article=1278&context=dissertations. – 154 S.

[31] NASA/JPL-Caltech: *In-situ Exploration and Sample Return: Autonomous Planetary Mobility*. http://mars.nasa.gov/mer/technology/is_autonomous_mobility.html. – (visited on 14.01.2016)

[32] NASA/JPL-Caltech: *Mars Exploration Rover - Spirit*. http://www.jpl.nasa.gov/missions/mars-exploration-rover-spirit-mer/. – (visted on 25.02.2016)

[33] NASA/JPL-Caltech: *Spirit and Opportunity - Mars Exploration Rovers - -Spirit Slipping in Soft Ground, Sol 1889*. http://www.nasa.gov/mission_pages/mer/images/pia12002.html. Version: May 2009. – (visited on 13. 01. 2016)

[34] NASA/JPL-Caltech: *NASA Mars Rover Curiosity Nears Mountain-Base Outcrop*. http://www.jpl.nasa.gov/news/news.php?release=2014-257. Version: August 2014. – (visted on 14.01.2016)

[35] Olsson, H. ; Åström, Kj K. ; Canudas de Wit, C. ; Gäfvert, M. ; Lischinsky, P.: Friction Models and Friction Compensation. In: *European Journal of Control* 4 (1998), Nr. 3, 176–195. http://dx.doi.org/10.1016/S0947-3580(98)70113-X. – DOI 10.1016/S0947–3580(98)70113–X. – ISBN 0947–3580

[36] Pruiksma, J.P. ; Kruse, G.A.M. ; Teunissen, J.A.M. ; Winnendael, M.F.P van: Tractive performance modelling of the ExoMars Rover wheel design on loosely packed soil using the Coupled Eulerian Lagrangian Finite Element Technique. In: *11th Symposium on advanced space technologies in robotics and automation* (2011), Nr. 1. http://robotics.estec.esa.int/ASTRA/Astra2011/Presentations/Session2A/02_pruiksma.pdf

[37] Scharringhausen, Marco ; Beermann, Dominik ; Krömer, Olaf ; Richter, Lutz: Single Wheel Tests for Planetary Applications at DLR Bremen. In: *11th European Regional Conference of the International Society for Terrain-Vehicle Systems* (2009), October

[38] Senatore, C. ; Sandu, C.: Off-road tire modeling and the multi-pass effect for vehicle dynamics simulation. In: *Journal of Terramechanics* 48 (2011), Nr. 4, 265–276. http://dx.doi.org/10.1016/j.jterra.2011.06.006. – DOI 10.1016/j.jterra.2011.06.006. – ISBN 00224898

[39] Stribeck, R.: Die wesentlichen Eigenschaften der Gleit- und Rollenlager. In: *Mitteilungen über Forschungsarbeiten auf dem Gebiete des Ingenieurwesens, ins-*

besondere aus den Laboratorien der technischen Hochschulen 7 (1903). https://books.google.de/books?id=nZssnQEACAAJ

[40] Tariku, Fitsum A. ; Rogers, Robert J.: Improved Dynamic Friction Models for Simulation of One-Dimensional and Two-Dimensional Stick-Slip Motion. In: *Journal of Tribology* 123 (2000), August, Nr. 4, 661–669. http://dx.doi.org/10.1115/1.1331057. – ISSN 0742–4787

[41] Terzaghi, Karl: *Erdbaumechanik auf Bodenphysikalischer Grundlage.* F. Deuticke, 1925

[42] The Modelica Association: Modelica A unified object-oriented language for physical systems modeling. In: *Simulation Practice and Theory* 5 (1997), Nr. 6. http://dx.doi.org/10.1016/S0928-4869(97)84257-7. – DOI 10.1016/S0928–4869(97)84257–7. – ISBN 978–3–540–64737–9

[43] Trease, Brian ; Arvidson, Raymond E. ; Lindemann, Randel ; Bennett, Keith ; Zhou, Feng ; Iagnemma, Karl ; Senatore, Carmine ; Dyke, Lauren V.: Dynamic Modeling and Soil Mechanics for Path Planning of the Mars Exploration Rovers. In: *Proceedings of the ASME 2011 International Design Engineering Technical Conference & Computers and Information in Engineering Conference IDETC/CIE* (2011), 1–11. http://web.mit.edu/mobility/publications/DETC2011-47896%20TREASE%20FINAL.pdf

[44] Waycon: *Drawwire sensor - SX120 / SX80 / SX50 Datasheet.* January 2014

[45] Wong, J.Y.: *Theory of Ground Vehicles.* John Wiley & Sons, 2008. – ISBN 9780470170380

[46] Yoshida, Kazuya ; Asai, Hisafumi ; Hamano, Hiroshi: Motion Dynamic Simulations and Experiments of an Exploration Rover on Natural Terrain. In: *6th International Symposium on Artificial Intelligence and Robotics & Automation in Space: i-SAIRAS 2001* (2001). http://robotics.estec.esa.int/i-SAIRAS/isairas2001/papers/Paper_AS026.pdf